



PONTIFICIA  
**UNIVERSIDAD  
CATÓLICA**  
DEL PERÚ

*th*  
TECHNISCHE UNIVERSITÄT  
**ILMENAU**

# Pontificia Universidad Católica del Perú

Escuela de Posgrado

## Tesis de Maestría

Optical system to observe and measure the spectra of a  
light emitting substrate and plasma in a RF magnetron

Para obtener el grado de:

**Master of Science (M. Sc.)**

en Ingeniería Mecatrónica

Presentado por: Julian Andreas Lich

Fecha y Lugar de Nacimiento: 09/05/1992 Gieben, Germany

Tutor Responsable (TU Ilmenau): Prof. Dr.-Ing. René Theska

Professor Responsable (TU Ilmenau): Prof. Dr.-Ing. René Theska

Professor Responsable (PUCP): Prof. Dr. Roland Weingärtner

Fecha y Lugar: 10/07/2017, Lima



## Scope of Master's-Thesis

Julian Andreas Lich

**Topic:** „Optical system to observe and measure the spectra of a light emitting substrate and plasma in a RF magnetron“

**Description:**

In the materials science sector of the PUCP, thin films are produced in a radio frequency magnetron sputtering chamber. During the fabrication of a-SiC:H:Tb films, Terbium emits light due to the excitation by the electrons within the plasma.

The objective of the thesis is to develop an external optical system, to capture light from the sputtering chamber into an available spectrograph. The target is to allow in-situ spectroscopy of the deposition process to get information about emission intensities, spectral distributions in dependence to parameter changes. It shall be possible to observe the substrate and the plasma separately.

**Tasks:**

1. Specification of the objective
2. Compilation of the state of the art
3. Construction of a basic prototype system
4. Experimental verification of the function principle
5. Formulation of potential solutions
6. Discussion and evaluation of the potential solutions
7. Construction of a final optical system

**Date of issue:** 01.02.2017

**Supervisors:** Prof. Dr. Roland Weingärtner (PUCP)

Prof. Dr. Ing. René Theska (TU Ilmenau)

Lima, 10.04.2017

Place, date

Signature Prof. Dr. Roland Weingärtner

Ilmenau, 17.05.2017

Place, date

Signature Prof. Dr. Ing. René Theska

Lima, 10.04.2017

Place, date

Signature Julian Andreas Lich

# Declaration of Authorship

I hereby certify that this thesis has been composed by me and is based on my own work, unless stated otherwise. No other person's work or thought has been used without acknowledgement in this thesis. All references and verbatim extracts have been quoted and all sources of information, including graphs, figures and data sets, have been specifically acknowledged.

Place, date:

Lima, 13.06.17

Signature:

*JL*



# Abstract / Kurzfassung

## Abstract

To obtain spectra of a light emitting substrate during the deposition of Terbium (Tb) doped thin films by RF magnetron sputtering, an optomechanical device is developed, constructed and tested.

The device is required to enable spatial scans of the substrate plane and the plasma beneath. Thereby, measurements of spatial emission intensity distribution and a separation of the Tb spectrum from the plasma-overlain substrate spectrum shall be possible.

After an introduction into theoretical and practical boundary conditions, the system's requirements are specified, followed by a brief investigation of existing solutions for similar problems.

A basic optical prototype system is introduced and analysed. After a discussion and evaluation of part solutions, an optomechanical system is developed, constructed, analysed and compared to the prototype system.

## Kurzfassung

Zur spektralen Analyse eines lichtemittierenden Substrates während des Beschichtungsprozesses von Terbium (Tb)-dotierten Dünnschichten durch RF Magnetron-sputtern wird ein optomechanisches Gerät entwickelt, konstruiert und getestet. Das Gerät soll räumliche Scans der Substratoberfläche und dem, sich darunter befindenden, Plasma ermöglichen. Räumliche Verteilungen der Emissionsintensität sollen dadurch messbar- und das Tb-Spektrum von dem plasmaüberlagerten Substratspektrum trennbar gemacht werden.

Nach einer Einführung in die theoretischen- und praktischen Rahmenbedingungen erfolgt die Präzisierung der Aufgabenstellung und eine kurze Recherche zu bereits vorhandenen Lösungen von ähnlichen Problemen.

Ein Prototyp wird vorgestellt und geprüft. Nach der Diskussion und Evaluierung von Teillösungen wird ein optomechanisches System entwickelt, konstruiert, analysiert und mit dem Prototyp verglichen.

# Contents

Scope of Master's Thesis	I
Declaration of Authorship	II
Abstract/Kurzfassung	III
Contents	IV
List of Figures	VII
List of Tables	IX
Abbreviations	X
Acknowledgements	XI
<b>1 Introduction</b>	<b>1</b>
1.1 Objective and Motivation	1
1.2 Plasma Generation and Direct Current (DC) Sputtering	2
1.3 Radio Frequency (RF) Sputtering	2
1.4 Magnetron Sputtering (MS)	3
1.5 Deposition of Terbium (Tb) doped Films	4
1.6 Optical Emission Spectroscopy (OES) with optical Spectrometers	4
1.7 Étendue and Lagrange Invariant	5
<b>2 System Requirements</b>	<b>9</b>
2.1 Utilised Facility	9
2.2 Utilised Spectrograph	11
2.2.1 Description	11
2.2.2 Defocus	12
2.3 Requirements	13

<b>3</b>	<b>State of the Art</b>	<b>19</b>
<b>4</b>	<b>Experimental Verification of a basic optical Assembly</b>	<b>24</b>
4.1	Assembly . . . . .	24
4.2	Description of experimental Procedure . . . . .	26
4.3	Discussion of Results . . . . .	29
<b>5</b>	<b>Discussion and Evaluation of potential Solutions</b>	<b>31</b>
5.1	Optics Placement . . . . .	32
5.1.1	Optics inside Chamber . . . . .	32
5.1.2	Optics completely outside Chamber . . . . .	34
5.1.3	Evaluation . . . . .	35
5.2	Spatial Homogenization . . . . .	35
5.2.1	Integrating Sphere . . . . .	35
5.2.2	Light Pipe . . . . .	36
5.2.3	Diffuser . . . . .	38
5.2.4	Evaluation . . . . .	39
5.3	Moving Field of View (FoV) . . . . .	39
5.3.1	Relative Movement between Fibre Entrance and Lens . . . . .	39
5.3.2	Moving entire Objective . . . . .	40
5.3.3	Evaluation . . . . .	41
5.3.4	Additional Possibility: Use of several FoV at once . . . . .	41
<b>6</b>	<b>Construction of an optomechanical System</b>	<b>42</b>
6.1	Optics . . . . .	42
6.1.1	Fibre . . . . .	42
6.1.2	Lens . . . . .	42
6.2	Mechanics . . . . .	44
6.2.1	Rotational-/translational Movements . . . . .	44
6.2.2	Mechanical Principle and Construction . . . . .	45
<b>7</b>	<b>Analysis of the System</b>	<b>49</b>
7.1	Setup . . . . .	49
7.2	Field of View (FoV) . . . . .	50
7.3	Resolution and Intensity at different axial Fibre Positions . . . . .	54
7.4	Tb- and Plasma Signal . . . . .	56
<b>8</b>	<b>Summary and Outlook</b>	<b>60</b>
8.1	Summary . . . . .	60
8.2	Outlook . . . . .	61

<b>A Appendix</b>	<b>63</b>
A.1 Supplements to Chapters . . . . .	63
A.1.1 To Section 6.1.1 . . . . .	63
A.1.2 To Section 6.1.2 . . . . .	63
A.1.3 To Section 6.2.2 . . . . .	66
A.1.4 To Section 7.2 . . . . .	68
A.1.5 To Section 7.4 . . . . .	69
A.2 Drawings . . . . .	69



# List of Figures

1.1	DC Sputtering . . . . .	2
1.2	RF Sputtering . . . . .	2
1.3	Magnetron Principle . . . . .	3
1.4	Cylindrical Magnetron and Sputter Gun . . . . .	3
1.5	Terbium Emission . . . . .	4
1.6	Prism Spectrometer . . . . .	5
1.7	Grating Spectrometer . . . . .	5
1.8	Solid Angle $\Omega$ and projected Area $A$ . . . . .	6
1.9	Solid Angle $\Omega$ . . . . .	7
1.10	Sketch of optical System . . . . .	8
2.1	Photograph of Chamber . . . . .	10
2.2	Geometrical System Requirements . . . . .	10
2.3	Defocussed Spectrograph . . . . .	12
2.4	Spectral Shift by changing Entering Ray Direction . . . . .	13
2.5	f-Number . . . . .	15
3.1	OES Fiber in Quartz Pipe . . . . .	20
3.2	Example Lens . . . . .	20
3.3	Example Laser Induced Breakdown Spectroscopy (LIBS) . . . . .	21
3.4	Long Slit Spectroscopy . . . . .	22
3.5	Capturing multiple Objects with Lenslet System . . . . .	22
4.1	First Assembly . . . . .	25
4.2	Observability of FoV and Stray Light Reduction . . . . .	25
4.3	Dark Signal Correction . . . . .	26
4.4	Extraction of Tb Spectrum . . . . .	28
4.5	Tb Spectrum AlN . . . . .	30
4.6	High Resolution Tb Measurement . . . . .	30
4.7	Spectral Shift of Plasma . . . . .	30
5.1	Function Structure . . . . .	31



5.2	Examples of Optics inside Chamber . . . . .	33
5.3	Motion Control from outside the Chamber . . . . .	34
5.4	Optics outside Chamber . . . . .	35
5.5	Light Pipe Cross Section . . . . .	37
5.6	Fibre Angle of Light Input . . . . .	37
6.1	Estimation of FoV . . . . .	44
6.2	Movement in y-Direction . . . . .	45
6.3	Technical Principle . . . . .	46
6.4	Examples of Optics inside Chamber . . . . .	48
7.1	Analysis Setup . . . . .	49
7.2	Aperture- and FoV Illumination . . . . .	51
7.3	Examples of Optics inside Chamber . . . . .	51
7.4	Moving FoV . . . . .	52
7.5	Scaled Substrate Holder . . . . .	53
7.6	Graphs for optimal axial Fibre Positions . . . . .	54
7.7	Refocus with Fibre . . . . .	55
7.8	Process Conditions while testing Final- and Prototype System	56
7.9	Extraction and Comparison of Tb Spectrum . . . . .	58
7.10	Comparison of Plasma Spectra . . . . .	59
A.1	Fibre Attenuation . . . . .	63
A.2	Parax System Dimensions . . . . .	64
A.3	Oslo System Dimensions . . . . .	65
A.4	Lens AR Coating . . . . .	66
A.5	Substrate Inclination Consequences . . . . .	67
A.6	Relationship $\Delta x/\Delta X$ . . . . .	67

# List of Tables

4.1	Details of Prototype System Test . . . . .	26
5.1	Evaluation Table: Placement of optical System . . . . .	35
5.2	Evaluation Table: Homogenization Method . . . . .	39
5.3	Evaluation Table: Movement of FoV . . . . .	41
6.1	Objective Requirements . . . . .	43
A.1	Results of Repeatability and Extend . . . . .	68
A.2	Measurement Conditions: Prototype/Final system . . . . .	69

# Abbreviations



<b>AR</b>	Anti Reflection
<b>CCD</b>	Charge-Coupled Device
<b>CL</b>	Cathodoluminescence
<b>CVD</b>	Chemical Vapor Deposition
<b>DC</b>	Direct Current
<b>DoF</b>	Degree(s) of Freedom
<b>DSC</b>	Dark Signal Corrected
<b>EP</b>	Entrance Pupil
<b>FoV</b>	Field of View
<b>FWHM</b>	Full Width Half Maximum
<b>LIBS</b>	Laser Induced Breakdown Spectroscopy
<b>RFMS</b>	Radio Frequency Magnetron Sputtering
<b>RIE</b>	Reactive Ion Etching
<b>OES</b>	Optical Emission Spectroscopy
<b>PUCP</b>	Pontificia Universidad Católica del Perú
<b>PVD</b>	Physical Vapor Deposition
<b>RF</b>	Radio Frequency
<b>Tb</b>	Terbium

# Acknowledgements

This work was written within the scope of the IISD double degree program of the TU Ilmenau and the Pontificia Universidad Católica del Perú (PUCP).

I want to thank Prof. Dr.-Ing. René Theska from the TU Ilmenau for his support before and during the program, especially while I was writing the master's thesis.

Furthermore, I want to thank Prof. Dr. Roland Weingärtner and the Solid State Physics & Materials Science Group of the PUCP, who enabled and assisted my work and who also gave me an interesting first insight into semiconductor technology. Moreover, I want to thank them, as well as my other friends, for making me truly enjoy my time in Perú.

Last of all, special thanks go to my family, who supported me uncompromisingly during my studies.

# Chapter 1

## Introduction

### 1.1 Objective and Motivation

During the deposition of Tb doped thin films by Radio Frequency Magnetron Sputtering (RFMS), the Tb emits light under certain process conditions.

The goal of this work is to develop an optomechanical system which channels light from the plasma and the Tb doped thin film to a spectrograph. Thereby, in-situ emission spectroscopies of the deposition process shall be possible. It shall also be possible to scan the substrate's surface systematically to measure spatial emission distributions on substrate and plasma.

Being able to measure and track spectral distributions and intensities over time and at different spots allows parameter studies during the deposition process itself.

In case of the Tb film, emission intensity plays a major role. It gives information about concentration and stimulation of Tb at the observed spots. With the emission spectrum, Tb can be proven as source of emission.

In case of the plasma, its whole spectrum is interesting because it gives information about the plasma's composition, which is also crucial for the process properties.

## 1.2 Plasma Generation and DC Sputtering

The basic setup for the DC sputtering process contains a vacuum chamber with two metallic electrodes and a supply for sputter gas. As seen in figure 1.2, the sputter gas gets ionized due to the electric field between cathode and anode: Free electrons get accelerated by the electric field and collide with gas atoms. Due to the collision, a free electron can "knock off" an electron from the gas atom. Now there are two free electrons which again are accelerated towards the anode until they collide with other gas atoms. This avalanche effect leads to an ionization of the sputter gas, transforming it into plasma and making it conductive. The positively charged gas ions get accelerated towards the target cathode. When they collide with it, they knock particles off the target, which is the actual intention of the sputter process.

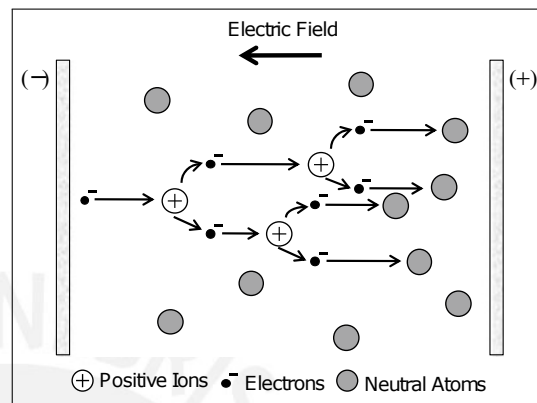


Figure 1.1: Principle of gas discharge. Credit: [Noj15]

## 1.3 Radio Frequency (RF) Sputtering

If the target material is an insulator, the surface gets charged up by the positive sputter gas ions. This weakens the electrical field between cathode and anode. Eventually, there will be no more current and no more discharges. DC sputtering is just possible with metallic targets. For other materials, impossibly high voltages would be necessary [Ohr01].

If the DC power supply is substituted by an RF source, discharges get possible for non metallic targets. RF sputtering gets possible because of a target self biasing [Beh81, Noj15]. Due to their minor mass, the electrons have a

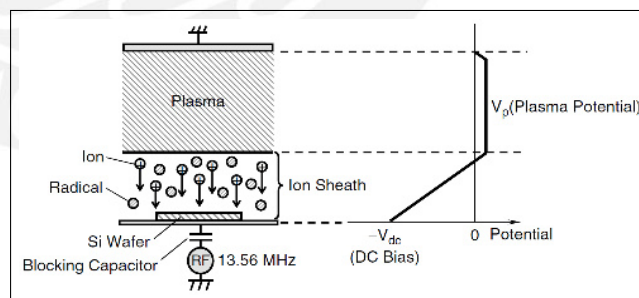


Figure 1.2: Example of RF Reactive Ion Etching (RIE). Credit: [Noj15]

higher mobility than the sputter gas ions. During the positive cycle, a great amount of electrons reach the lower electrode (figure 1.3). Much less positively charged ions reach the lower electrode during the negative cycle due to their higher inertia. By the implementation of a blocking capacitor, the electrons are hindered to leave the electrode so that it becomes biased to a negative potential  $-V_{dc}$  [Noj15]. Hence, discharges become possible also for isolating targets. [Beh81, Ohr01, Noj15, WKA04]

## 1.4 Magnetron Sputtering (MS)

To increase the electrons' chances of colliding with gas atoms, a magnetic field is introduced, as shown in figure 1.4. This causes the electrons not to move in a straight line between the electrodes but in an additional orbit around the magnetic field lines. The electrons' effective paths increase significantly, as well as the chances of colliding with other particles. More particles get ionized and accelerated towards the target, leading to a higher sputtering rate.

Another advantage is the possible reduction of process pressure. The chance of collision between particles decreases. Ions hit the target with higher average energies, knocking off a greater amount of target particles. Due to the reduction of particle collision, the "knocked off" particles fly a longer distance and get less frequently scattered to other directions. This leads to higher deposition rates [Ohr01].

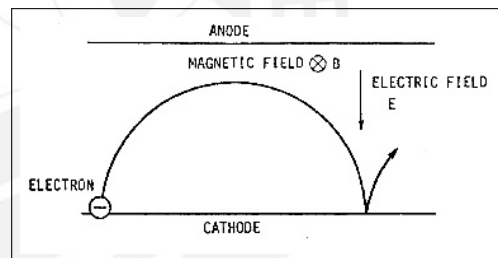


Figure 1.3: Path of electron between electrodes in the presence of a magnetic field. Credit: [WKA04]

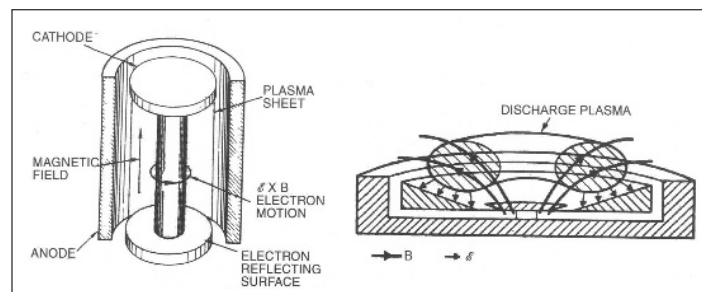


Figure 1.4: Cylindrical Magnetron (left) and Sputter Gun (right). Credit: [Ohr01]

## 1.5 Deposition of Terbium (Tb) doped Films

As mentioned in section 1.4, the sputtering process can be used to deposit the knocked off particles onto another surface. One or more sputter guns (figure 1.4, right picture) can be used to produce thin films, made of one or more materials.

The process relevant for this work is the deposition of Tb doped semiconductor materials like Si, SiC or AlN. One sputter gun with a matrix-target and one with a Tb-target "shoot" the particles onto a substrate to form a thin film. During this process, Tb inside the semiconductor matrix gets excited by the plasma and starts to luminesce characteristically (figure 1.5a).

Figure 1.5b shows peaks of Tb doped SiC:H between 475 nm and 650 nm [GDZT<sup>+</sup>16]. These peaks are characteristic for Tb<sup>3+</sup> Ions and also occur in Tb doped AlN [GMW<sup>+</sup>15, LJ07]. They are the main region of interest for this work.

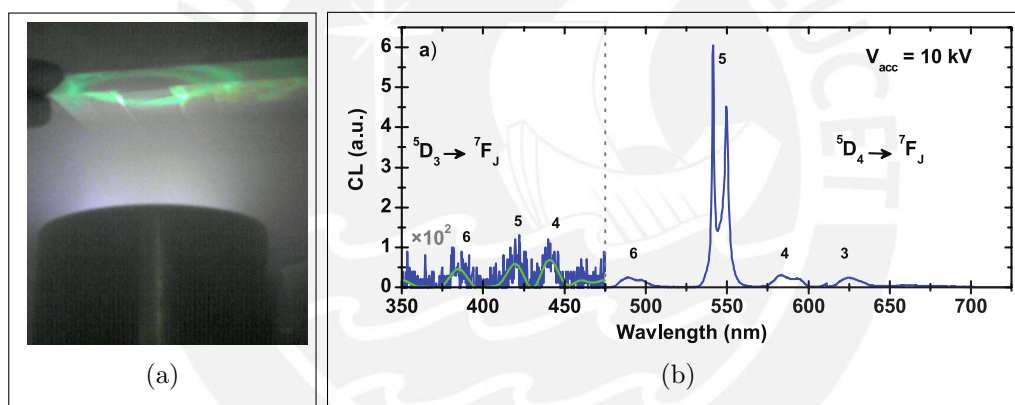


Figure 1.5: (a) Photograph of in-situ Tb emission, taken from sputtering chamber. (b) Cathodoluminescence (CL) spectrum of SiC:H doped with Tb and annealed at 1050°C. Credit: [GDZT<sup>+</sup>16]

## 1.6 Optical Emission Spectroscopy (OES) with optical Spectrometers

Optical spectrometers analyse the composition of light by monitoring its distribution of intensity over wavelength (spectrum). An example of an optical spectrometer's possible setup is shown in figure 1.6.



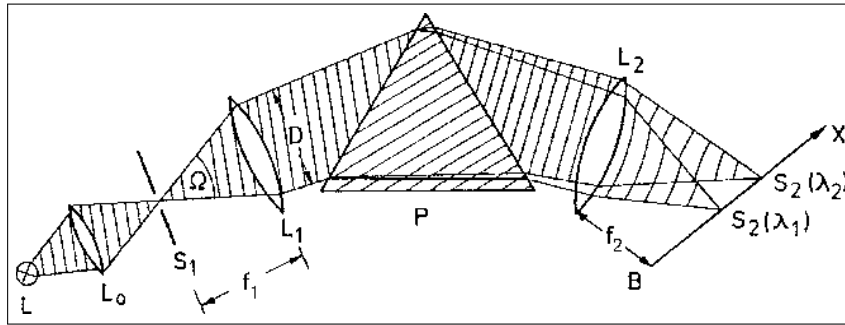


Figure 1.6: Setup of a prism spectrograph. Credit: [Dem14]

The light that enters the entrance slit  $S_1$  gets collimated by a lens  $L_1$  or a curved mirror. The collimated beam then gets directionally distributed into its particular wavelengths by a prism  $P$  or an optical grating. A second Lens  $L_2$  or another curved mirror focusses the beams onto an exit plane  $B$ . According to the light's wavelength, the entrance slit gets imaged ( $S_2(\lambda)$ ) onto different positions  $x$  on the exit plane.

Optical spectrometers can be distinguished into spectrographs and monochromators. A spectrograph analyses a larger spectral range at a time by having a CCD-sensor in the exit plane. A monochromator has a slit in the exit plane to isolate a small range of wavelengths from the spectrum. Next to other possible applications, the intensity of this isolated wavelength can be measured by a detector. To measure the whole spectrum, either the output slit has to be moved, or the grating's direction has to be changed for each wavelength [Dem14]. In this work, a grating spectrometer that can be spectrograph or monochromator, as shown in figure 1.6, is utilised.

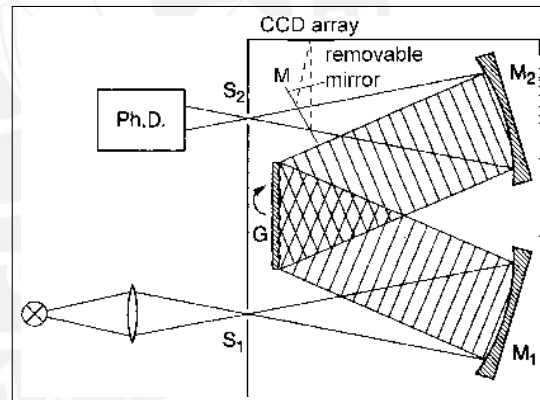


Figure 1.7: Setup of a grating spectrometer. Credit: [Dem14]

## 1.7 Étendue and Lagrange Invariant

To enable quick and accurate spectrography, enough light has to be captured from the measured object. *Étendue* is a geometrical quantity which gives information about how much light a lossless optical system can cap-

ture without knowing the measured object's emission properties. It is also known as *light-gathering power* [New], *throughput* [New, Kos12, Kas11] and *optical/geometrical extent* [New, Kos12].

The total flux  $\Phi$  in an optical system can be described as the source radiance  $L$  integrated over the projected source area  $\cos\theta dA$  (figure 1.8b) and the solid angle  $d\Omega$  in view of the Entrance Pupil (EP) [Kos12]:

$$\Phi = \iint_{\text{EP}} L(\mathbf{r}, \hat{\mathbf{a}}) \cos\theta dA d\Omega, \quad (1.1)$$

where  $L$  depends on position  $\mathbf{r}$  and direction  $\hat{\mathbf{a}}$ .

If  $L$  is constant over all  $\hat{\mathbf{a}}$  (*lambertian*) and  $\mathbf{r}$ , equation 1.1 becomes

$$\Phi = L \iint_{\text{EP}} \cos\theta dA d\Omega. \quad (1.2)$$

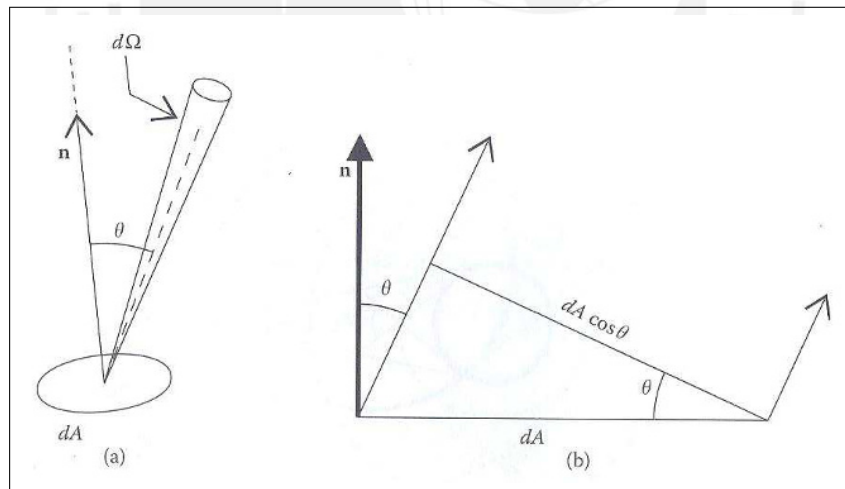


Figure 1.8: (a) Solid angle  $\Omega$  and (b) projected area  $A$ . Credit: [Cha08].

Étendue is defined as [Kos12]

$$E = n^2 \iint_{\text{EP}} \cos\theta dA d\Omega, \quad (1.3)$$

which means that the flux can be rewritten as

$$\Phi = \frac{L E}{n^2}. \quad (1.4)$$

The solid angle  $d\Omega$  is defined as [Kos12, Cha08]

$$d\Omega = \frac{dA^*}{r^2} = \sin\theta \, d\theta \, d\phi, \quad (1.5)$$

where  $dA^*$  is the surface on- and  $r$  the radius of a (hemi-)sphere, as can be seen in figure 1.9.

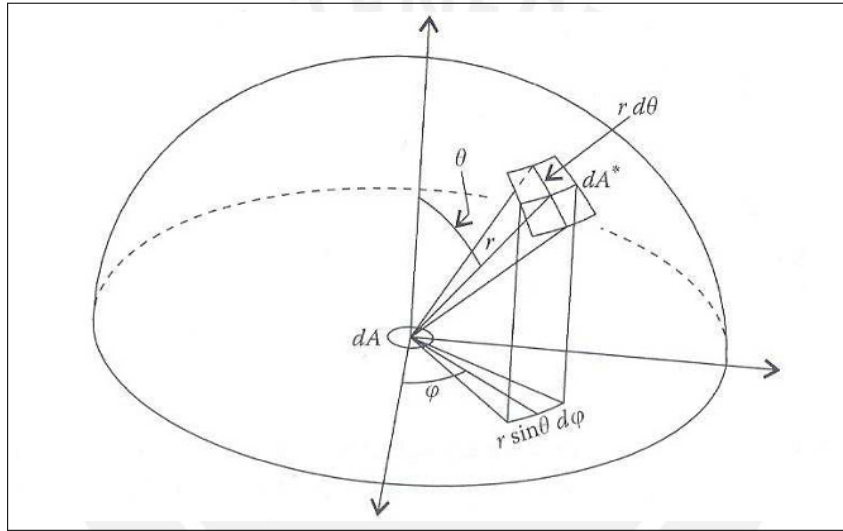


Figure 1.9: Solid angle  $\Omega$  in spherical coordinates. Credit: [Cha08].

In a rotationally symmetric system (as can be seen in figure 1.10) with a small source area  $A$ , the half cone angle  $\theta_a$  is nearly constant over  $\phi$ . In this case, *Étendue* can be defined as [Kos12]

$$E = n^2 A \int_0^{2\pi} \int_0^{\theta_a} \cos\theta \sin\theta \, d\theta \, d\phi = \pi n^2 A \sin^2\theta_a. \quad (1.6)$$

Applied to the paraxial regime, a conserved relationship between aperture angle  $\theta_a$ , chief ray height  $h$ , field angle  $w$  and marginal ray height  $y$  can be used. It is called the *Optical- or Lagrange Invariant H* [Kas11, Kos12]. It is generally defined as

$$H = n(h\theta_a - wy) = n'(h\theta'_a - w'y) \quad (1.7)$$

and can be rewritten as

$$H = nh\theta_a = n'h'\theta'_a \quad (1.8)$$

for object and image space (figure 1.10). It is the paraxial form of *Étendue* [Kos12], since

$$H^2 \propto E \quad (1.9)$$

for rotationally symmetric objects in the paraxial regime.

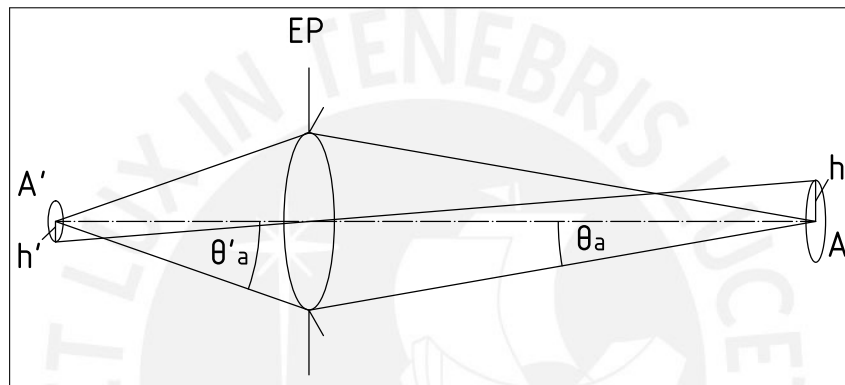


Figure 1.10: Sketch of rotationally symmetric optical system

$E$  and  $H$  are constant over the entire optical system. Field size and aperture are inversely proportional to each other:

$$h = \frac{H}{n\theta_a}. \quad (1.10)$$

For a spectrograph, this invariance means that *étendue* is defined by its slit width and *f-number*, i.e.  $2h'$  and  $2\theta'_a$  in figure 1.10. If the object space aperture is increased, the object field will get smaller. If the object space aperture is decreased, the field becomes larger. Assuming that the light source is a spatially and directionally (lambertian) homogeneously emitting area, flux channelled into the spectrograph does not change in any of these cases.

*Étendue* gives information about the theoretical amount of flux which can be channelled through an optical system. In reality there will be flux losses due to absorption, scattering or Fresnel reflection. Gains due to additional light sources can also be present. These effects are not considered by *Étendue* but need to be avoided or optimized to achieve the necessary throughput conditions.

# Chapter 2

## System Requirements

### 2.1 Utilised Facility

The used facility is a self constructed RFMS chamber in a laboratory of materials science in the physics department of the Pontificia Universidad Católica del Perú (PUCP). The chamber walls are made of non-magnetic, stainless steel. Exchangeable aluminium foil protects the walls from contamination. The front door and the left wall (figure 2.1) contain a central window each. An exchangeable protecting glass (figure 2.2) is placed between each window and the plasma region to protect the windows from contamination by the deposition process.

Each of the three magnetrons is connected to an RF generator through a bendable tube, which permits adjusting their tilt.

The substrate holder is water cooled. It can be rotated around- and moved along the z-axis in figure 2.2. There is also an adjustable shutter which can be used to stop deposition on the substrate.

A turbo molecular pump is able to produce a pressure of down to  $2.5 \cdot 10^{-6}$  mbar. During the sputtering process, a pressure of about  $(0.9...1.5) \cdot 10^{-2}$  mbar is set inside the chamber. Concentrations of Argon, Nitrogen, Oxygen and Hydrogen can be set by four mass flow controllers. A mass spectrometer is connected to the chamber and there are three KF40- and seven 1-1/3 CF flanges left for additional applications.

The chamber is mainly used to fabricate wide bandgap, amorphous semiconductor films such as SiC or AlN doped with rare earths such as Tb or Yb.

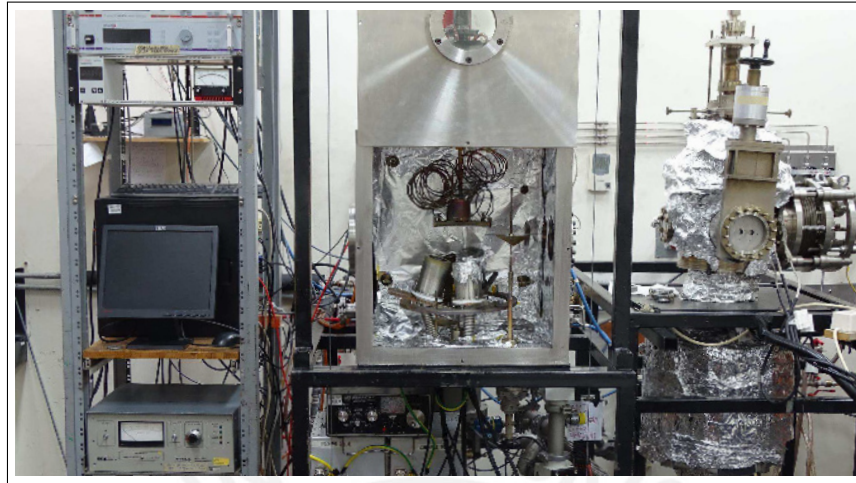


Figure 2.1: Photograph of chamber and surroundings.

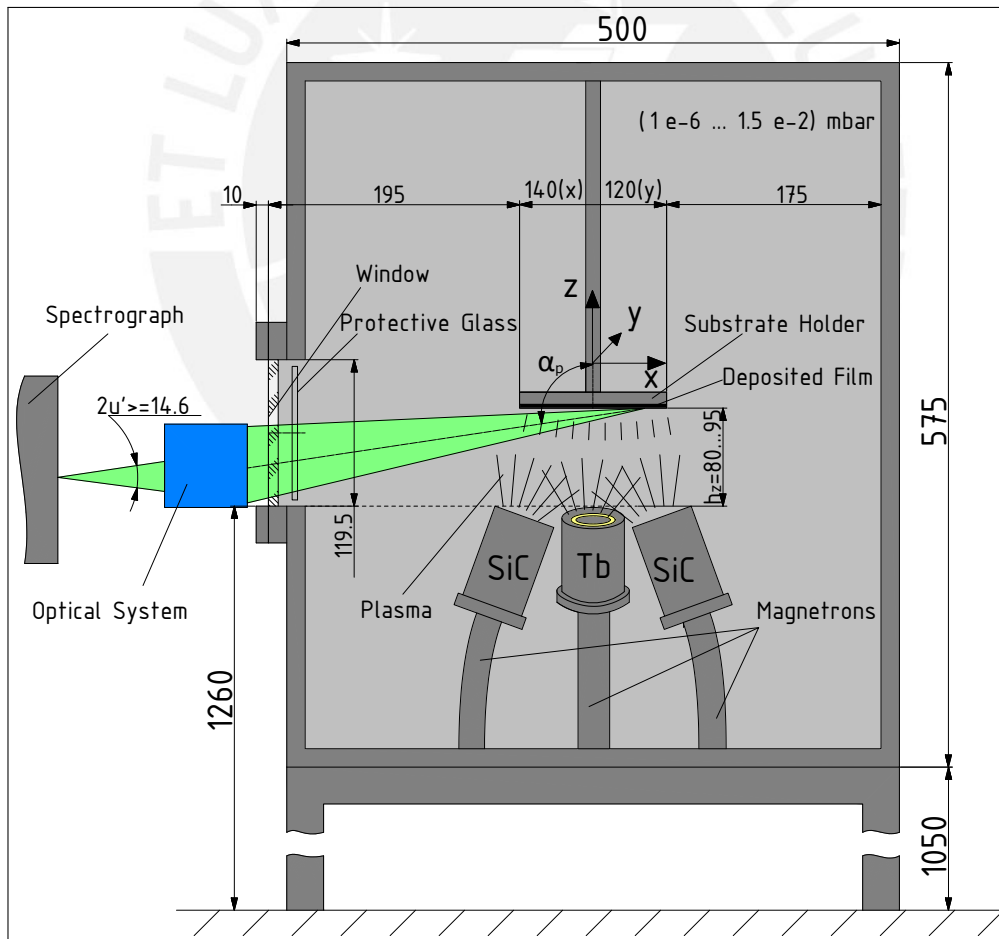


Figure 2.2: Visualized geometrical requirements of the system.

## 2.2 Utilised Spectrograph

### 2.2.1 Description

To analyse the spectra, a Czerny-Turner-Spectrograph from ORIEL INSTRUMENTS (model 74086) is used.

Its micrometer driven entrance slit (model 74001) is adjustable from  $4 \mu m$  to  $3000 \mu m$  width.

A curved mirror ( $f = 250 \text{ mm}$ ) collimates light from the slit onto a grating (model 77986). The grating has a spectral range from  $280 \text{ nm}$  to  $1400 \text{ nm}$  and a peak efficiency of  $80 \%$  at  $500 \text{ nm}$ . Another curved mirror ( $f = 250 \text{ mm}$ ) refocusses the dispersed slit image onto one of the two exit ports. These can be switched by electronically flipping a mirror inside the spectrograph. One port is equipped with a LINESPEC CCD-detector (model 7885). The other port has an exit slit of the same model as the entrance slit.

The *reciprocal linear dispersion* is defined as [PL05]

$$P = \frac{d \cos \beta}{mr'}, \quad (2.1)$$

where  $d$  is the grating's grooves' width,  $\beta$  the diffraction angle,  $m$  the diffraction order and  $r'$  the focal length.  $P$  gives a ratio between change of wavelength  $\lambda$  and its corresponding distance  $L$  on the detector:

$$P = \frac{d\lambda}{dL} \quad (2.2)$$

Equation 2.1 shows that  $P$  is a function of  $\beta$ , while  $\beta$  varies over  $\lambda$ . Nevertheless, the *reciprocal linear dispersion* is given as a fixed value  $P = 3.2 \frac{nm}{mm}$  for the used grating-spectrograph combination in ORIEL data sheets. It represents  $P$  at the blaze wavelength.

The used spectrograph is not calibrated yet. To get an idea what wavelength difference  $\Delta\lambda_{pix}$  one pixel on the detector roughly represents, the following assumption is made:

$$\Delta\lambda_{pix} = P \cdot L_{pix} = 3.2 \frac{nm}{mm} \cdot 14\mu m = 0.0448 \text{ nm}, \quad (2.3)$$

where  $L_{pix}$  is the distance between two pixels. This value leads to an assumed detector bandpass  $B_{det}$  of

$$B_{det} = P \cdot L_{pix} = 2048 \cdot 0.0448 \text{ nm} = 91.75 \text{ nm}. \quad (2.4)$$

The values calculated in 2.3 and 2.4 must be seen as a rough assumption that is used in the thesis. Contrary to the grating's actuator, the spectrograph's CCD-detector is not calibrated yet. Around the blaze wavelength, the values should be rather exact. In other parts of the spectrum, greater errors are made by using them to determine the represented wavelength of a pixel.

## 2.2.2 Defocus

The spectrograph, as shown in figure 2.3 and used in this work, is defocused. The CCD-detector is not located in the focal plane but closer to the curved mirror. Thus, the entrance slit does not lie within the object field, which is located further away from the curved mirror's focal plane. The entrance slit is projected defocused onto the image field, which leads to a loss of peak intensity and spectral resolution. Furthermore, spectral shifts occur when the direction of entering light changes, as shown in figure 2.4. Before the spectrograph gets calibrated, the CCD should be moved to its intended plane.

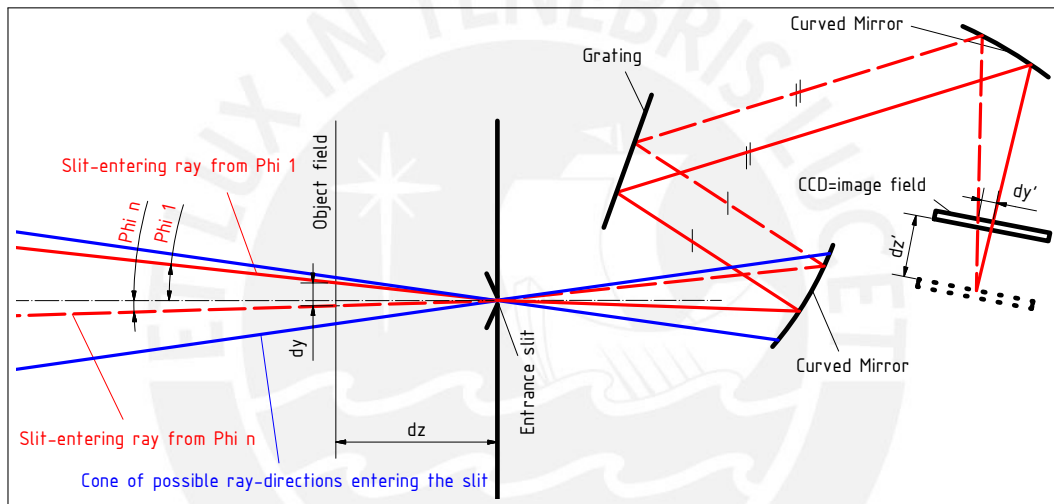


Figure 2.3: Scheme of utilised spectrograph. The Detector is defocused for  $dz'$ . The object field is shifted from the entrance slit for  $dz$ . The defocus leads to a loss of spectral resolution and possible spectral shifts  $dy'$ .



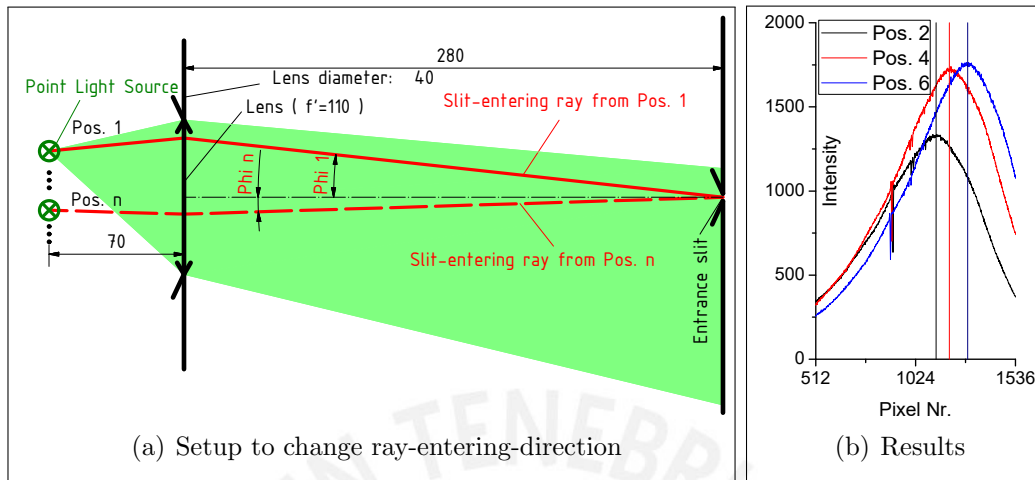


Figure 2.4: Spectral shift by changing entering ray direction. (a) A lens is positioned in front of the spectrograph's entrance slit. By moving a point light source (in this case an LED) laterally to the optical axis of the lens (Pos. 1...Pos. n), the direction of the rays which enter the slit changes. (b) Shifted spectra resulting from different positions of the point light source.

## 2.3 Requirements

This section enumerates and quantifies the system's requirements. Obligatory requirements are necessary to fulfil basic needs of the system. Desirable requirements are additional functions to simplify the device's use or add further possibilities to the spectral analysis.

- (O) - obligatory
- (D) - desirable

### 1. Spectroscopy of substrate- and plasma emission

The main purpose of the device will be to measure light intensities from the light emitting Tb in the substrate. The spectrum is necessary to identify the Tb as a light source.

While the Tb doped film is observed, there is always plasma emission in the optical path. It is not possible to get an isolated spectrum of the substrate's Tb emission during the sputtering process. Because there is also excited Tb inside the plasma, it emits in the same spectral region as the substrate. To get the excited substrate's spectrum, the plasma spectrum must be filtered out of the spectral superposition.

The plasma spectrum itself is also a quantity of interest as it gives information about the plasma's composition.

- (a) (O) spectroscopy of substrate emission
- (b) (O) spectroscopy of plasma emission
- (c) (O) separation of superpositioned substrate- and plasma spectrum

## 2. Flux distribution in entrance slit

The spectrograph images its entrance slit onto a detector which measures the image's distribution of illumination intensity. The image position depends on wavelength and the grating's type and orientation. Assuming that monochromatic light enters the slit, just one image of the slit is produced on the detector. If there is a peak of luminance changing its position within the slit, there will be also a shift of illumination measured by the detector. This effect can get stronger with larger slit widths, limiting measuring accuracy. Imaging a FoV from the spatially inhomogeneously emitting substrate onto the slit area can lead to this spectral shift and must be avoided. The image must be "destroyed" by a homogenizing element before entering the entrance slit.

- (a) (O) spatial information of FoV must be destroyed

## 3. Image-space aperture

The spectrograph's aperture is given by its f-number  $f'/D = 3.9$  [New16]. This conforms to an aperture with a half angle of

$$\theta_{spec} = \arctan(1/(2 \cdot 3.9)) = 7.306^\circ.$$

Light entering the entrance slit from outside of the "acceptance pyramid/-cone", as shown in figure 2.5, should be avoided [New15, PL05].

- (a) (O) f-number:  $f'/D = 3.9$
- (b) (D) prevent stray light outside cone of acceptance

## 4. Throughput

The system's throughput depends on its étendue and the optical efficiencies of its components. The thin film as light source emits relatively weakly, which means that unnecessary losses due to the spectrograph's possible upstream components (fibres, lenses, windows,...) should be avoided.



## 7. Spectral resolution

The Tb peaks mostly lie more than 35 *nm* away from each other. High resolution is not necessary to identify Tb as source of emission. An exception are the two major peaks at about 540 and 547 *nm*. Their visibility does not only depend on the spectrograph's resolution but also on the used matrix and its degree of crystallinity. Due to the amorphous character of the deposited matrix, the Tb-lines get thicker and are less distinguishable than in 1.5b.

- (a) (O) min. spectral resolution: < 20 *nm*
- (b) (D) min. spectral resolution: < 5 *nm*

## 8. Calibration of the system

It shall be possible to calibrate the Spectrograph. For each orientation of the grating. Every pixel shall be assignable to a certain wavelength.  
(O)

## 9. Field of View (FoV)

To scan the substrate's surface more effectively, the FoV should be as small as possible. According to the laws of étendue (see section 1.7), its size depends on the slit's (image's) extent and the object space aperture. Depending on the objective's position, the substrate will be observed from an inclined angle, and not from a perpendicular direction to its surface. This can lead to a distortion of the FoV's shape.

- (a) (O) maximum extent: < 20 *mm*
- (b) (D) maximum extent: < 1 *mm*
- (c) (D) shape: circle or square
- (d) (D) distribution of light collection: homogeneous
- (e) (D) variable extent: (1...50) *mm*

## 10. Every position on substrate measurable

As seen in figure 1.5a, the emission intensity of the Tb has a certain distribution over the substrate holder. Depending on the process settings, the location of maximum light intensity can change within a few minutes. Being able to observe every position on the substrate holder is necessary. The substrate holder's height can vary in a range of 15 *mm*. Moreover, the plasma between substrate and magnetrons shall be observable. The focus position needs to be movable within the following ranges (directions according to coordinate system in figure 2.2):

- (a) (O) in-situ scans of substrate surface must be possible
- (b) (O) movement range of focus (substrate):
  - $x \geq 100 \text{ mm}$
  - $y \geq 160 \text{ mm}$
  - $z \geq 15 \text{ mm}$
- (c) (O) observability of plasma:  $z \geq 80 \text{ mm}$
- (d) (D) low scan time 50 spots in  $< 10 \text{ min}$

#### 11. Know which spot is observed

The substrate holder does not have a very stable position and orientation and its height gets adjusted. Furthermore, the probes get exchanged and their position on the substrate holder can change.

To ensure that the objective has its focus on the substrate plane, it needs to be observable. Thereby, also its adjustment to a reference spot on the substrate should be possible to set reproducible scanning conditions.

- (a) (O) position of FoV can be made visible
- (b) (O) form of FoV can be made visible
- (c) (O) repeatability of FoV's position:
  - $x < 1 \text{ mm}$
  - $y < 1 \text{ mm}$
  - $z < 1 \text{ mm}$
- (d) (D) reference point on substrate

#### 12. Available space outside the Chamber

As seen in figure 2.1, there is plenty space on the left, right and front side of the chamber. Left- and front side include a window. The front side should be kept free for accessibility purposes. The device will probably be located on the left side. The control panels left of the chamber should stay easily accessible.

Spatial restrictions in case of putting the device on the left side of the chamber (directions according to coordinate system from figure 2.2):

- (a) (O) max. spatial extent:
  - $x < 750 \text{ mm}$
  - $y < 400 \text{ mm}$
  - $z < 2000 \text{ mm}$
- (b) (D) compact system preferred:
  - $x < 250 \text{ mm}$
  - $y < 300 \text{ mm}$
  - $z < 450 \text{ mm}$
- (c) (D) spatial separation of spectrograph from objective

13. **User friendly assembly and disassembly**

If space occupied by the construction is needed for other applications, it should be easy to take the construction off the chamber. It should also be easy to reassemble it. (D)

14. **Vacuum inside chamber**

There may be modifications of the chamber, or parts are placed inside it. These modifications must not severely affect the vacuum or the process in general and they also must not be severely affected by those:

- (a) (O) forces occurring due to pressure difference must be considered
- (b) (O) no additional particle leakage from outside the chamber
- (c) (O) no strong particle leakage from parts inside the chamber

15. **Protection from contamination by sputtering process**

To guarantee a long termed constant spectral sensitivity of the construction, optically important parts need to be protected from contamination by sputtered particles. (D)

16. **Automatic motion shall be possible**

To scan the substrate's surface automatically and more efficiently, slots for automatic actuators shall be considered to move the FoV into the following directions (according to coordinate system of figure 2.2):

- (a) (D) automatic movement of FoV: x-direction
- (b) (D) automatic movement of FoV: y-direction

17. **Cost**

The budget for parts and fabrication is  $< 5000 \text{ €}$  (O)

# Chapter 3

## State of the Art

An investigation of solutions to capture light for Optical Emission Spectroscopy (OES) has been done. The results are summarized in this chapter.

In [AA14, RWS99] (figure 3.1a) the fibre is brought close to the plasma through a transparent pipe, which is exchanged after every deposition cycle. Figure 3.1b shows fibre ends which are modified with refractive and reflective elements to change ray profiles (3.1b, top+bottom) and entering directions (3.1b, bottom) into the fibre. If brought very closely to the object, like in figure 3.1a, these modifications could be used to obtain a very large aperture and a small FoV. A change of the light's entering direction could be useful to simplify a construction which shall be able to scan the entire substrate's surface and the plasma.

In [Naw11, MIE<sup>+</sup>01, OLZ<sup>+</sup>13], the plasma emission was directed through a chamber window and a lens system into the fibre. Figure 3.2 shows a system where the lens captures collimated light from the plasma through a window into the fibre. This means that light is captured from a large FoV. Simple repositioning of the lens would allow to focus a certain spot in the plasma or on the substrate.

In Laser Induced Breakdown Spectroscopy (LIBS) [MP14], a pulsed laser generates a small plasma plume on the substrate's surface. As seen in figure 3.3, a high aperture of the "light collection unit (5)" is necessary to effectively channel light from the tiny exited spot into the spectrometer (6).

The shown principles can be designed in a way that the focus position can be changed spatially by moving the fibre end and/or the lens system. Thereby, the required scan of the substrate surface would be possible.

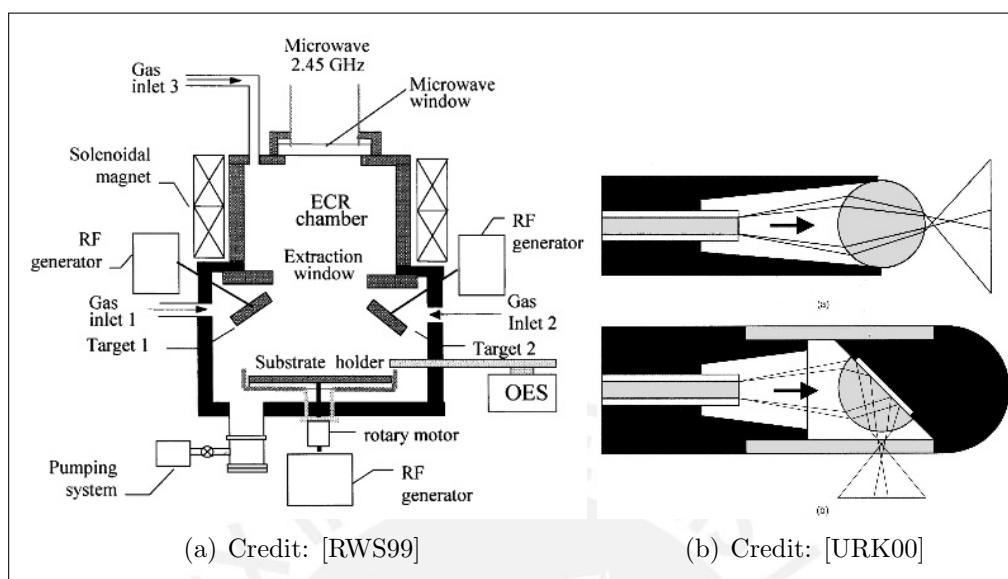


Figure 3.1: (a) OES quartz pipe set-up in sputtering process. Fibre end is brought very closely to plasma by a quartz pipe, which is exchanged after every process. (b, top) Refractive element directly built onto fibre entrance to change ray profile. (b, bottom) Additional reflection of rays to 90°-angle.

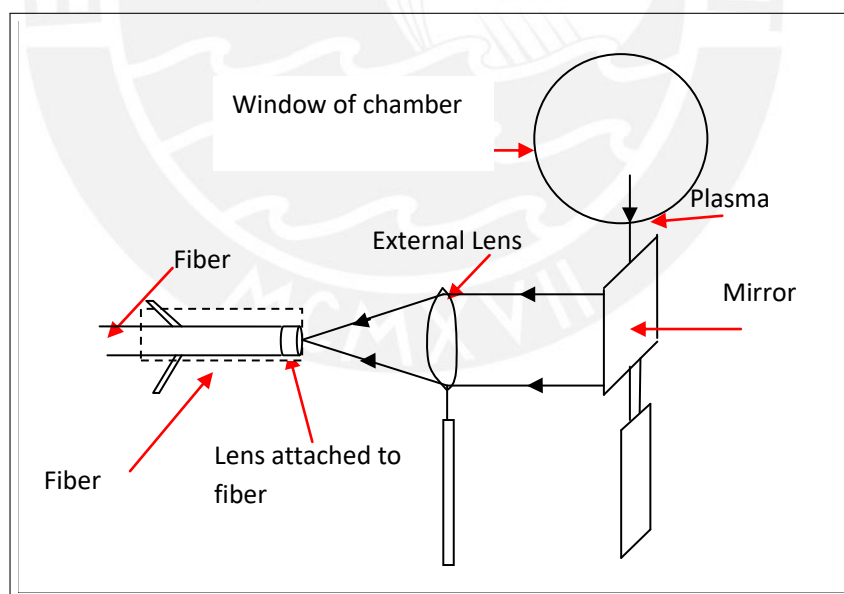


Figure 3.2: Light is directed through window and lens system. Credit: [Naw11]



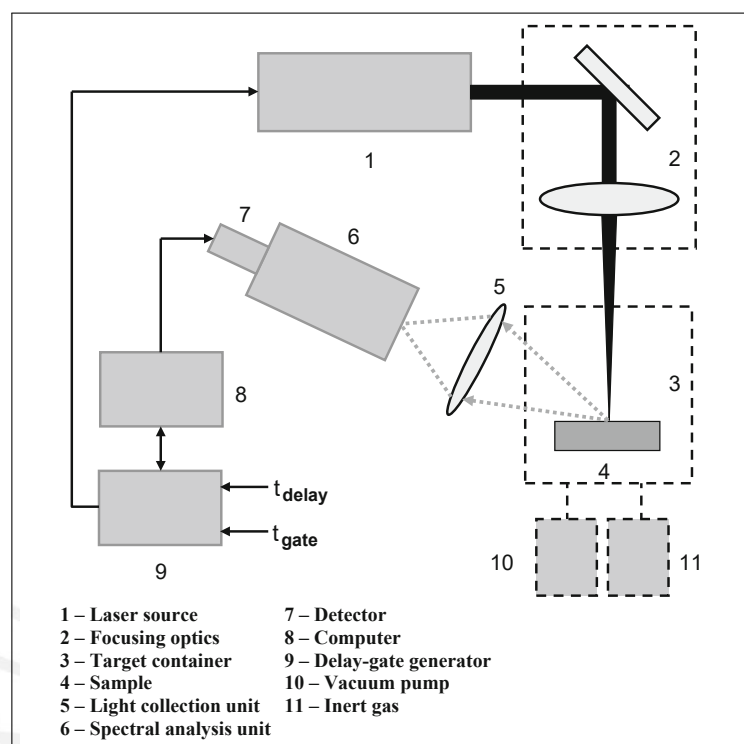


Figure 3.3: In LIBS, a small field gets excited by a focussed and pulsed laser beam. The emission is captured by a spectrometer (6) due to a "light collection unit" (5). Credit: [MP14].

[Law13] shows techniques to maintain spatial information within the spectrograph. Less movements are necessary to scan the object space, which can potentially simplify the mechanical construction. Furthermore, scanning time can be saved.

A simple technique is *long-slit-spectroscopy*, as shown in figure 3.4. Along the slit's one-dimensional extent, spectra of spatially separated objects can be distinguished by their position on a two-dimensional detector plane.

To get spectra of two-dimensionally distributed objects, the slit can be replaced by a *slit mask*, which contains slits on each spot complementary to the required object positions. Depending on the spectra's extent and the slits' arrangement, an overlap of spectra is possible and should be avoided.

Figure 3.5 shows another way to get spectra from spots on a two-dimensional object field. Light is captured from relevant spots on a "focal plane" with "lenslets" and fibres. The fibres can then be arranged along the slit so that the spots' spectra can be read out separately.

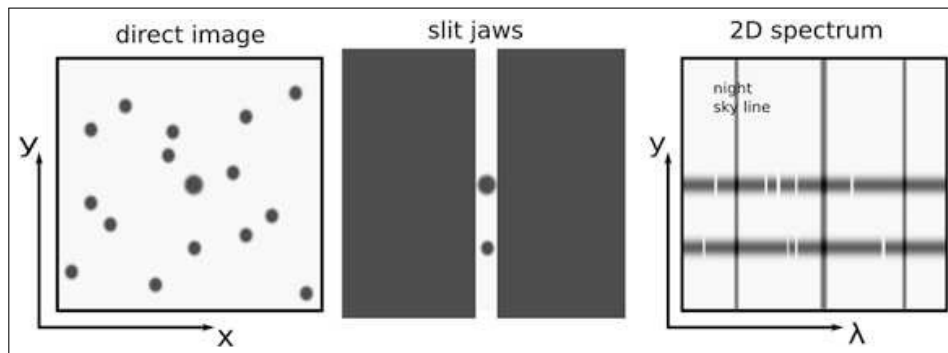


Figure 3.4: (Left) intermediate image plane (slit plane). (Middle) perspective through slit jaws. (Right) spatially separated spectra of objects along the slit on detector plane (e.g. CCD-matrix). Credit: [Law13]

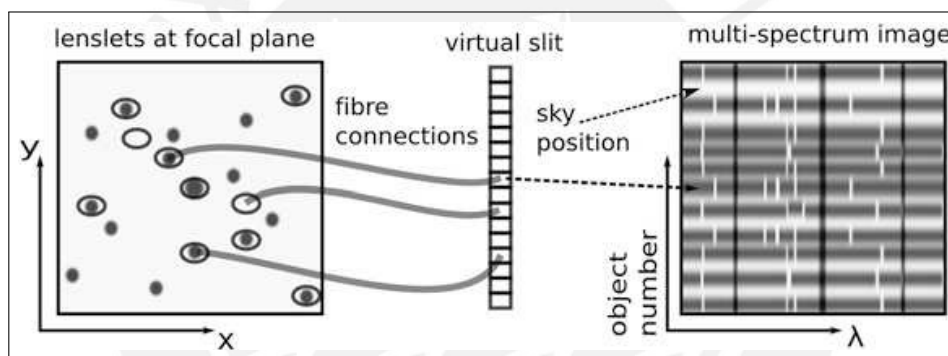


Figure 3.5: (Left) intermediate image plane with lenslets and fibre entrances put on relevant objects. (Middle) rearranging fibre exits between slit jaws. (Right) spatially arranged and separated spectra of objects on detector plane. Credit: [Law13]

The given examples show that there are several solutions for similar problems as the one faced in this work. Usually, not a processed surface, but the plasma is analysed in OES of plasma involving Physical Vapor Deposition (PVD) and Chemical Vapor Deposition (CVD). In the majority of cases, deposited films do not emit light during the deposition process. Setups with an objective behind the chamber window, as well as setups with optics very close to the probe object can possibly focus onto finite object spots on the substrate. With optics brought closely to the probe object, generally smaller FoV are possible as the apertures are not limited by a window's extent. However, the necessary movements of the optical parts in several DoF are more difficult to realize.

In nearly all cases showed in this chapter, optical fibre was used to channel light from an object (plasma spot/area or celestial body) into the spectrometer. Next to its light-homogenizing abilities, it is very useful to be able to keep functional elements spatially separated from each other. However, additional light losses must be considered.

Furthermore, simultaneous spectral analysis of multiple points at a time are possible with certain fibre arrangements, but construction effort and costs would increase with such arrangements.

The solutions presented in this chapter are partly discussed in chapter 5.



# Chapter 4

## Experimental Verification of a basic optical Assembly

### 4.1 Assembly

First, a simple prototype system is set up to spot errors, difficulties and opportunities for the system that shall be developed.

The Spectrograph, on a table outside the chamber, is aligned to the substrate, as shown in figure 4.1. A window in the left chamber wall enables an optical path between substrate and entrance slit. A lens ( $f \approx 115 \text{ mm}$ ) images a point of the substrate onto the spectrograph's entrance slit, as shown in figure 4.2a. Apart from its detector, a mirror can change the optical path inside the spectrograph to another exit slit. A laser is used to send light through the exit slit to illuminate the entrance slit, which then gets imaged onto the substrate. Thereby, information about focus and position of the observed point can be obtained. By moving the lens in x-, y- and z-direction, the observed location can be adjusted. Behind the substrate, a black body is placed to prevent the measurements from unwanted reflections from the aluminium foil on the chamber walls, as shown in figure 4.2b.

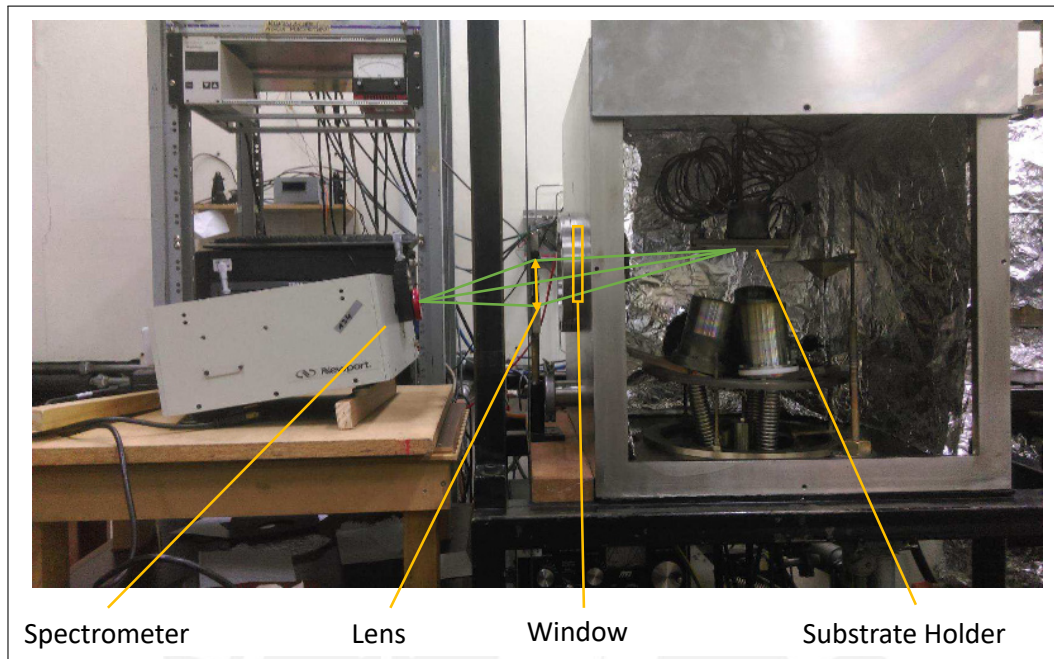


Figure 4.1: Construction of a first test assembly to measure Tb emission.

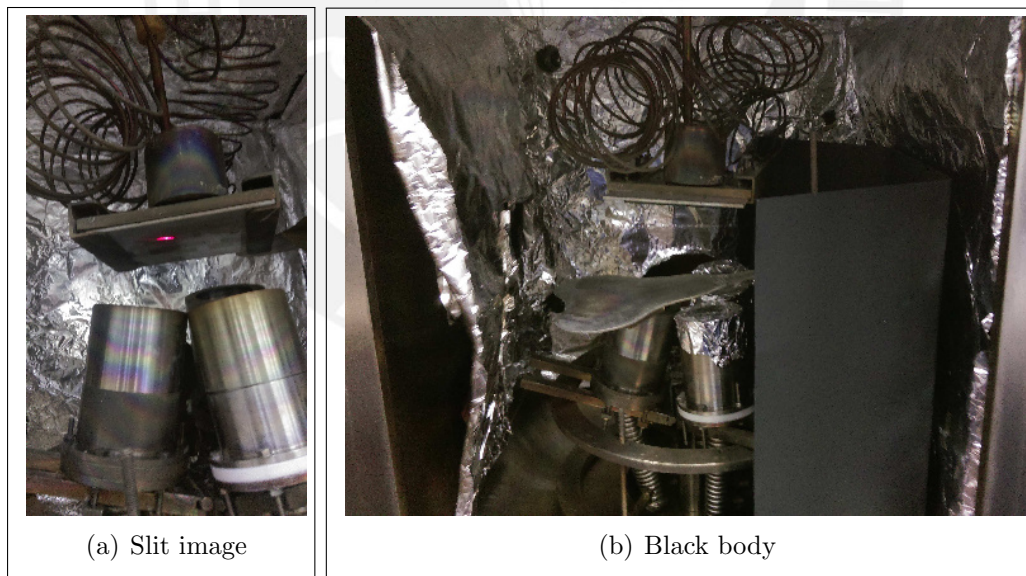


Figure 4.2: (a) Imaging slit on substrate by letting laser light enter the spectrograph's exit slit. (b) Representative picture of black body behind substrate to prevent measurement from stray light. For the actual test, a black matt polymer case was used because cardboard would worsen the vacuum conditions too much.

Parameters of process and measurement	Value
Power Magnetron Si	100 W
Power Magnetron Tb	10 W
Substrate height (ruler value on top of chamber)	3.5 cm
Lens focal length	$\approx 115$ mm
CCD Integration time	1000 ms
Slit width	0.5 mm
Range of measurement	(300...900) nm

Table 4.1: Details of Prototype System Test

## 4.2 Description of experimental Procedure

Emission spectra of Tb and plasma during a sputtering process are taken. The raw signal, taken from the CCD-detector, is a superposition of its dark signal and the actual signal. In a first step, the dark signal is subtracted, as shown for the main Tb-peak in figure 4.3b. To capture the dark signal, the shutter is closed. The dark signal is then measured with the integration time of the actual measurement.

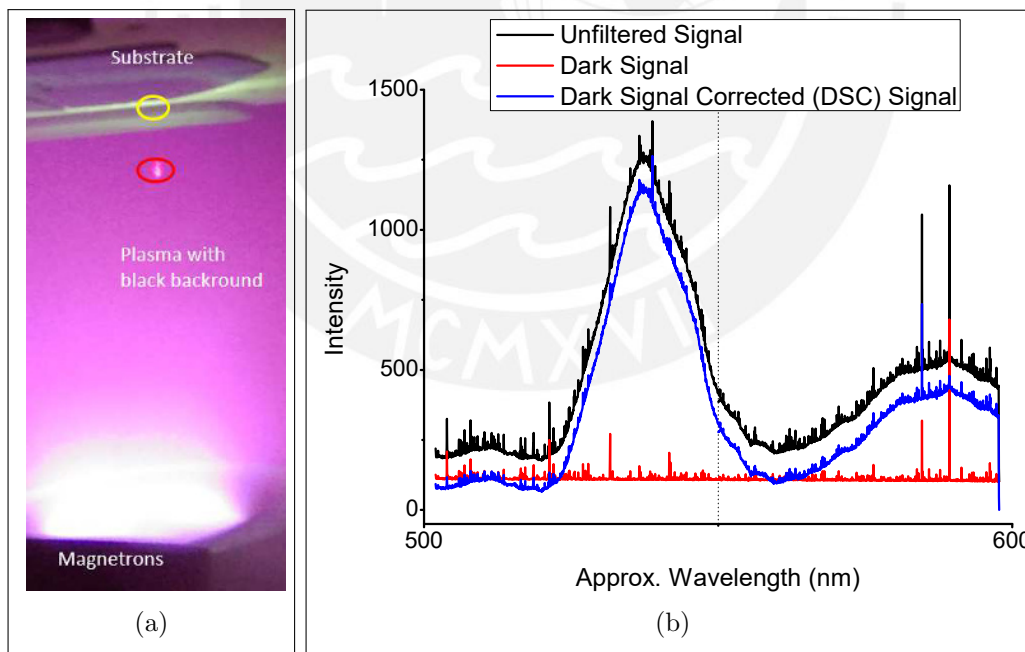


Figure 4.3: (a) (Yellow) Observed spot on substrate. (Red) Observed spot just on plasma. (b) Subtracting dark signal (red) from raw signal (black) to get corrected spectrum.

In figure 4.4, spectra of the process emission are taken for  $\lambda = (300\dots900) \text{ nm}$ . The detector's limited extent just allows to measure a bandpass of  $B_{det} \approx 90 \text{ nm}$ , as demonstrated in Equation 2.4. The grating has to be redirected to make all sectors of the observed range visible. For this experiment, the grating is moved to six different wavelengths. In figure 4.4, these wavelengths are marked with vertical lines. The bandpass is smaller than the intervals of movement, which means that values for wavelengths around each full hundred are not plotted in the graph. The spectrograph is not calibrated yet. The same bandpass  $B_{det}$  and correlation factor  $\Delta\lambda_{pix}$  are used for each sector, which leads to mapping errors.

As mentioned in 2.2.1-1, the Tb-signal  $I_{Tb}(\lambda)$  must be separated from the spectral superposition with the plasma signal  $I_{Pl1}(\lambda)$ :

$$I_{superp}(\lambda) = I_{Tb}(\lambda) + I_{Pl1}(\lambda) \quad (4.1)$$

In figure 4.4a, the Tb superposition signal  $I_{superp}(\lambda)$  is taken from the substrate's surface. Also a just-plasma signal  $I_{Pl2}(\lambda)$  is obtained by moving the observed spot to a place closely beneath the substrate (figure 4.3a).

Next, a wavelength  $\lambda_p$  is chosen that exhibits plasma emission but no Tb emission so that

$$I_{superp}(\lambda_p) = 0 + I_{Pl1}(\lambda_p). \quad (4.2)$$

In this case, the plasma peak at  $\lambda_p \approx 740 \text{ nm}$  is taken. Assuming that each pixel has a constant signal-to-flux ratio, the following generalization is made:

$$\frac{I_{Pl1}(\lambda_p)}{I_{Pl2}(\lambda_p)} = k = const = \frac{I_{Pl1}(\lambda)}{I_{Pl2}(\lambda)}, \forall \lambda. \quad (4.3)$$

By multiplying the just-plasma spectrum by  $k$ , it represents the plasma part of the superposition spectrum (figure 4.4b):

$$I_{Pl1}(\lambda) = k \cdot I_{Pl2}(\lambda) \quad (4.4)$$

The superposition signal gets subtracted by its plasma part. Hence, just the Tb-spectrum remains (figure 4.4c):

$$I_{Tb}(\lambda) = I_{superp}(\lambda) - k \cdot I_{Pl2}(\lambda) \quad (4.5)$$

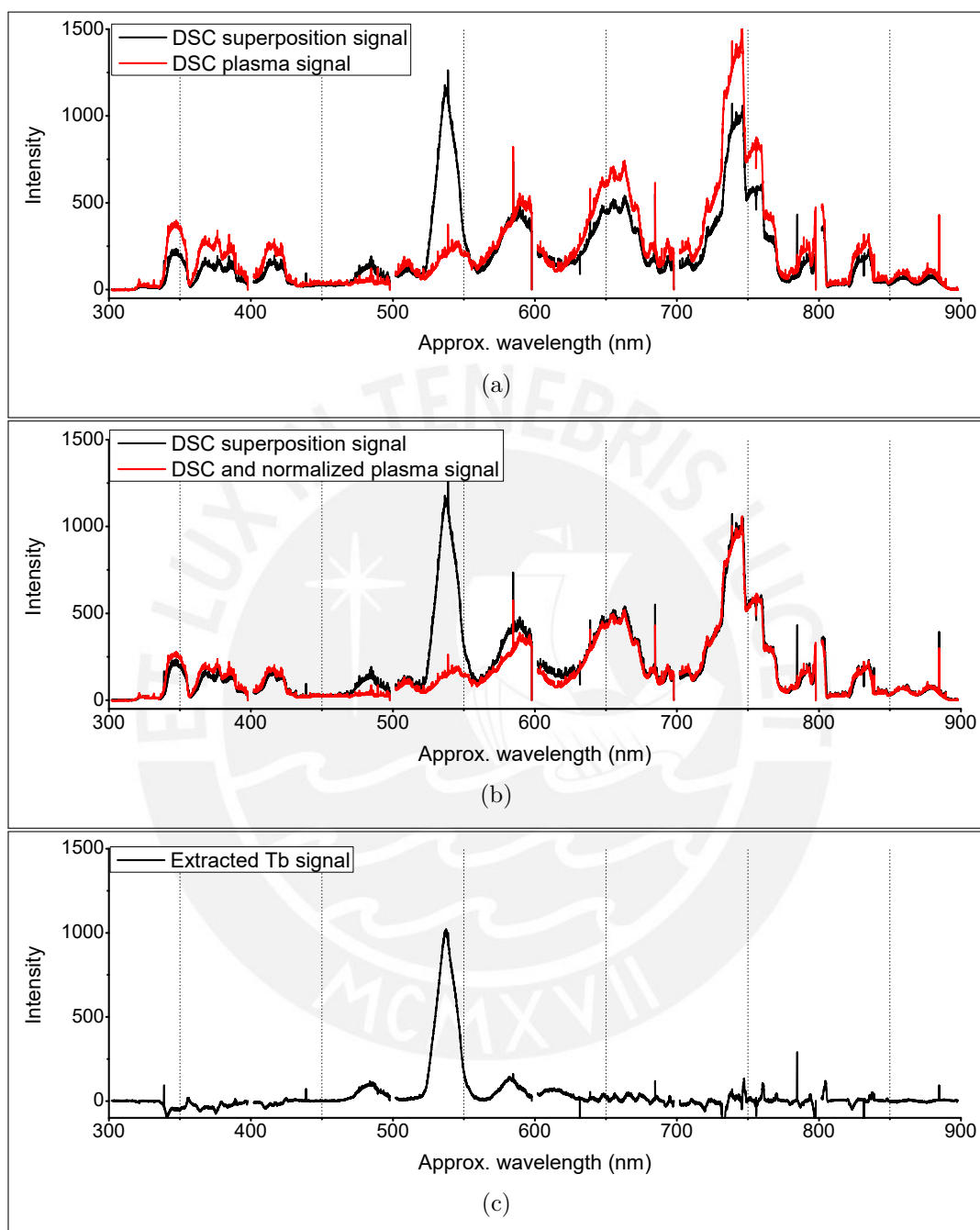


Figure 4.4: (a) Dark Signal Corrected (DSC) spectrum captured from substrate surface (black) and spectrum from plasma only (red). (b) Intensity of plasma spectrum gets normalized to substrate's spectral intensity. (c) Tb spectrum gets extracted by subtracting normalised plasma spectrum from superpositioned substrate surface spectrum.



### 4.3 Discussion of Results

Under the given conditions, the Intensities were sufficient to spot each of the four main peaks of the Tb spectrum, which could be successfully extracted from the superposition signal, as shown in figure 4.4. It must be mentioned that the Tb's light emission was relatively strong in comparison to former deposition cycles.

The calculated peak wavelengths lie at (483, 537, 583, 613) *nm*. They differ up to 8 *nm* from literature values<sup>1</sup>. Main cause for this difference is probably the inaccurate mapping method, described in section 2.2.1 and section 4.2. The low intensity of the minor peaks in combination with their large width could also influence the obtained peak position.

Especially the main peak looks very similar to the curves in figure 4.5. A slight "shoulder" on its right side is visible, but the curve does not split up into two peaks, like in figure 1.5b. The graph in figure 4.6 is captured with a five times higher resolution, which does not have consequences on the curve's form. Therefore, the double peak's non-visibility is assumed to depend on the matrix' material and its amorphous state, rather than on the spectrograph's resolution.

Between (330...440) *nm* and (630...840) *nm*, there are a lot of disturbances in the extracted Tb spectrum. Tb does not emit in these sectors. One reason could be a lack of repeatability of the grating's actuator. If the normalized plasma signal in figure 4.4b is not totally coincident with the superposition signal, its subtraction could lead to the seen disturbances. In figure 4.7, the originally extracted Tb spectrum between 700 *nm* and 800 *nm* is compared to a version where the normed plasma spectrum from figure 4.4 is shifted 9 pixels<sup>2</sup> aside before being subtracted from the superposition signal. The peak-to-valley distance is reduced by 45 % from 301 to 166 intensity points. Although this behaviour speaks for the proposed lack of repeatability, there are still peaks and valleys left in the curve of the shift result. Other factors, like inhomogeneous slit illumination or differences in the signals' plasma composition due to their recording at different spots and times, could play a role.

---

<sup>1</sup>Tb peaks at (489, 544, 583, 621) *nm*, according to [BRR05]

<sup>2</sup>+9 · 0.0448 *nm* ≈ +0.4 *nm* according to equation 2.3

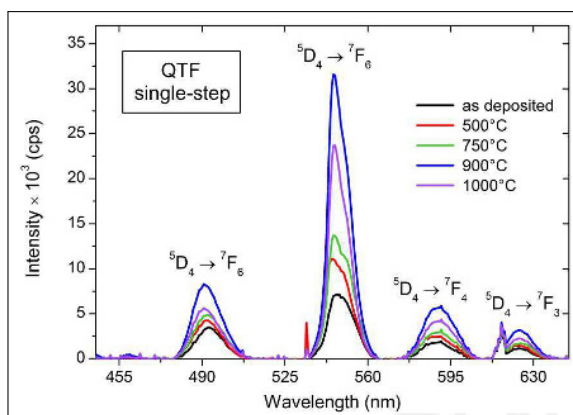


Figure 4.5: CL spectrum of Al doped with Tb at different annealing temperatures. Credit: [TS16]

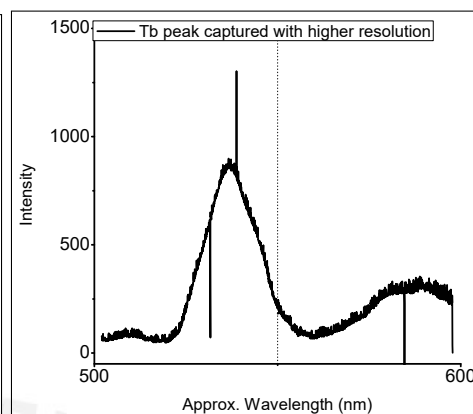


Figure 4.6: Superposition of major Tb peak and plasma captured with  $0.1 \text{ mm}$  slit width and  $5000 \text{ ms}$  integration time.

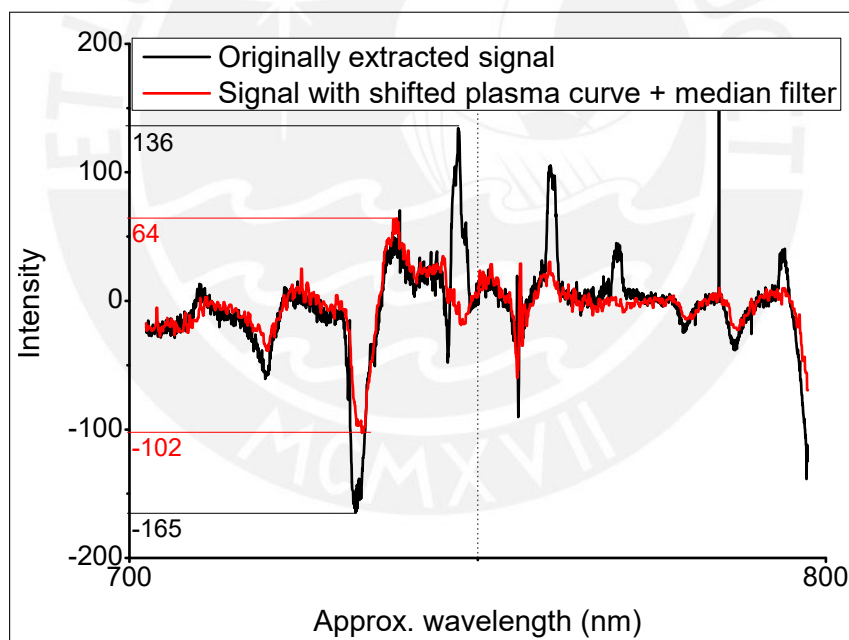


Figure 4.7: (Black) originally extracted spectrum at  $(700\dots800) \text{ nm}$ . (Red) gained spectrum after shifting the normalized plasma spectrum (figure 4.4b) by  $+0.4 \text{ nm}$  and then subtracting it from the superposition spectrum. A median filter is applied to filter noise effects generated by assigning different pixels to each other, which can differ in their sensitivities due to the shift.

# Chapter 5

## Discussion and Evaluation of potential Solutions

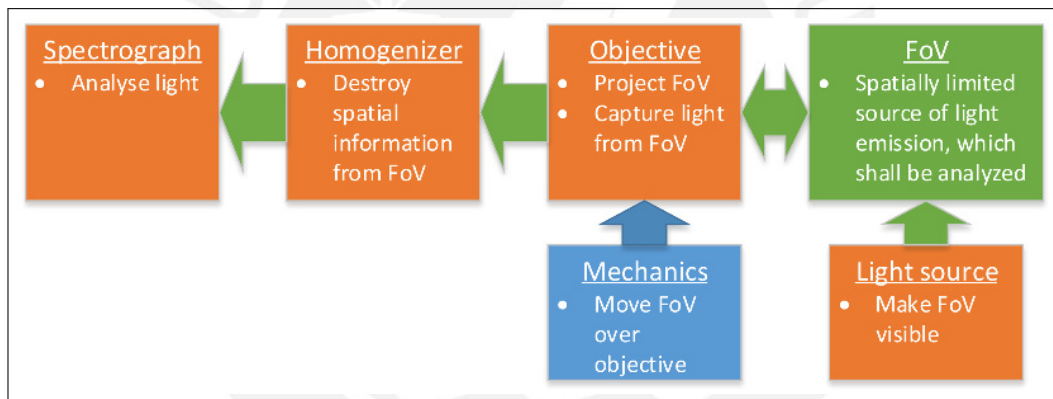


Figure 5.1: Function structure of optomechanical system.

The prototype system already showed good results, especially in terms of the captured emission intensity. Nevertheless, it does not prevent the entrance slit from spatially and directionally inhomogeneous illumination. This can cause spectral shifts and form errors in the spectral curves. There are different ways to construct the final system in terms of light capturing, homogenization and FoV positioning, which are discussed in this chapter.

Choices are made by the use of evaluation tables for each part function. The tables compare the solutions by relevant criteria, which gain individual *weight*  $W$ . Depending on the solution's fulfilment of the *criterion* "*Crit*", it gets a *grade*  $G$  from 1 to 6.  $G$  gets multiplied by  $W$  to a certain number of *points*  $P$ . The solution with the highest sum of points  $\sum P$  of all applied criteria shall be chosen.

The following criteria are applied to evaluate the solutions:

- **Optical Efficiency (OE, W=5)** is the most important factor because it determines the spectrograph's accuracy fundamentally by reducing the signal-to-noise ratio, while simultaneously allowing narrower slit widths for higher spectral resolution.
- **Constructional Practicability (CP, W=4)** is the grade of how much time and effort a construction of the system takes, how much risk is combined with it and how convenient its use of space is.
- **Applicability (A, W=4)** is a measure of how "user friendly" the system will be and how fast measurements of different positions on the substrate can be taken.
- **Comparability of Measurements (CM, W=3)** shall describe how similar the FoV are in their form and extent on different positions on the substrate.
- **Spatial Resolution (SR, W=3)** is a grade of how small the FoV's extent is and how distorted it is on the substrate. This depends on object space aperture and the angle from which the substrate is observed.
- **Grade of Homogenization (GH, W=3)** represents the capability to prevent spectral changes because of spatially inhomogeneous emission distributions within the FoV.
- **Cost (C, W=2)**

Each criterion is just used if it is relevant to the part function and if the solutions are estimated or known to differ in their performance in this regard.

## 5.1 Optics Placement

A fundamental question is whether there shall be optics inside the chamber or not, which will be discussed in this section.

### 5.1.1 Optics inside Chamber

The main advantage of placing optics inside the chamber would be a significant possible increase of the object space aperture due to a smaller distance between substrate and objective. According to equation 1.10, this would lead

to a smaller FoV. There would also be more freedoms in terms of perspective. The substrate could be observed from a more obtuse angle, leading to a less distorted FoV. These advantages would lead to a higher spatial resolution. Repositioning the FoV in at least three degrees of freedom (DoF) is necessary in order to scan the substrate on every position (requirement 10d in section 2.3). There is very limited space available inside the chamber to move optics over these ranges. Furthermore, the movement would need to be controlled from outside of the vacuum chamber. It also would be necessary to modify the chamber. Functional entrances and seals would need to be used, which would cause additional risk of leaks that influence vacuum quality. The mechanical implementation would be more difficult and risky with optics inside the chamber.

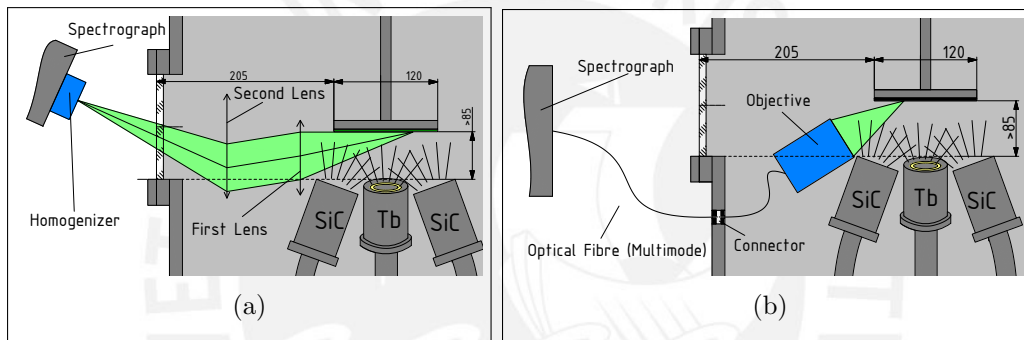


Figure 5.2: Examples of optics inside the chamber. (a) Two lenses. First lens collimates light and gets moved to change position of FoV. Second lens refocusses collimated light into a homogenizing element connected to the spectrograph's entrance slit. (b) Objective connected to the spectrograph with an optical fibre. Entire objective is moved to change FoV's position.

Two examples of a possible arrangement are briefly introduced. The FoV's position could be changed by moving two lenses relatively to each other like in figure 5.2a. Refocussing under similar optical conditions and within the available space would be rather difficult.

In figure 5.2b, the FoV's position is changed by moving the whole objective, which is connected to an optical fibre. Due to a vacuum adapter and another fibre, the fibre is connected to the spectrograph outside the chamber.

Another variant of figure 5.2b would be a glass pipe, as shown in figure 3.1, which is movable in space, additionally. The fibre could be brought very closely to the substrate/plasma and could have a very high aperture. Due to its small geometrical extent, it also could be easier to manoeuvre during the scanning process. A disadvantage would be the direct presence in the sputtering zone. The deposition process would get influenced by the pipe's

shadowing of the substrate. The pipe itself would be strongly deposited with sputtered particles. The protective layer in its entrance would need to be exchanged very often.

For space saving- and reachability purposes, mechanical components, like gears and actuators, could be positioned outside the chamber and mechanically connected to the objective by a flexible tube, as shown in figure 5.3. However, because of the pressure difference, the mechanical parts would need to be dimensioned for high forces in direction to the chamber.

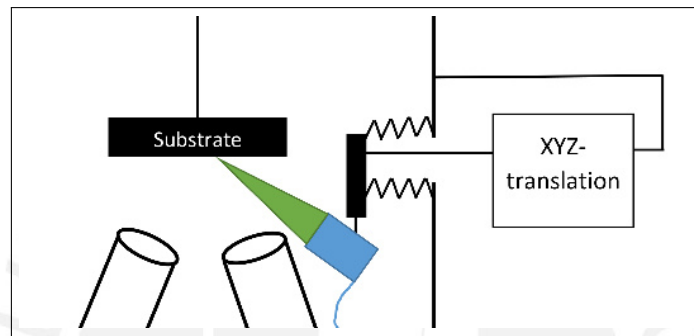


Figure 5.3: Sketch of a system with a flexible tube that makes positioning of actuators outside the chamber for objective motion possible.

### 5.1.2 Optics completely outside Chamber

In a construction completely outside the chamber, the relative position of window and substrate to each other would limit the objective's possible closeness. Due to the window's limited extent, also the object space aperture would be limited, which would lead to a bigger FoV, according to equation 1.10. It also would determine the optical axis' direction to the substrate plane to a very acute angle. Thus, the FoV would be significantly distorted. The spatial resolution while scanning the substrate would be significantly worse in comparison to a system with an objective inside the chamber. According to the laws of *étendue* (section 1.7), the amount of light that enters the spectrograph would be similar.

However, the mechanical construction would be comparatively easy. There is plenty of space available and all mechanical parts would be easily accessible by the user. There is also a variety of purchasable rotational and translational stages which would be appropriate for the rather rough necessary positioning accuracies (see requirement 10d in section 2.3).

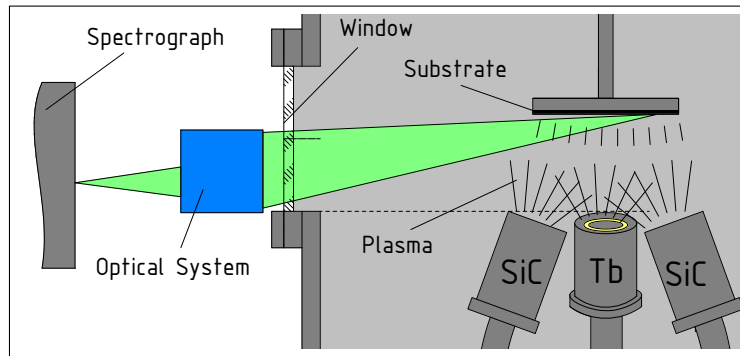


Figure 5.4: Sketch of an optical system which is placed totally outside the sputtering chamber.

### 5.1.3 Evaluation

Crit	W	Placement of optics			
		Inside chamber		Outside chamber	
		G	P	G	P
CP	4	2	8	6	24
SR	3	6	18	2	6
		$\sum P:$	26	$\sum P:$	30

Table 5.1: Evaluation Table: Placement of optical System

A movement in three DoF and within the necessary ranges would be difficult to realise inside the chamber as space and access possibilities are limited. The system will be constructed completely outside of the chamber. The construction will be similar to the already proven test assembly, which increases chances of a successful implementation.

## 5.2 Spatial Homogenization

In order to comply with requirement 2 of section 2.3, there are several ways to homogenize light.

### 5.2.1 Integrating Sphere

The integrating sphere is a very effective but expensive component to reach almost perfect homogenization. However, the optical efficiency is low with this variant.

To calculate the flux efficiency  $F$ , the following assumptions are taken: Both entrance- and exit hole are very small, compared to the sphere's completely lambertian reflective area so that the average reflection index  $\rho \approx \rho_{refl.area}$ . Furthermore, all light that enters the exit hole shall be channelled into the spectrograph's entrance slit. The fraction  $F$  of the incident flux entering the exit hole with an area  $a$  is [Goe67]:

$$F = \frac{a}{\pi \cdot D^2} \cdot \frac{\rho}{1 - \rho} \quad (5.1)$$

A common diameter for integrating spheres is  $D \approx 50.8 \text{ mm}$ . Assuming that  $a_{slit} = 1 \times 3 \text{ mm}^2$  and  $\rho = 0.99$ , just  $F = 3.7\%$  of the incident flux would enter the slit. Furthermore, light would enter the exit hole from each direction. Its aperture solid angle would be  $\Omega = 2\pi sr$ . According to the laws of *étendue* (section 1.7), light would enter the spectrograph's entrance slit with the same aperture because  $a = a_{slit}$ . This means that an even smaller part of the light would actually enter the entrance slit within the allowed f-number of the spectrograph. Hence, the total efficiency would be

$$\eta_{int} < 3.7 \text{ \%}.$$

## 5.2.2 Light Pipe

The degree of homogenization depends on the light pipe's length, form of its cross section, bending, direction- and spatial distribution of the incident light [Kos12].

Figures 5.5 and 5.6 show that under certain conditions, like a squared cross section or a special input angle, very homogeneous output profiles can be achieved. This would not necessarily be the best possible profile. A narrow gaussian intensity distribution, as given while using a circular light pipe with an input angle of  $0^\circ$ , could potentially increase the spectrograph's resolution. The most important requirement is constance of the output distribution.

Light pipes can be solid rods but also bendable cables, which would enable mechanical decoupling of the spectrograph from the objective. This could make the mechanical construction significantly easier.

The two main sources of light loss in light pipes are fresnel reflection (in case of a solid light pipe) and attenuation within the light pipe.



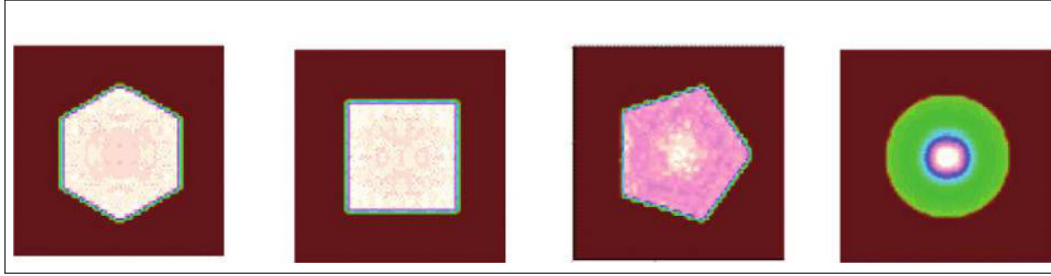


Figure 5.5: Light output distributions of light pipes with different cross sections. Credit: [Kos12]

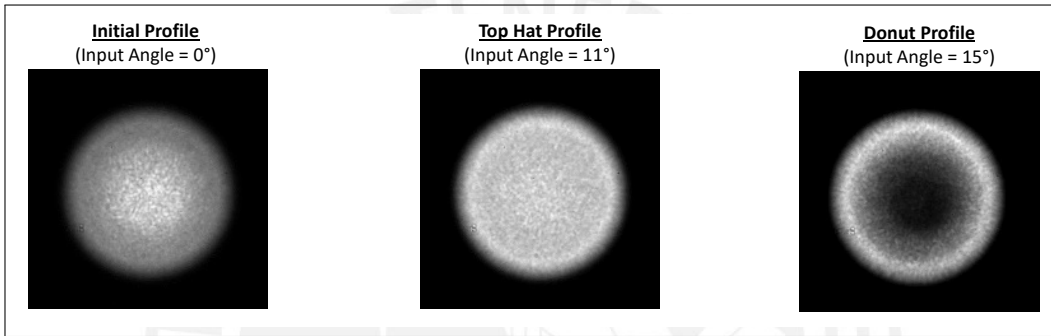


Figure 5.6: Light output distribution of fibre with different light input angles. Credit: [Tho]

The following equations describe the loss due to Fresnel reflection for non-magnetic materials [Haf03]:

$$R_p = \frac{\tan^2(\epsilon'' - \epsilon)}{\tan^2(\epsilon'' + \epsilon)}; \quad R_s = \frac{\sin^2(\epsilon'' - \epsilon)}{\sin^2(\epsilon'' + \epsilon)}, \quad (5.1a,b)$$

with the incident ray's angle  $\epsilon$  and the refracted ray's angle  $\epsilon''$ . According to the law of reflection

$$n \sin(\epsilon) = n'' \sin(\epsilon''). \quad (5.2)$$

The total reflection is

$$R = \frac{1}{2}(R_s + R_p) \quad (5.3)$$

and for  $\epsilon \rightarrow 0$

$$R = \left( \frac{n'' - n}{n'' + n} \right)^2. \quad (5.4)$$

This means that a fibre with the refractive index of  $n_{fibre} = 1.51$  will lose  $R_{ent} = 4.1 \%$  at its entrance and  $R_{ext} = 4.1 \%$  at its exit due to fresnel reflection if the ray's incident angle is  $0^\circ$  and the ray is entering from- and exiting into air ( $n_{air} = 1$ ). This leads to a total efficiency of  $\eta_{surf} = 92 \%$ <sup>1</sup> and barely changes over the necessary incident angles.<sup>2</sup>

The losses can be decreased significantly by using anti reflection (AR) coatings at the fibre entrance and exit.

Attenuation between the powers  $P_1$  and  $P_2$  of two different cross sections, separated by the distance  $L$ , is defined as [Fre96]

$$a(\lambda) = \frac{10 \cdot \log\left(\frac{P_1(\lambda)}{P_2(\lambda)}\right)}{L}. \quad (5.5)$$

Hence, the ratio between the output power  $P_2$  and the input power  $P_1$  at two different would be

$$\eta_{at}(\lambda) = \frac{P_2(\lambda)}{P_1(\lambda)} = 10^{-a(\lambda) \cdot L/10}. \quad (5.6)$$

According to established vendors<sup>3</sup>, common attenuation values in the relevant wavelength range are below  $a = 200 \text{ db/km}$ <sup>4</sup>. For an optical fibre with  $L = 2 \text{ m}$  length, this would lead to a minimum efficiency of  $\eta_{at} = 91.2 \%$ . Combined with the probable fresnel loss, the total efficiency would be around

$$\eta_{LP} = \eta_{surf} \cdot \eta_{at} = 83.8 \%.$$

### 5.2.3 Diffuser

Diffusers are a cheap variant to scatter light. They change the direction of incoming rays to a distribution of output ray directions. Diffusers with high scattering rates normally have a comparably low transmission. Established vendors<sup>3</sup> offer diffusers with nearly lambertian ray distribution and 30 % transmission. They also provide specimens with an intensity-over-angle-distribution with an approximate full width half maximum (FWHM) of  $\pm 2.2^\circ$  and 90 % transmission.

<sup>1</sup> $\eta_{surf}(\epsilon = 0^\circ) = (1 - R_{ent})(1 - R_{ext}) = 91.91 \%$

<sup>2</sup>Typical fibre aperture:  $NA = 0.22 \equiv \epsilon = 12.7^\circ$ . Even  $\eta_{surf}(\epsilon = 20^\circ) = 91.86 \%$

<sup>3</sup>thorlabs.com, edmundoptics.com, request date: 10.06.17

<sup>4</sup> $a_{max} < 200 \text{ db/km}$  for  $\lambda = (400 \dots 800) \text{ nm}$ , as shown in figure A.1 (Low-OH-curve)

If the optical system just consisted of an objective and a diffuser, it would scatter the slit's image on the substrate (FoV) and significantly decrease the system's spatial resolution.

## 5.2.4 Evaluation

Crit	W	Homogenization method					
		Int. sphere		Light pipe		Diffuser	
		G	P	G	P	G	P
OE	5	0	0	3	15	3	15
CP	4	1	4	6	24	2	8
GH	3	6	18	4	12	3	9
SR	3	5	15	5	15	1	3
C	2	1	2	3	6	6	12
		$\sum$ P:	39	$\sum$ P:	72	$\sum$ P:	47

Table 5.2: Evaluation Table: Homogenization Method

In table 5.2, a clear decision for the light pipe solution in form of an optical fibre is made. The additional mechanical decoupling between spectrograph and objective makes the construction significantly smaller. It enables the use of easily purchasable translation- and rotation stages, which are specially designed for optical applications.

## 5.3 Moving FoV

To fulfil requirement 10 from section 2.3, it is necessary to do a repositioning of the FoV on the substrate. In this section, several possibilities for this partial function are presented and analysed.

### 5.3.1 Relative Movement between Fibre Entrance and Lens

If the fibre entrance is moved for  $\Delta r_{yz}$  (y- and z direction from figure 2.2) on the lens's image plane, the FoV gets replaced by the same amount multiplied by the reproduction scale  $\beta'$  on the object plane:

$$\Delta r'_{yz} = \beta' \cdot \Delta r_{yz}. \quad (5.7)$$

To move the FoV within the required range of  $\Delta r'_y \geq 160 \text{ mm}$ , a relative movement of  $\Delta r_y = 43 \text{ mm}$ <sup>5</sup> would be necessary.

For a movement in x-direction, a relative movement in axial- and lateral direction to the optical axis would be necessary because the optical path is not parallel to the x-axis. The relationship between relative axial movement of the fibre entrance and the FoV's movement is not linear. It is described by the projection equation [Haf03]

$$\frac{n'}{a'} - \frac{n}{a} = \frac{n'}{f'} \quad (5.8)$$

with the distance  $a'(a)$  between the lens's knot point and image(object) and the refractive indices  $n = n' = 1$ . Because [Haf03]

$$\beta' = \frac{na'}{n'a}, \quad (5.9)$$

also the FoV's extent would depend on the object distance as it gets magnified by  $\beta'$ .

The equations 5.7, 5.8 and 5.9 are just valid for the paraxial regime and can only be used to estimate the FoV's position roughly. The substrate's extent of approximately  $160 \times 100 \text{ mm}^2$  implies a big object field far off from paraxial conditions. Aberrations like coma, astigmatism, field curvature and distortion would severely influence the FoV's axial-/lateral position and extent in comparison to paraxial conditions. A lens system that is optimized for big fields should be used to achieve appropriate projection conditions. However, measurements of different spots would be less comparable. Moreover, a mapped scan of the substrate surface would take more effort because the system would need to be refocussed for each spot that shall be measured.

### 5.3.2 Moving entire Objective

The optical components could stay in a fixed relative position to each other while the whole optical system would move. The FoV would be kept on the optical axis and constant in its extent, form and distance to the objective, which would make measurements from different spots more comparable.

---

<sup>5</sup>According to figure A.2,  $\beta' = -3.7$ , so  $\Delta r_y = \frac{\Delta r'_y}{\beta'} = 43 \text{ mm}$

The FoV's movement axes would need to be adjusted to be parallel to the substrate plane once. This would increase the constructional effort. The FoV could then be moved without having to be refocussed for each spot on the substrate plane. Its position on the substrate plane could also be relatively easily estimated by looking at the movement stages' coordinates.

### 5.3.3 Evaluation

Crit	W	Movement of FoV			
		Relative movement between lens and image field blind		Moving entire objective	
		G	P	G	P
CP	4	6	24	4	16
A	4	2	8	5	20
CM	3	2	6	6	18
		$\sum P:$	38	$\sum P:$	54

Table 5.3: Evaluation Table: Movement of FoV

A movement of the entire objective is chosen, despite the increased constructional effort. The system is easier to handle and delivers measuring results that are more comparable to each other.

### 5.3.4 Additional Possibility: Use of several FoV at once

As mentioned in Chapter 3, spatial information could be obtained by using *long-slit-spectroscopy*. Fibres could be arranged in slit and image field to measure spectra from several FoV at once. This could potentially reduce the substrate scanning time by a factor equal to the number of separate fibres used. As the number of applicable separate fibre exits is limited, this solution would not replace the ones from the previous chapter but complement them. However, the constructional effort and costs would increase. The spectrograph's CCD-sensor would have to be exchanged with a compatible 2D-array and a special fibre bundle would be necessary. Similar to the case of section 5.3.1, the optics should be dimensioned for a bigger object field to get similar projection conditions for the simultaneously measured different FoV on the substrate plane.

# Chapter 6

## Construction of an optomechanical System

### 6.1 Optics

#### 6.1.1 Fibre

The fibre will not just be used to homogenize the light and to decouple objective from spectrograph. Its core diameter will also work as the spectrograph's entrance slit. The fibre's aperture should be rather close to the spectrograph's but not smaller. The fibre's core diameter should be big enough to collect sufficient amounts of light but not too big to lose too much resolution.

A multimode fibre with 2 m length is used. Its core diameter of 550  $\mu\text{m}$  is similar to the slit width which was used to get the spectra in 4.4. With  $NA = 0.22$ , the fibre's half aperture angle is  $\theta_{fibre} = 12.7^\circ$  in comparison to the spectrograph's  $\theta_{spec} = 7.3^\circ$  (see requirement 2.3-3). No smaller apertures have been found for the elected core diameter.

#### 6.1.2 Lens

According to the fibre data and the geometrical limitations, an objective is developed. It will consist of one lens, which will also work as the system's aperture. Figure A.2 shows the system's paraxial design from to table 6.1. A lens with a focal length  $f' = 75 \text{ mm}$  is elected. To get a smaller FoV and less chromatic aberrations, the lens shall be achromatic. A ray fan and a spot diagram are simulated, as shown in figure A.3.

Parameter	Value	Comment
Image radius	0.275 mm	Fibre core radius
NA'	0.22	Fibre NA
Object distance	350 mm	Distance between window and back end of substrate + 10 mm (figure 2.2)
Aperture diameter	< 80 mm	Minimal distance between window bottom and substrate in z-direction (figure 2.2)
Spectral range	(400...800) nm	
Lens type	Achromatic	Chromatic correction and less aberrations

Table 6.1: Objective Requirements

The maximal extent of the FoV is assumed as

$$ext_{FoV} = \frac{2(hp_2 + r_{RMS})}{-\cos\alpha_p} + RD(\alpha_p) \quad (6.1)$$

with the object height  $hp_2$  and the "geometrical RMS r size"  $r_{RMS}$ .  $\alpha_p$  is the angle between the optical axis and the substrate plane's normal, as shown in figure 2.2. It should be as big as possible because the FoV's extent is proportional to  $-\frac{1}{\cos\alpha_p}$  with  $\alpha_p > 90^\circ$ . Therefore, the objective should be positioned as low as possible next to the window, which corresponds to a distance of the objective's half aperture to the window's lower end.

$$\alpha_p = 90^\circ + \arcsin\left(\frac{h_z - h_1}{e'_1}\right) \quad (6.2)$$

with  $e_1$  as the object distance,  $h_z$  as the substrate height and  $h_1$  as the aperture radius. Under the given conditions,  $\alpha_p = 99.5^\circ$ <sup>1</sup> and the maximum extent  $ext_{FoV} = 15.5 \text{ mm} + RD(\alpha_p)$ .<sup>2</sup>  $RD(\alpha_p)$  is the additional extent that is caused by ray divergence before- and after the focal point.

The FoV varies slightly with the wavelength. While  $hp_2$  does not change significantly,  $r_{RMS}(400 \text{ nm}) = 0.51 \text{ mm}$  and  $r_{RMS}(800 \text{ nm}) = 0.56 \text{ mm}$  increase the FoV up to  $ext_{FoV}(800 \text{ nm}) = 18.2 \text{ mm} + RD(\alpha_p)$ .

Figure 6.1 shows an attempt to estimate the FoV with a reconstruction of the ray fan from figure A.3 within the also reconstructed vacuum chamber. The estimated FoV has a length of  $l_{FoV} = 17 \text{ mm}$  and a width of  $b_{FoV} = 3 \text{ mm}$ .

<sup>1</sup> $e_1 = 350 \text{ mm}$  and  $h_1 = 22 \text{ mm}$  from figure A.2.  $h_z = 80 \text{ mm}$  from figure 2.2

<sup>2</sup> $hp_2 = 1 \text{ mm}$  from figure A.2 and  $r_{RMS} = 0.28 \text{ mm}$  from figure A.3

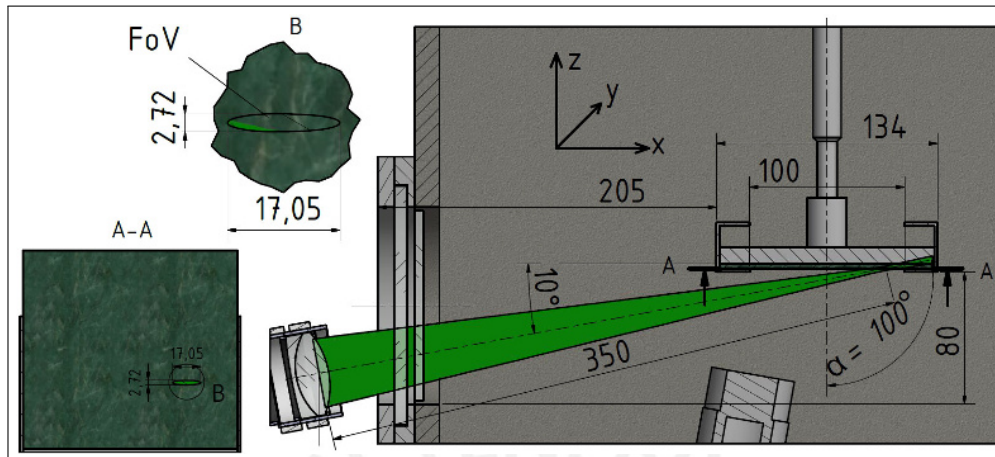


Figure 6.1: Estimation of the FoV by reconstructing ray fan from figure A.3 and putting it into the final construction.

## 6.2 Mechanics

### 6.2.1 Rotational-/translational Movements

The substrate shall be scannable by moving the FoV over it. The FoV's track should be as predictable and intuitive as possible. Therefore, translational movement is preferred. It allows movement along an axis without parasitic movement to other directions. The covered distance can be read out directly without further calculations. If translational movement is not possible, a circular track shall be aspired.

#### **x-direction**

Except the window, there is no obstacle for the objective and the optical path for a translational movement in x-direction (figure 6.1).

#### **y-direction**

Figure 6.2 shows that the window is too small to make a scan of the entire substrate possible by a translational movement. The aperture would be shadowed or completely blocked by the window's frame if moved near to the extremes of the substrate in y-direction. Therefore, the FoV shall be slewed around an axis perpendicular to the substrate plane to enable a movement on the entire substrate in y-direction.



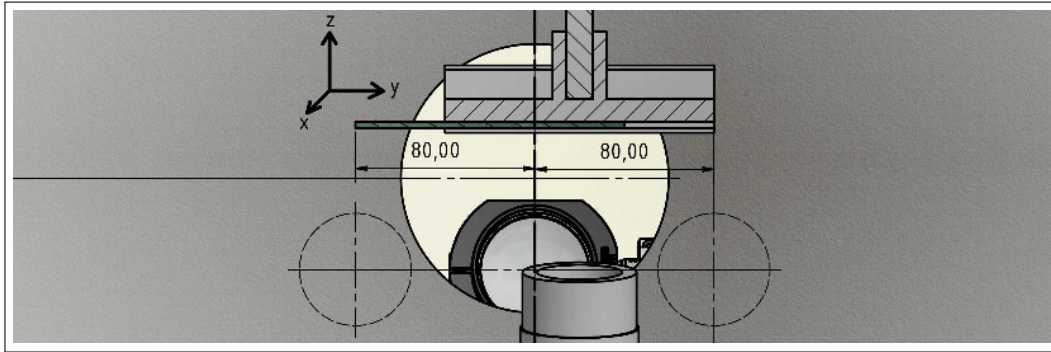


Figure 6.2: Objective behind window from substrate's perspective inside the reconstructed chamber. To cover the magnetrons' effective deposition field, the substrate has to outreach the substrate holder. The dashed circles represent the objective's position which would be necessary to scan the full substrate(-holder) in y-direction with a translational movement.

### **z-direction**

To adapt to different substrate heights, a translational movement in z-direction would be possible, as can be seen in figure 6.1. However, to measure the plasma, the space between the magnetrons and the substrate must be observable. Because of the window frame, this is just possible by slewing/rotating the objective.

Substrate- and plasma observation could be separated by introducing an additional DoF, allowing translation for substrate- and rotation for plasma observation. The benefits would be that the FoV would keep its relative distance in x-direction on the substrate and would not need to be refocussed while adapting its height to the substrate. This is not seen as worth the increase of costs and constructional effort as the substrate height does not get changed very frequently during the sputtering process.

## **6.2.2 Mechanical Principle and Construction**

Figure 6.3 shows the technical principle of the final construction. The substrate plane is spanned by the vectors  $\mathbf{x}_p$  and  $\mathbf{y}_p$ .  $\mathbf{x}_p$  lies in a plane which is spanned between  $\mathbf{e}_t$  and  $\mathbf{e}_r$ . The substrate plane's height is adjustable by a movement along  $\mathbf{z}_p$ . The object distance  $\mathbf{a}$  is constant.

To move the FoV onto the substrate plane or down into the plasma,  $\mathbf{e}_a$  can be slewed around  $\mathbf{e}_g$  by using the goniometer.  $\mathbf{e}_g$  should be roughly parallel to the substrate plane.

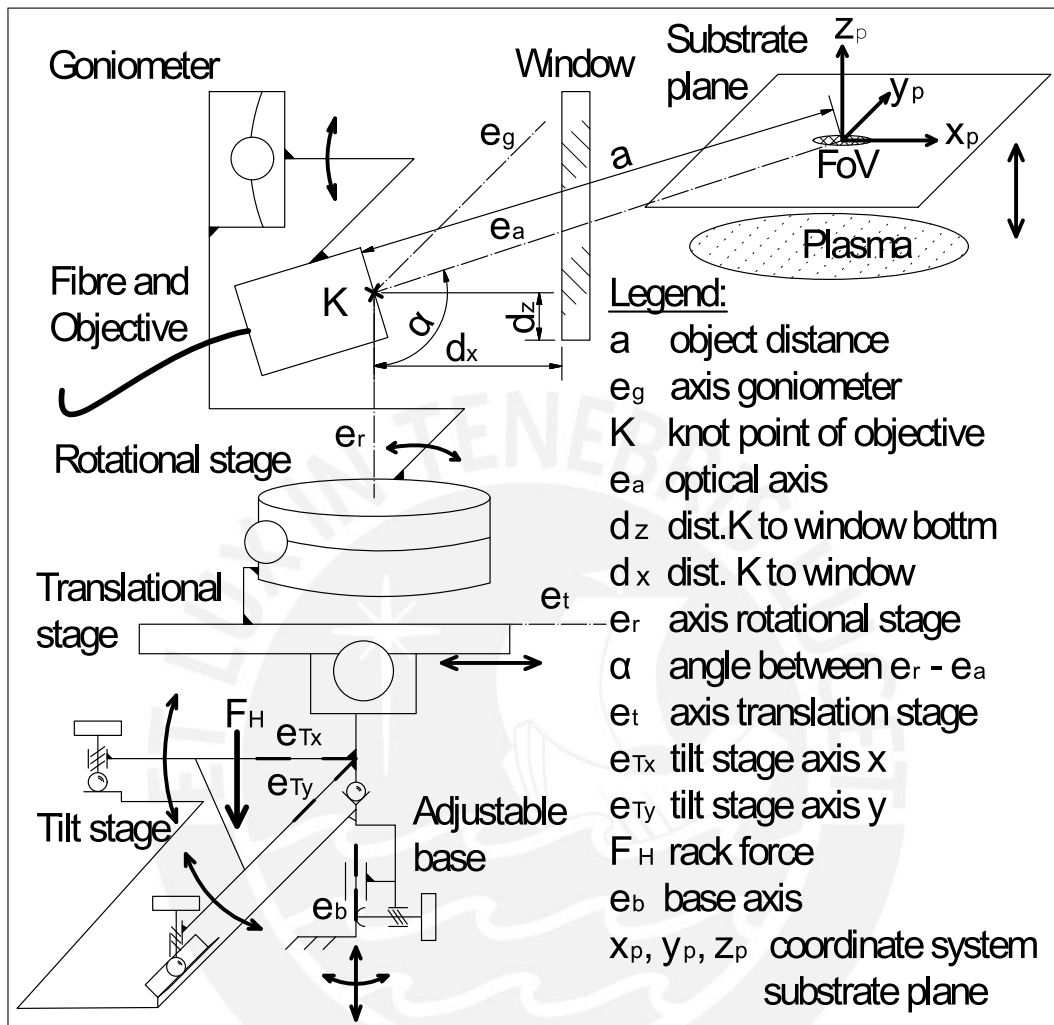


Figure 6.3: Technical principle of final construction.

The knot point  $K$  lies approximately on the intersection between  $e_a$  and the outer lens surface of the objective.  $e_g$  should be approximately coincident with  $K$  to keep  $d_z$  roughly constant. If  $d_z$  decreases, the aperture will get shadowed partly by the window's bottom end. If  $d_z$  increases,  $\alpha$  decreases relatively if the same spot is observed, which leads to a bigger FoV, as shown in section 6.1.2. These effects should be avoided.

The translational stage is movable along  $e_t$ . It shall be used to move the FoV along  $x_p$ .  $e_t$  and  $x_p$  have to be parallel to keep the FoV focussed within the substrate plane while it is moved. Appendix A.1.3 describes a possible translation error that occurs if  $e_t$  does not lie in the substrate plane.

$\mathbf{d}_x$  varies with the objective's position in  $\mathbf{e}_t$ -direction. It reaches its minimal value  $\mathbf{d}_{x\min}$  when the substrate's back end is observed.  $\mathbf{d}_{x\min}$  should be as small as possible to keep  $\mathbf{a}$  and  $\alpha$ , and therefore the FoV, small.

To move the FoV in  $\mathbf{y}_p$  direction, the rotational stage shall be used to slew  $\mathbf{e}_a$  around  $\mathbf{e}_r$ . To keep the FoV within the substrate plane,  $\mathbf{e}_r$  needs to be perpendicular to  $\mathbf{x}_p$  and  $\mathbf{y}_p$ . This implies also that  $\mathbf{e}_t$  has to be perpendicular to  $\mathbf{e}_r$ . If  $\mathbf{e}_a$  is slewed around  $\mathbf{e}_r$  by the angle  $\Delta\phi_y$ ,

$$\Delta y_p = a \cdot \sin(\alpha) \cdot \tan(\Delta\phi_y), \quad (6.3)$$

but there is also a parasite movement

$$\Delta x_{ppar} = a \cdot \sin(\alpha) \cdot (\cos(\Delta\phi) - 1) \quad (6.4)$$

in  $\mathbf{x}_p$ -direction because the FoV moves within a circular path. This must be considered during substrate scans.

To make  $\mathbf{e}_r$  perpendicular- and  $\mathbf{e}_t$  parallel to the substrate plane, the tilt stage shall be used. With two screws, the base shall be tiltable around  $\mathbf{e}_{Tx}$  and  $\mathbf{e}_{Ty}$ , which shall be perpendicular to each other.

The holding force  $\mathbf{F}_H$ , produced by a screw or a spring, shall keep the construction fixed to the base.

To accurately position the assembly relatively to the window, the base is rotatable and adjustable in its height around- and along axis  $\mathbf{e}_b$ .

$$\begin{array}{cccccc} \uparrow & & \uparrow & & \uparrow & & \uparrow & & \uparrow \\ e_t \parallel x_p; & e_r \perp x_p; & e_r \perp y_p; & e_g \perp e_r; & e_{Tx} \perp e_{Ty} & & & & \end{array} \quad (6.5)$$

The plans of the final construction can be found in appendix A.2. Figure 6.4 shows photographs of the final assembled construction.

The goniometer has a range of  $\pm 10^\circ$  and a resolution of  $5'$ .<sup>3</sup> The translation stage has a range of  $\pm 50 \text{ mm}$  and  $1 \text{ mm}$  increments.<sup>3</sup> The rotational stage is rotatable for  $360^\circ$  and has  $10'$  increments.<sup>3</sup> With an object distance of  $a = 350 \text{ mm}$  and  $\alpha = 100^\circ$  each increment should mean a movement of  $\Delta y(10') = 1 \text{ mm}$  in y-direction, according to equation 6.3.

The tilt stage can be adjusted within a range of  $\pm 2.5^\circ$  around  $\mathbf{e}_{Tx}$  and  $\mathbf{e}_{Ty}$ .

---

<sup>3</sup>edmundoptics.com, request date: 10.06.17

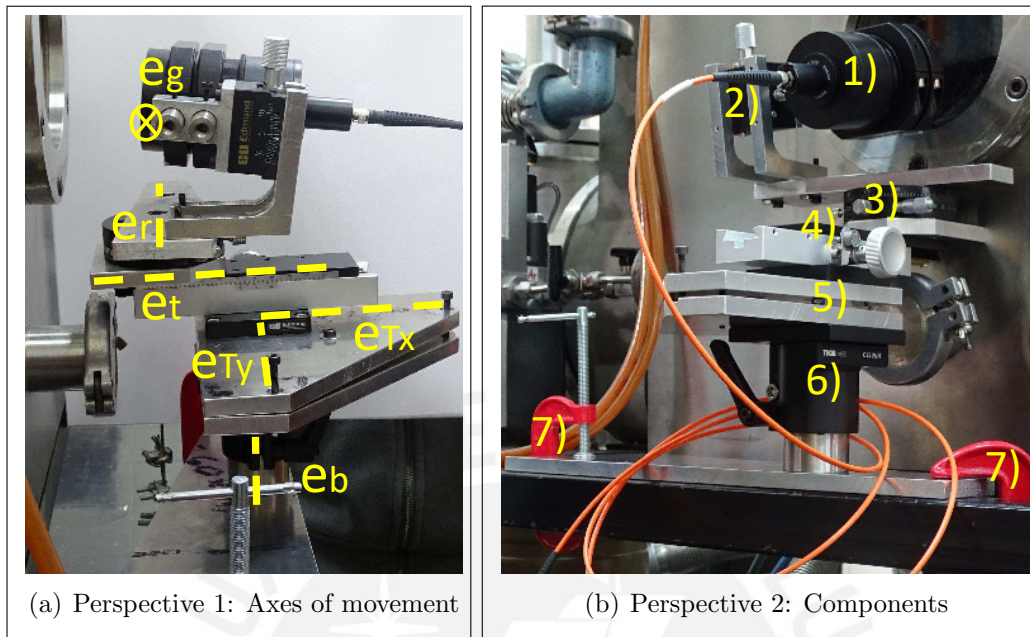


Figure 6.4: Assembled construction: (a) Perspective from left side. Movement axes from figure 6.3 are shown. (b) Perspective from back right side. 1) Objective and fibre, 2) Goniometer, 3) Rotation stage, 4) Translation stage, 5) Tilt stage, 6) Height adjustable/rotatable base, 7) Clamps.

# Chapter 7

## Analysis of the System

### 7.1 Setup

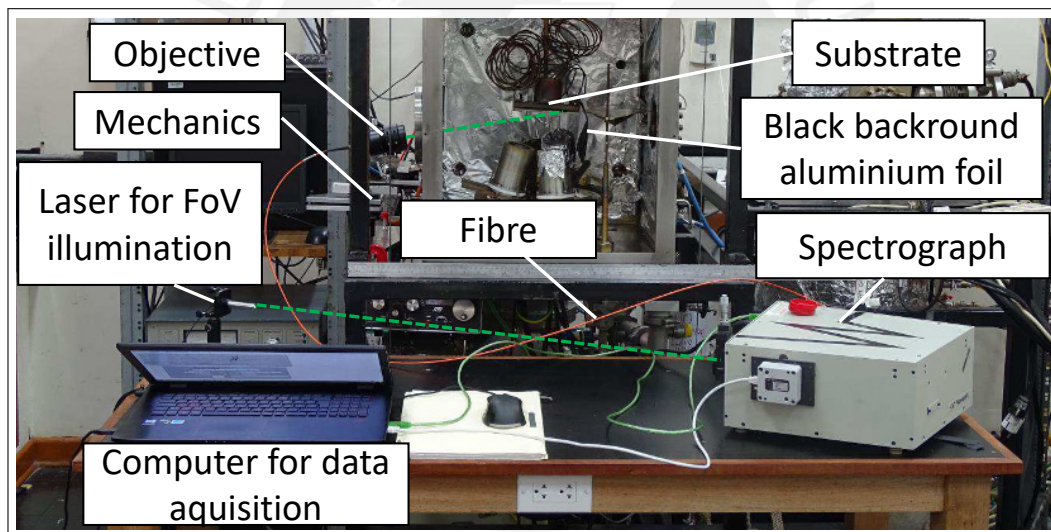


Figure 7.1: Setup of main analysis. The dashed green lines represent paths of light from the laser source into the spectrograph and from substrate and plasma into the objective (or the other way around).

Figure 7.1 shows the all necessary components for the spectroscopy of Tb emission. Their purpose has already been described in section 4.1. However, some components have changed:

- The light source was changed from a simple  $650\text{ nm}$  laser pointer to a  $4.5\text{ mW}$  and  $532\text{ nm}$  laser diode. The FoV shall be smallest for the Tb emission. Its main peak lies at about  $540\text{ nm}$ , as can be seen in figures

1.5b and 4.5. The light to get the FoV focussed should be near to this peak's wavelength to avoid focal shift due to chromatic aberrations.

- The objective lens was changed from a biconvex singlet ( $f' \approx 115 \text{ mm}$ ) to an achromatic lens ( $f' = 75 \text{ mm}$ ). Spherical- and chromatic aberrations are reduced for FoV projection.
- The objective can now be moved reproducibly in three DoF.
- The "black body" from figure 4.2b is now a piece of matt black aluminium foil.
- An optical fibre disconnects spectrograph and objective spatially and homogenizes incoming light.
- The CCD-sensor is not mounted correctly but is shifted on the optical axis. The entrance slit does not lie in the object plane. The fibre exit can be positioned within the real object plane, which leads to higher signal resolution and intensities.

## 7.2 Field of View (FoV)

The laser source is used to illuminate the FoV through fibre and objective. In the objective's illuminated aperture, an outer ring and an inner circle can be seen (figure 7.2a). The illuminated field on the substrate consists of a bright core and two tails at both sides of the core. These tails enlarge the illuminated field to more than double its core size. If the FoV is represented by the whole illuminated field, a huge loss in spatial resolution would result.

It must be found out if these tails are relevant for spectral analysis, or if it is possible to just let the bright core count as FoV. The system is tested with different aperture diameters  $D$ .<sup>1</sup>

As seen in figure 7.2b, the tails' extents decrease when  $D$  is reduced. At  $D = 40 \text{ mm}$ , the right tail has already lost half of its extent and even more brilliance. At  $D = 20 \text{ mm}$ , just a slight shining left of the core is visible.

Figure 7.3b shows that  $D = 40 \text{ mm}$  does not decrease the captured spectral intensity at all, even though the luminous outer ring from figure 7.2a is already completely shadowed. Even with  $D = 20 \text{ mm}$ , (80...90) % of the intensity still hits the CCD.

Hence, the observed tails do not have a big influence on the measurements. The bright core is declared as FoV for the following analysis.

---

<sup>1</sup> $D = 50 \text{ mm}$  (full aperture),  $D = 40 \text{ mm}$  and  $D = 20 \text{ mm}$

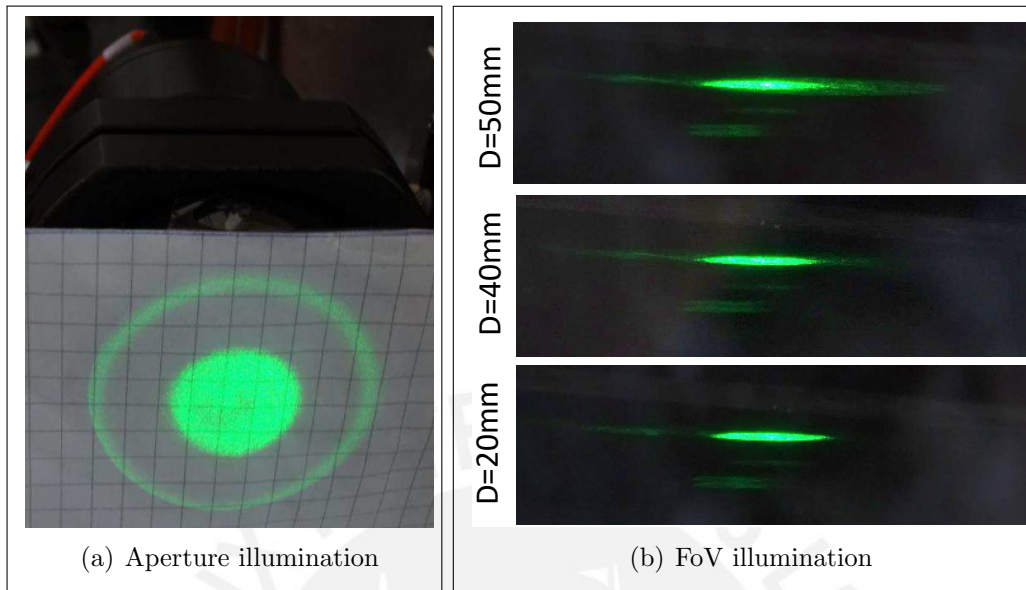


Figure 7.2: (a) Illumination of aperture near objective lens projected on white paper. The illumination profile consists of an outer ring ( $D \approx 45 \text{ mm}$ ) and an inner circle ( $D \approx 20 \text{ mm}$ ). (b) Projection of FoV on substrate with different aperture diameters. FoV consists of a bright core and tails left and right of it. A decreasing aperture diameter leads to a decrease of the tails' extent.

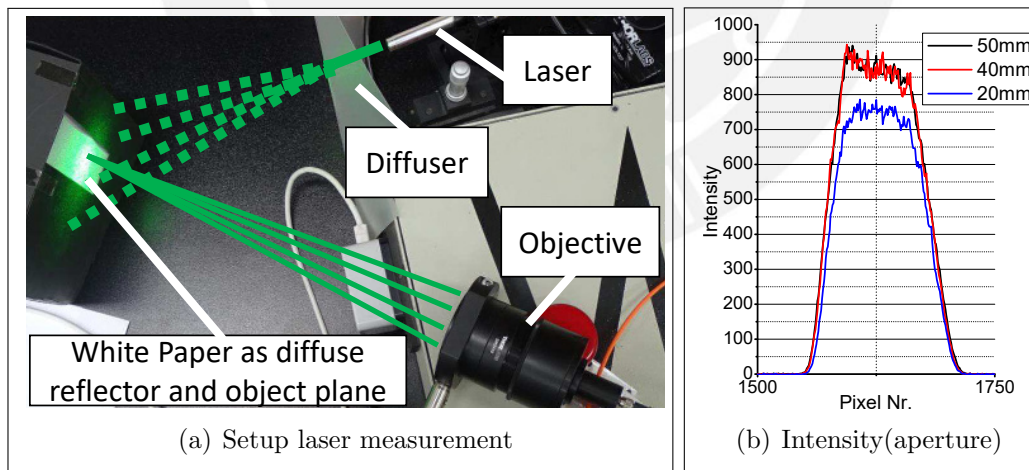


Figure 7.3: (a) Setup to measure laser spectrum. The laser ray is strayed by a diffuser onto a white paper surface which reflects the light also diffusely. The objective is focussed on the paper and channels the reflected light into the spectrograph. (b) Measured intensities with different aperture diameters. The curves for  $D = 50 \text{ mm}$  and  $D = 40 \text{ mm}$  lie directly on top of each other.

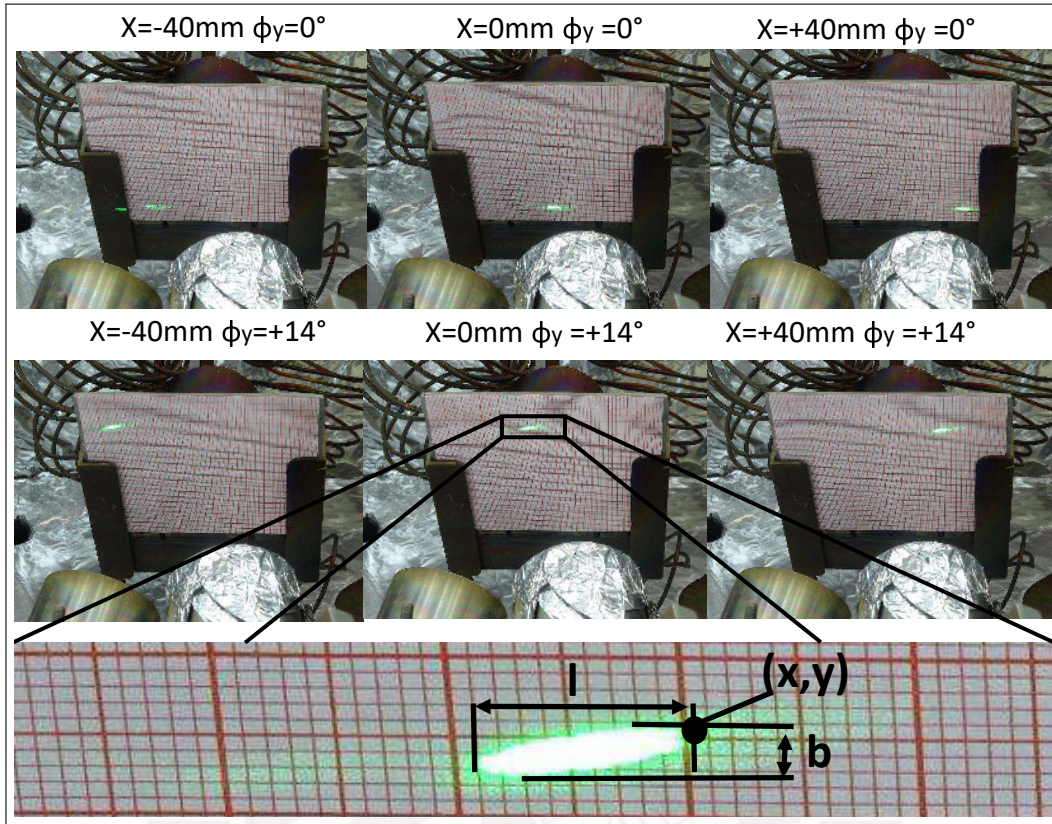


Figure 7.4: FoV is moved to different spots by moving the translation stage by "X" and the rotation stage by  $\phi_y$ . Position  $(x, y)$  on substrate, length  $l$  and width  $b$  of FoV is measured for each probe.

To measure the FoV's extent and the repeatability of its movement, scale paper is spanned onto the substrate holder. The FoV is moved to six different positions on the scale paper. Each position is approached three times. The procedure is done for two different substrate heights  $H_z = (3.0, 4.5) \text{ cm}$ , read from ruler on top of chamber. The probes are created in form of a photography of the substrate from a constant perspective. The resolution  $Res = 1 \text{ mm}$  of the measurements is limited by the increments of the scale paper and the unclear definition of the bright core's borders.

As seen in table A.1, the FoV's maximum extent  $l_{max} = 12 \text{ mm}$  was measured at  $H_z = 3 \text{ cm}$  substrate height.<sup>2</sup> It tends to decrease with an increasing substrate height as the angle  $\alpha_p$  in equation 6.1 increases.

<sup>2</sup> $H_z$  read from ruler on top of chamber.  $H_z = 3 \text{ cm} \hat{=} h_z = 75 \text{ mm}$



The coordinates of the probes, when repeatedly positioned onto the same spot, vary maximally between two values. This means a repeatability of  $Rep_{mov} \leq 1 \text{ mm}$  as a lower value cannot be proven by the applied measuring method.

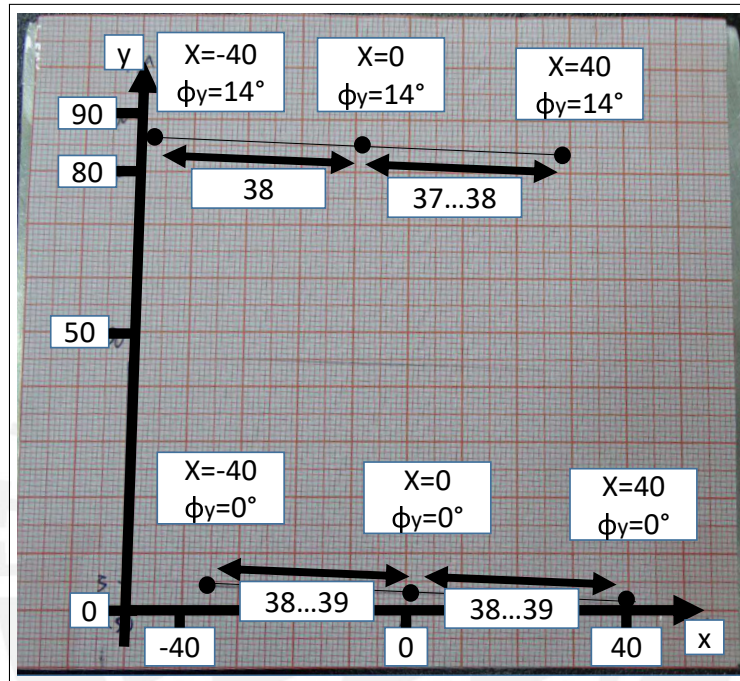


Figure 7.5: Photography of scale paper on substrate holder with added marks for probe positions and coordinate system. Distance values taken from table A.1

The measurement shows that the mean value of  $\frac{\Delta x}{\Delta X} = \frac{38}{40} = 95 \%$ . According to figure A.6, this means a relative inclination between substrate and stage axis of  $\gamma \approx +(0.5...1)^\circ$ .

With  $Rep_{mov} \leq 1 \text{ mm}$ , the results for repeatability are sufficiently good. The FoV's extent is smaller as expected.<sup>3</sup>

The sensitivity of the  $\frac{\Delta x}{\Delta X}$ -ratio towards slight inclinations (figure A.6) shows that at the actual system's condition, scans with high mapping accuracy are not possible. A more stable construction of the substrate holder would be necessary to permanently adjust the tilt stage to the movement stages' axes in order to make mapped scans possible.

<sup>3</sup> $l_{max} = 12 \text{ mm} < 17 \text{ mm}$  in figure 6.1

However, already possible is a movement of the illuminated FoV to relevant positions, e.g. probe objects on the substrate holder, and noting the coordinates from the translation-/rotation stage and goniometer before the deposition process. These coordinates can then be checked repeatedly with high spatial accuracy ( $< 1 \text{ mm}$ ) during the process.

### 7.3 Resolution and Intensity at different axial Fibre Positions

With the given fibre core diameter of  $D_c = 0.55 \text{ mm}$  and the reciprocal linear dispersion  $P = 3.2 \frac{\text{nm}}{\text{mm}}$ , the system's resolution should be around  $Res_{sys} = D_c \cdot P = 1.76 \text{ nm}$ . To measure the system's resolution and (relative) étendue, the setup of figure 7.3a is used. The fibre adapter of the spectrograph can be moved and fixed along the optical axis of the entrance slit. Two optimal axial positions have been found for the fibre exit: One for maximal étendue and one for maximal resolution. Both are measured with various slit widths.

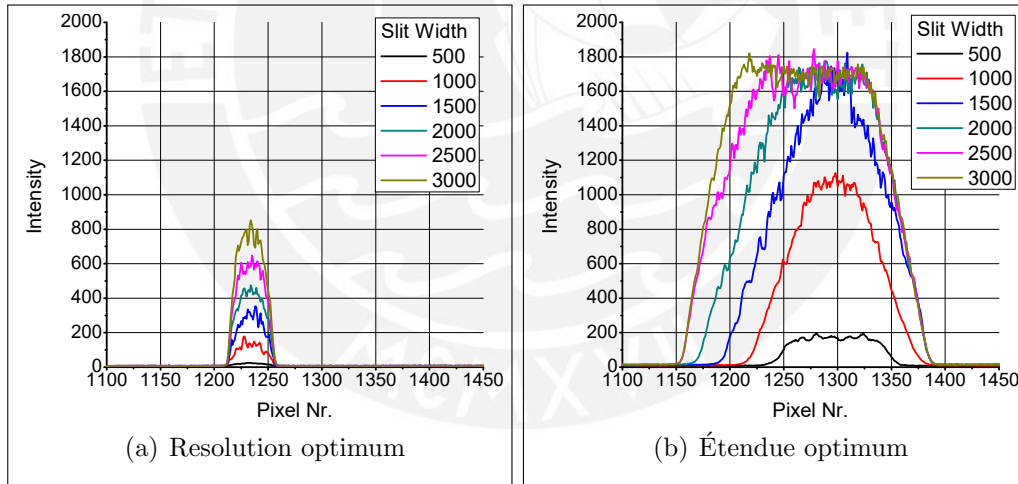


Figure 7.6: Spectroscopies of  $532 \text{ nm}$  laser light source taken with (a) fibre axial position for max. resolution. (b) fibre axial position for max. étendue.

Figure 7.6a shows the case of maximal resolution. The peaks' FWHM is  $1.5 \text{ nm}$ .<sup>4</sup> An increasing slit width only leads to a higher peak intensity. The peaks themselves keep their narrowness. Thus, the entrance slit works as the setup's aperture and the fibre exit is located in the detector's projection plane.

<sup>4</sup> $34 \text{ pixels}$  multiplied with  $\Delta\lambda_{pix} = 0.0448 \text{ nm}$  from equation 2.3

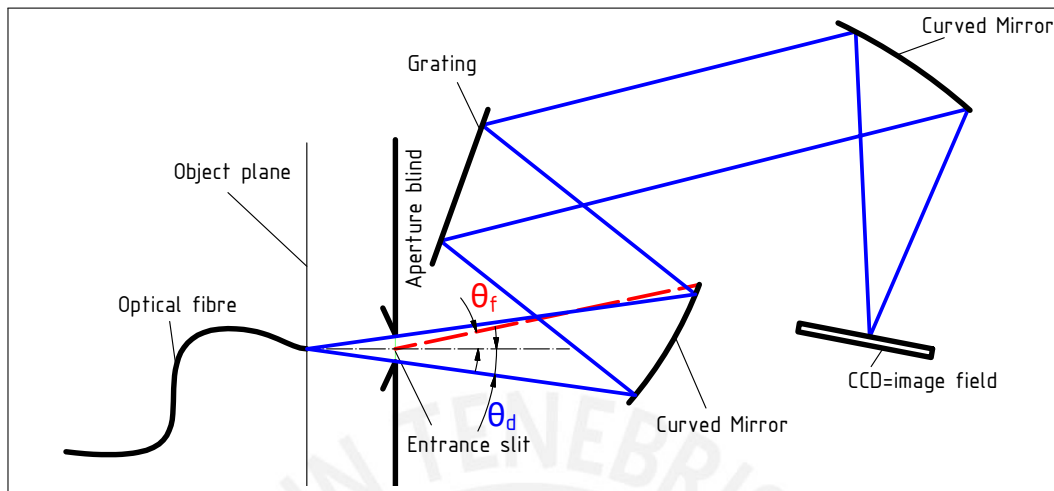


Figure 7.7: Fibre exit put into object plane to refocus onto shifted CCD-detector plane. Due to the larger distance to the mirror, the aperture  $\theta_d$  will always be smaller than  $\theta_f$  that would be possible if the detector would be in the entrance slit's image plane.

Figure 7.6b shows the curves for the axial optimal étendue position. It is closer to the slit than the position for optimal resolution. The maximal intensity is approximately two times higher than in figure 7.6a. The peaks' FWHM is not just larger than the one on maximal resolution position but also varies from 4.3 nm to 8.2 nm with increasing slit widths.<sup>5</sup>

As shown in section 2.2.2, the spectrograph is defocussed and does not work under optimal conditions. It is expected to have a similar resolution, as shown in figure 7.6a, and an equal- to higher étendue as available for the probe in figure 7.6b if the CCD is brought into the intended image plane.

<sup>5</sup>(96...183) pixels

## 7.4 Tb- and Plasma Signal

A test measurement of the Tb deposition process with the final construction is made. The fibre's axial position is on the étendue optimum, as explained in section 7.3. The signals are plotted dark signal corrected and 10x averaged by the program of the CCD. No further processing was made. The Tb spectrum is extracted, as described in section 4.2.

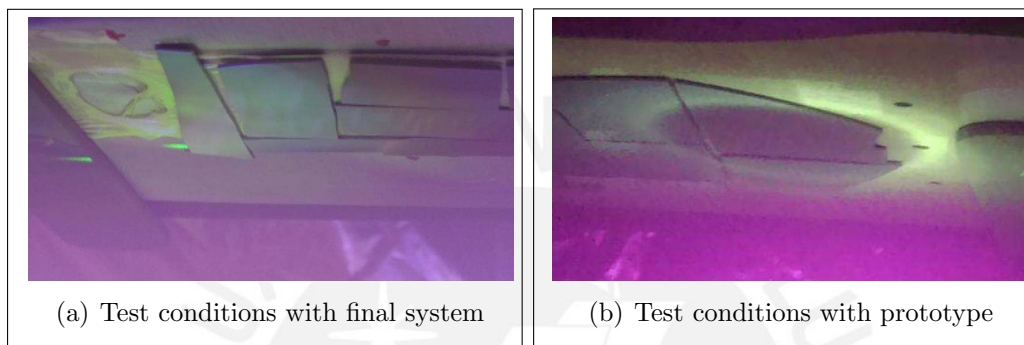


Figure 7.8: Process conditions while testing final- and prototype system. There was a generally higher Tb emission intensity during the test process of the prototype system (b).

The spectra of the final construction and the prototype from chapter 4 are compared. For both measurements, the spots with the highest Tb intensity on the substrate were elected to be analysed. However, the measuring conditions are different, as shown in figure 7.8 and table A.2. The prototype-measured process was a SiN:Tb deposition. The process, measured by the final system was an AlN:Tb deposition. In general, the emission intensity was higher during the prototype's measurement.

Figure 7.9c shows that the black Tb curve was extracted with a higher intensity by the final system despite the lower substrate emission intensity and even though a lower integration time was used for the measurement.

An explanation for this could be the defocussed state of the spectrograph, as shown in figure 2.3. The peaks smear over the detector plane and lose intensity on their actual location. Moreover, the defocus makes the object field no longer limited by the entrance slit which actually should work as a field blind. The effective object field is bigger than normally. Hence, the effective FoV on the substrate/plasma also increases to probably less intensively emitting regions. The FoV's average luminance most likely drops and so does the captured intensity.

The extraction of the Tb spectrum also seems to have worked more cleanly on the black curve. The extracted red curve of the prototype system has more disturbances where big plasma peaks have been subtracted from each other.

By slewing the FoV from substrate to plasma, the illumination distribution on the object field might have changed. This change would also be visible on the detector. The signal separation would then have more errors like the red curve in figure 7.9c. The fibre exit slit stays on a fixed position in the object field and has a constant spatial and directional flux distribution. Thus, less extraction errors occur. An error in the grating's repeatability seems to be less crucial than assumed in section 4.3.

The plasma curves in figure 7.10b show that the peak resolution is higher in the final system. This corresponds to the smaller effective object field as its extent is limited by the fibre exit's core diameter, as can be seen in figure 7.7.

Also, the spectral distributions differ. The peak at approximately  $\lambda = 650 \text{ nm}$  in the prototype's black curve is relatively high in comparison to the one of the red curve. The origin of this difference is assumed in the differing process conditions. The plasma of the prototype measurement in figure 7.8b appears to be more reddish than the plasma colour of figure 7.8a, which corresponds to the made assumption.

Another difference can be found below  $\lambda = 400 \text{ nm}$ . While the prototype still measures emission, the final system's curve is flat zero in this range. This behaviour is most likely caused by the "low-OH" fibre's optical efficiency which decreases significantly in this sector.<sup>6</sup>

Before its assembly, the final system was expected to have a lower throughput than the prototype because of the additional fibre losses. Due to its refocussing ability, it was possible to gain higher peak intensities and higher resolution at the same time. Nevertheless, the spectrograph still does not work in its optimal performance. Before the system's calibration, the CCD should be brought back into the entrance slit's projection plane.

---

<sup>6</sup> $L = 2 \text{ m}$ ,  $a = 5 \frac{db}{m}$  at  $\lambda \approx 320 \text{ nm}$  (figure A.1). According to equation 5.6,  $\eta_{at} \approx 10 \%$

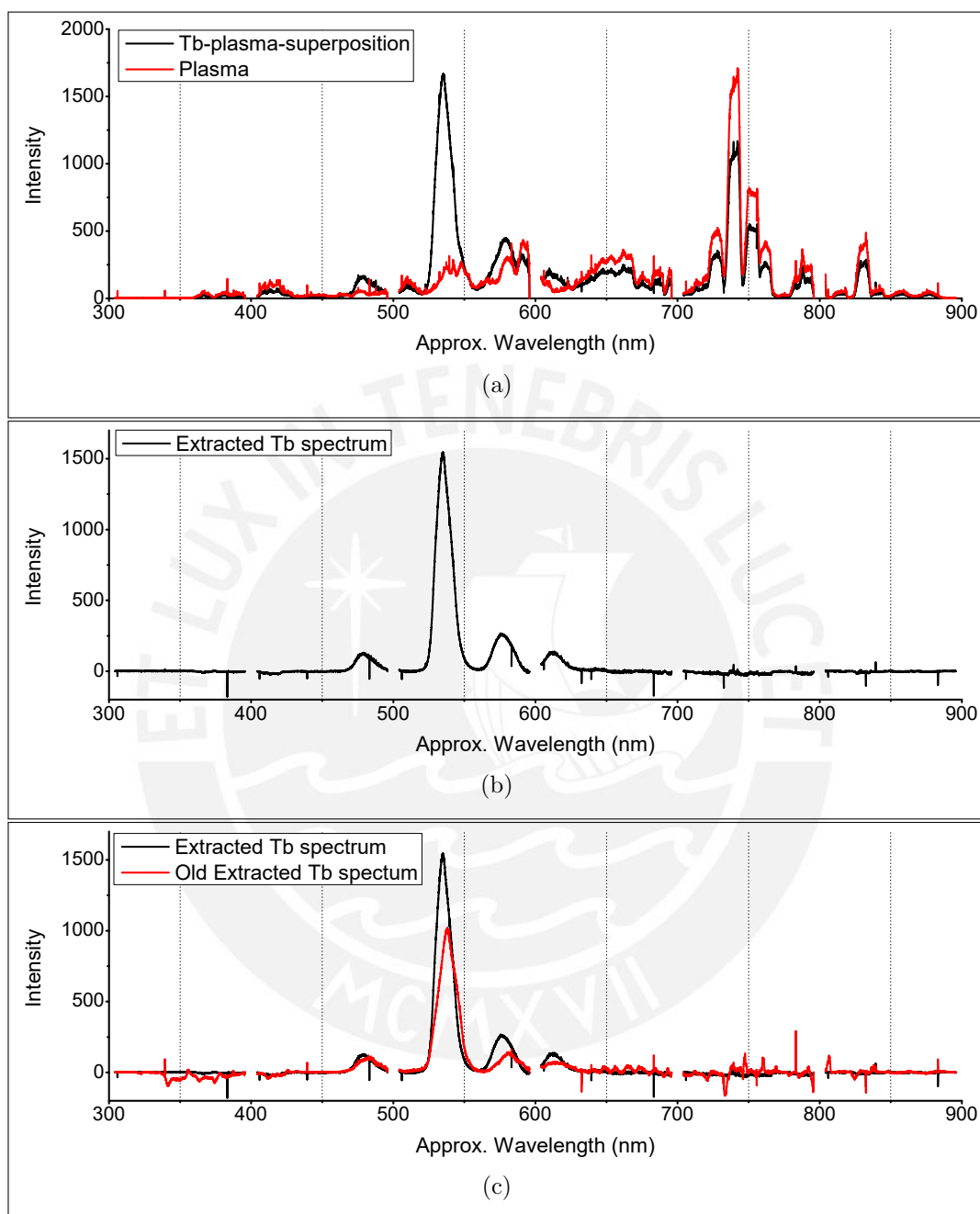


Figure 7.9: (a) Spectrum captured from substrate surface (black) and spectrum from plasma only (red). (b) Extracted Tb spectrum. (c) Comparison between Tb extraction with prototype (red) from section 4.2 and final construction (black).

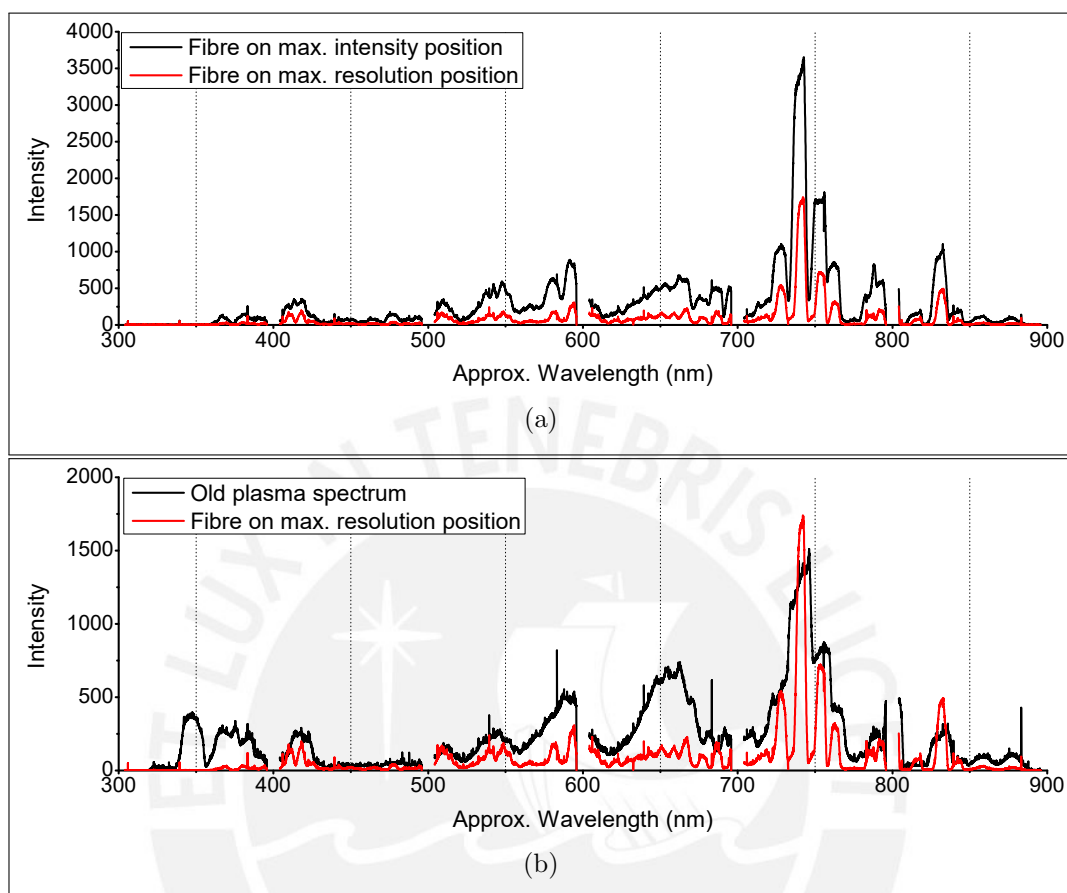


Figure 7.10: (a) Plasma spectra taken with fibre exit on max. intensity position (black) max. resolution position (red). (b) Comparison of plasma spectra between final construction and prototype system from section 4.2.

# Chapter 8

## Summary and Outlook

### 8.1 Summary

Chapter 1 begins with a definition of objective and motivation of the thesis, followed by a brief introduction into the sputtering process and in-situ emission spectra of sputtered Tb doped films. Furthermore, Optical Emission Spectroscopy (OES) is explained as well as the principles of étendue and the Lagrange Invariant.

Chapter 2 first introduces frame conditions like the utilised chamber and spectrograph. It ends with a specification of requirements the construction needs to comply with.

Chapter 3 introduces the state of the art. An investigation of existing solutions for similar problems is made.

In chapter 4, probes with a first prototype system are made to detect possibilities and problems for the final construction.

Chapter 5 splits the constructional problem into distinguishable parts. Different solutions for these partial problems are discussed, compared and elected to be adopted for the final principle.

In chapter 6, the optical system is dimensioned and constructed. Furthermore, movement types for the mechanical system's three degrees of freedom (DoF) are chosen and a final mechanical principle is introduced. Geometrical dependencies are determined. Partly discussed errors and the final construction's drawings can be found in the appendix.



Chapter 7 analyses the final construction. The Field of View (FoV) gets measured in its extent, its repositioning accuracy and its conformity to the mechanical system's movement. Afterwards, two optimal axial fibre exit positions are compared in terms of étendue and resolution. The two optimal axial positions are assumed to exist because the spectrograph is defocussed. At last, the final construction and the prototype are compared in their abilities to capture spectra from substrate and plasma.

## 8.2 Outlook

Due to utilization and positioning of the fibre, the system's ability to capture spectra has improved significantly in comparison to the prototype without fibre. However, sections 2.2.2 and 7.3 show that the system does not work in its optimal performance. Before the system gets calibrated, the detector plane should be brought to the entrance slit's image plane to get the best intensity/resolution ratio out of the spectrograph. The (still utilised) "micrometer adjustable slit" is not compatible with the fibre adapter and has to be replaced with a "fixed slit holder".<sup>1</sup> The CCD on the lateral port must be remounted with a greater distance<sup>2</sup> to the Spectrograph's wall or has to replace the exit slit at the axial port in order to be in the entrance slit's projection plane.

However, the entrance slit is still calibrated to the one at the axial port. The device at its current state can still be used as a monochromator. A dismantling of the slit would mean the destruction of this calibration. If a use of the device as a monochromator is no longer demanded, the replacement can be done and the spectrograph is ready to be calibrated.

A Program that combines the grating's movement with data gathering and processing would be useful to make the spectroscopy process more efficient. Especially if the substrate shall be systematically scanned, saving time is important as the emission conditions on the substrate surface can change within minutes. If just one spot is relevant, the program could observe the spot over larger amounts of time without the user's presence.

A further step could be the mechanical automation of the substrate scanning process. This would increase the scanning rate even more.

---

<sup>1</sup>newport.com, part nr.: 74001, (77357 and 77670), 77294. Request date: 11.06.17

<sup>2</sup>40 mm instead of 10 mm [New15]

As mentioned in section 7.2, a systematic substrate scan with high mapping accuracy is not possible yet. Before mechanical automation, a substrate holder that is able to fix the substrate in a reproducible position and orientation should be implemented. The tilt stage could then be effectively adjusted to the substrate holder.

Appendix A.1.3 includes an analysis of consequences of an orthogonality error  $\gamma_y$  of the rotational stage's axis  $\mathbf{e}_r$  to the substrate plane  $\mathbf{x}_p \times \mathbf{y}_p$  for the ratio between the translational stage's and the FoV's movement  $\frac{\Delta x}{\Delta X}(\gamma_y)$ . Additionally, an analysis regarding error  $\gamma_{x,y}$ , should be done for the ratio between objective rotation around  $\mathbf{e}_r$  and the FoV's movement  $\frac{\Delta y}{\Delta \phi_y}(\gamma_{x,y})$ , if scanning with high mapping accuracy is necessary.

The benefits of implementing mechanical automation must be weighed up against the high constructional effort which is combined with it.

Another method of significantly reducing the scanning time could be the use of several FoV at once, as discussed in section 5.3.4.

A relatively easy way to increase the captured emission intensity is the utilization of AR coatings on chamber window and protecting glass. The current, uncoated window and glass reflect  $R = 4 \%$  of incoming the light at each surface.<sup>3</sup> This means a total loss of 15 %.<sup>4</sup> AR coatings can reduce the surfaces' reflectance to about 0.3%, depending on the wavelength.<sup>5</sup> The windows' fresnel loss could be reduced to 1 %.<sup>6</sup>

Furthermore, the chamber window is already polluted and scratched, leading to additional absorption and scattering effects and making a window exchange even more worthwhile.

---

<sup>3</sup>According to equation 5.4 with an assumed refractive index  $n_{glass} = 1.5$

<sup>4</sup>Fresnel loss through four uncoated surfaces:  $1 - (1 - 0.04)^4 = 15 \%$

<sup>5</sup>See figure A.4

<sup>6</sup>Fresnel loss through four AR coated surfaces:  $1 - (1 - 0.003)^4 = 1 \%$

# Appendix A

## Appendix

### A.1 Supplements to Chapters

#### A.1.1 To Section 6.1.1

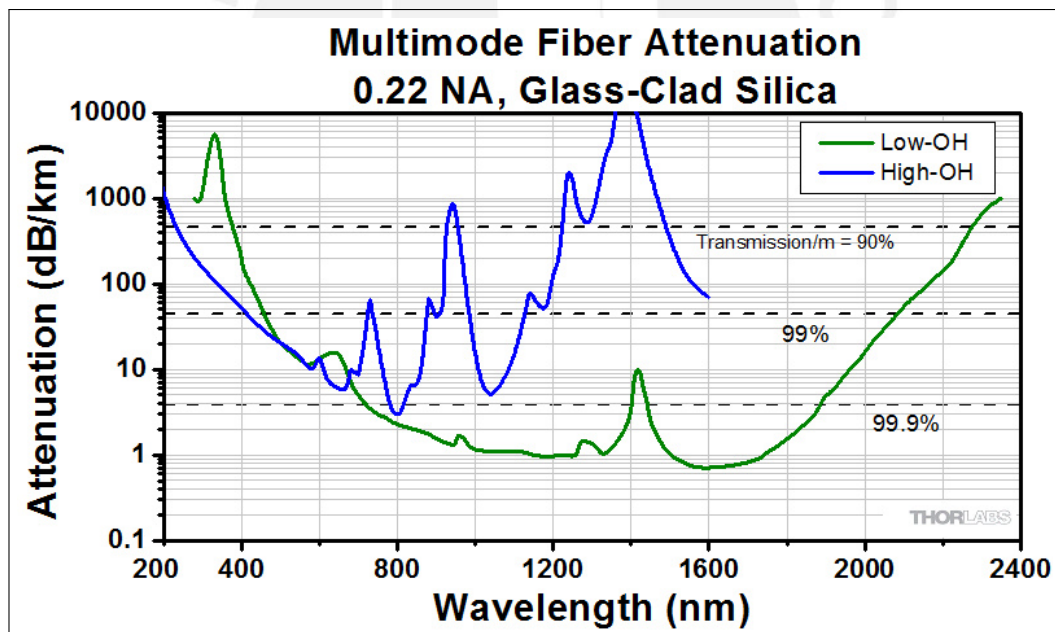


Figure A.1: Fibre attenuation curves from THORLABS. Link: [thorlabs.com/newgrouppage9.cfm?objectgroup\\_id=6838](http://thorlabs.com/newgrouppage9.cfm?objectgroup_id=6838), request date: 10.06.17

#### A.1.2 To Section 6.1.2

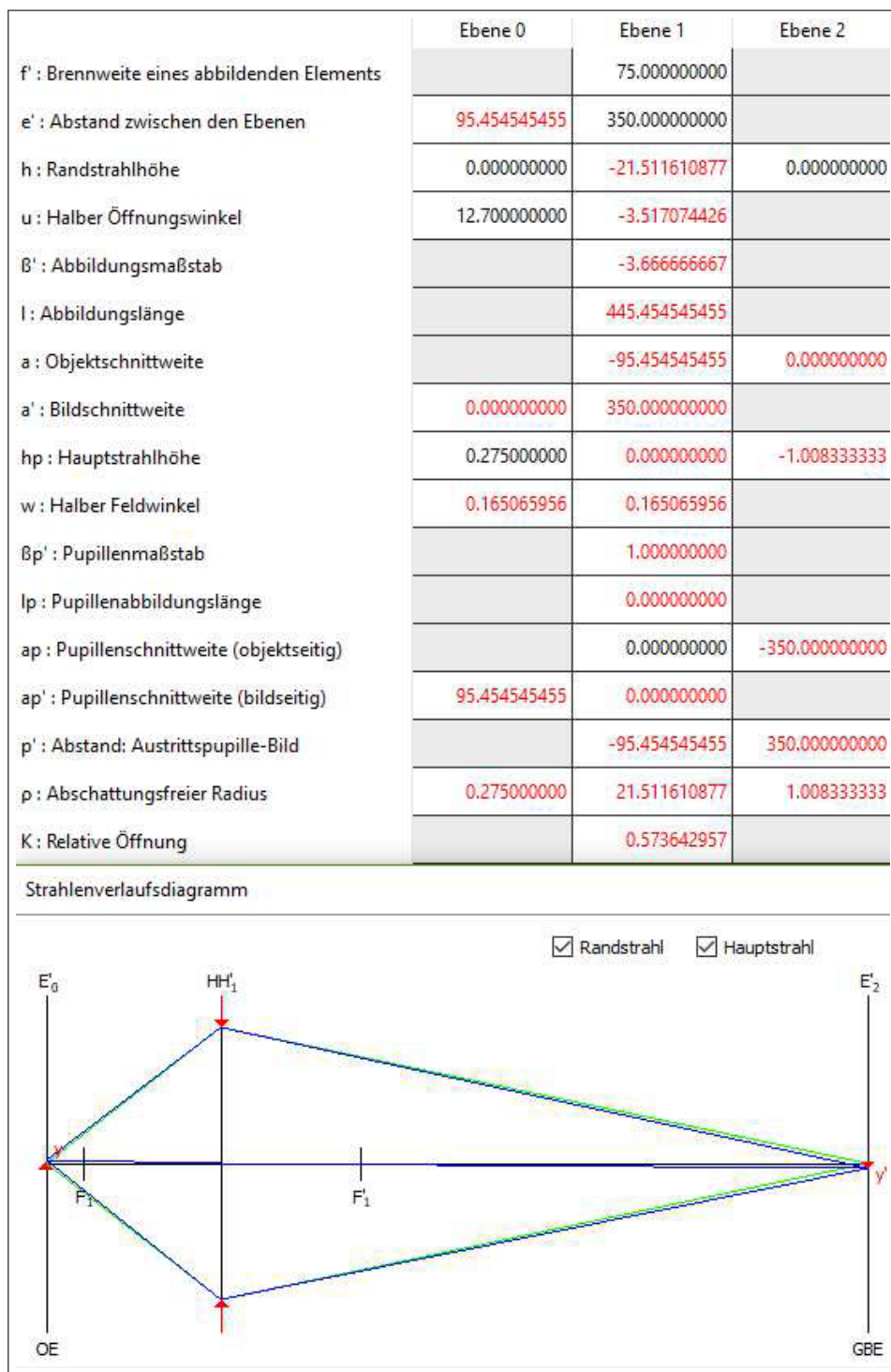


Figure A.2: Screenshot of system design with *Parax* [Mit17]. "Ebene 0" represents the fibre exit plane, "Ebene 1" the lens and "Ebene 2" the object plane (FoV)

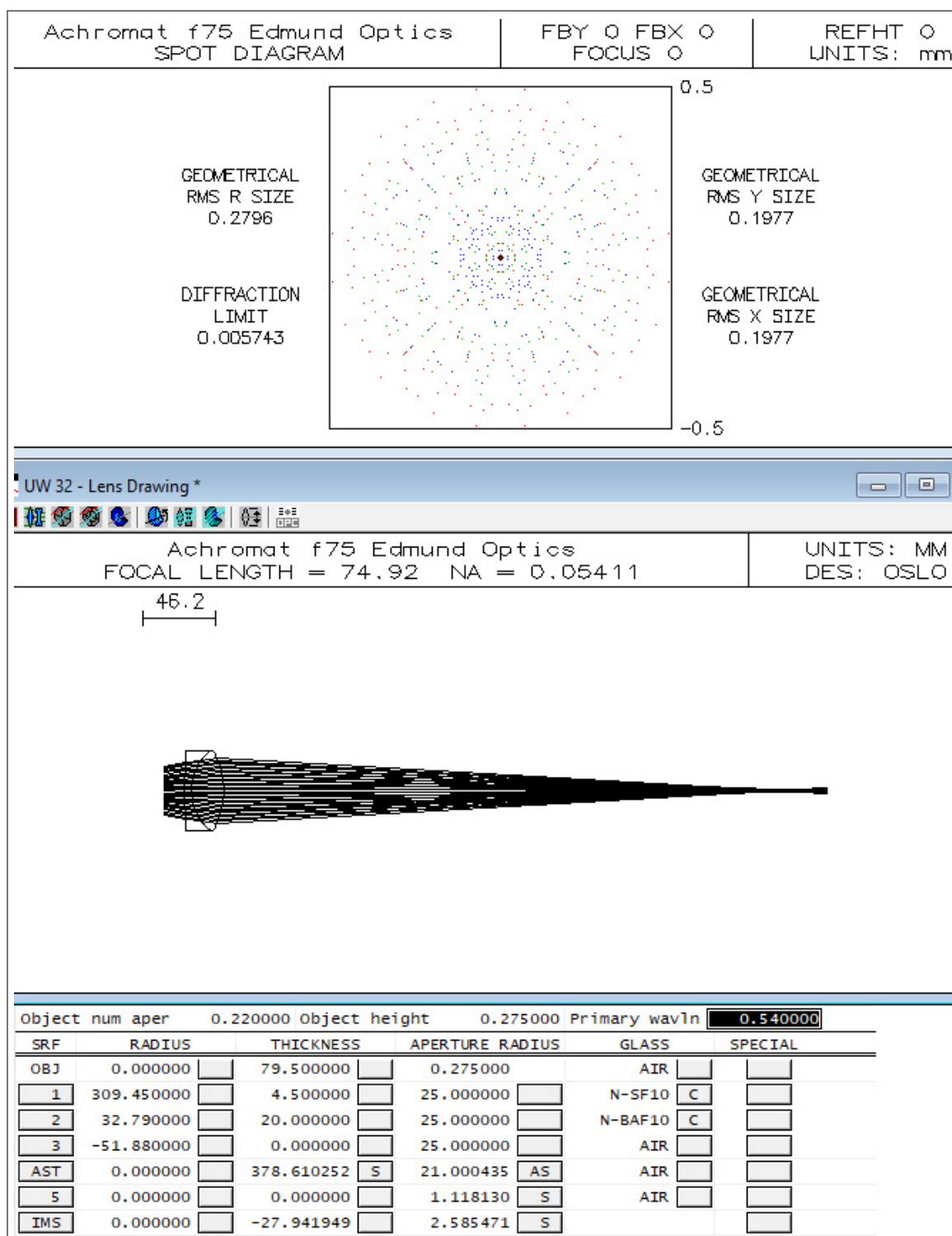


Figure A.3: Screenshot of system analysis with OSLO-EDU [Cor15]. Top: Spot diagram; Middle: Simulated ray fans; Bottom: Lens- and imaging data.

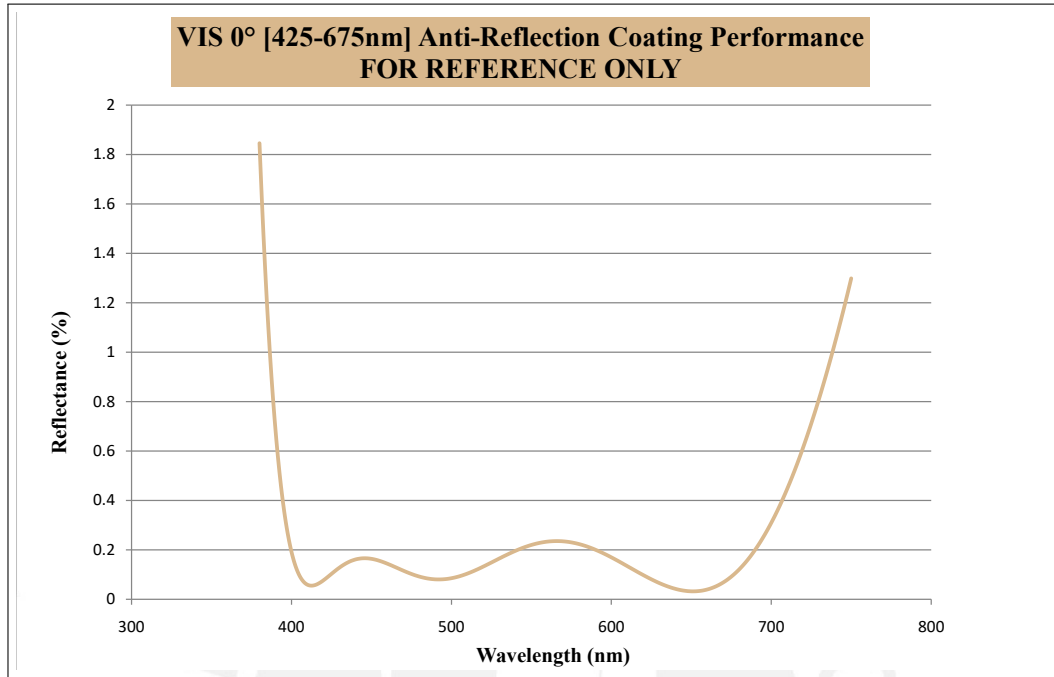


Figure A.4: Lens AR coating curve from EDMUND OPTICS. Link: [edmundoptics.com/optics/optical-lenses/achromatic-lenses/50mm-dia.-x-75mm-fl-vis-0deg-coated-achromatic-lens-/](http://edmundoptics.com/optics/optical-lenses/achromatic-lenses/50mm-dia.-x-75mm-fl-vis-0deg-coated-achromatic-lens-/), request date: 10.06.17

### A.1.3 To Section 6.2.2

Figure A.5 shows that the relationship between the moved paths of objective  $\Delta X$  and FoV  $\Delta x$  is influenced by a relative inclination  $\gamma$  between  $\mathbf{e}_t$  and  $\mathbf{x}_p$ . The relationship can be described by the law of sines:

$$\frac{\Delta x}{\sin(\alpha - \pi/2)} = \frac{\Delta X}{\sin(\beta)}, \quad (\text{A.1})$$

with  $\beta = \pi - (\alpha - \pi/2) - \gamma$ . Equation A.1 can be rewritten as

$$\frac{\Delta x}{\Delta X} = \frac{\sin(\alpha - \pi/2)}{\sin(\frac{3}{2}\pi - \alpha - \gamma)} = \frac{\cos(\alpha)}{\cos(\alpha + \gamma)}. \quad (\text{A.2})$$

As seen in figure A.6, the relationship  $\frac{\Delta x}{\Delta X}$  is sensitive to  $\gamma$ , especially if  $\gamma < 0$  (when  $\mathbf{x}_p$  in figure A.6 shows upwards) and  $\alpha$  is close to  $90^\circ$ . As  $\frac{\Delta x}{\Delta X} \stackrel{!}{=} 1$ ,  $\mathbf{e}_t$  should be parallel to  $x_p$  to achieve that  $\gamma \rightarrow 0$ .

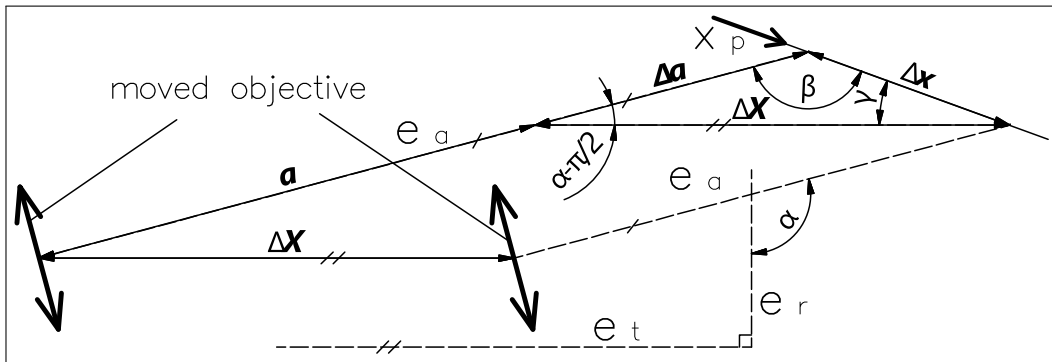


Figure A.5: Consequences of relative inclination  $\gamma$  between  $\mathbf{e}_t$  and  $\mathbf{x}_p$ . Relationship between translation-stage-induced movement of objective  $\Delta X$  and FoV's movement on substrate  $\Delta x$ .

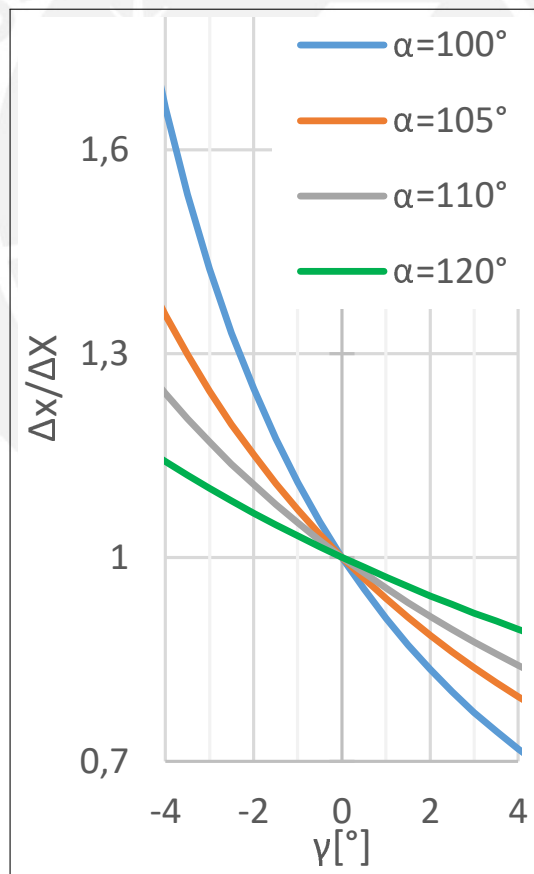


Figure A.6:  $\frac{\Delta x}{\Delta X}(\gamma, \alpha)$

### A.1.4 To Section 7.2

X mm	$\phi_y$ °	n	$H_z = 4.5$ cm				$H_z = 3.0$ cm			
			x mm	y mm	l mm	b mm	x mm	y mm	l mm	b mm
40	0	1	39	2	10	3	39	1	11	3
		2	39	2	10	3	40	1	12	3
		3	39	2	10	3	40	1	12	3
0	0	1	0	3	9	3	1	3	11	3
		2	0	3	9	3	2	3	12	3
		3	0	3	9	3	2	3	12	3
-40	0	1	-38	4	-	-	-37	5	-	-
		2	-39	4	-	-	-36	4	-	-
		3	-38	4	-	-	-37	5	-	-
-40	14	1	-48	86	10	3	-45	88	11	4
		2	-48	86	10	3	-45	88	11	3
		3	-48	86	10	3	-45	88	11	3
0	14	1	-10	85	9	3	-7	86	11	4
		2	-10	85	9	3	-7	86	11	4
		3	-10	85	9	3	-7	86	11	4
40	14	1	28	84	9	4	30	83	11	4
		2	28	84	10	4	30	83	10	4
		3	28	84	9	4	30	83	11	4

X) Coordinate translational stage,  $\phi_y$ ) Coordinate rotational stage, n) repetition, x) and y) Coordinates FoV on scale paper, l) length FoV along x, b) width FoV along y,  $H_z$ ) Substrate height read from ruler on top of chamber

Table A.1: Results of Repeatability and Extend

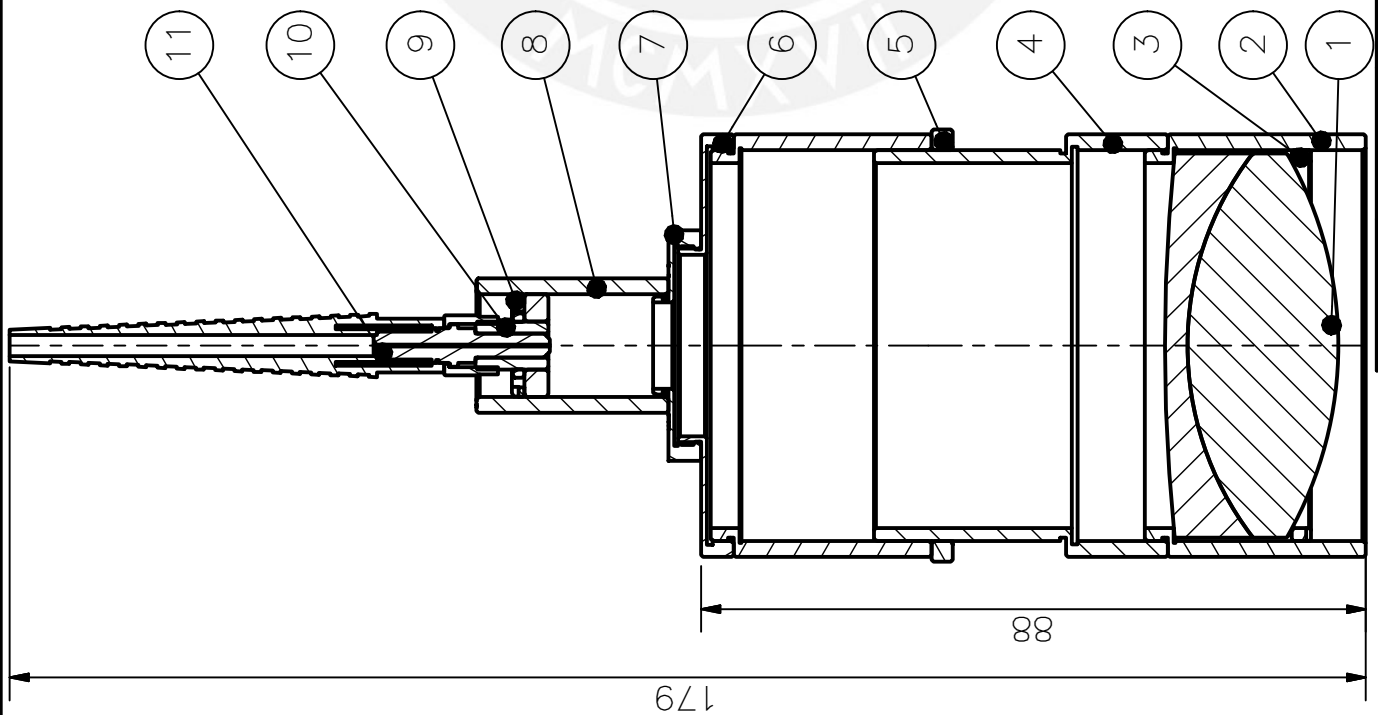


### A.1.5 To Section 7.4

<b>Process parameters</b>	<b>Value prototype</b>	<b>Value final system</b>
Power Magnetron AlN (figure 4.2a, front left)	0	90 <i>W</i>
Power Magnetron Si (figure 4.2a, front right)	100 <i>W</i>	0
Power Magnetron Tb (figure 4.2a, back)	10 <i>W</i>	30 <i>W</i>
Substrate height (ruler value on top of chamber)	3.5 <i>cm</i>	4.0 <i>cm</i>
Nitrogen flow	5 <i>sccm</i>	5 <i>sccm</i>
CCD Integration time	1000 <i>ms</i>	700 <i>ms</i>
Slit width /core diameter	0.50 <i>mm</i>	0.55 <i>mm</i>
Chamber pressure	$(1.6...2.0) \cdot 10^{-2}$ <i>mbar</i>	$1 \cdot 10^{-2}$ <i>mbar</i>

Table A.2: Measurement Conditions: Prototype/Final system

## A.2 Drawings



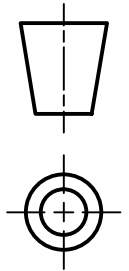
COTA NOMINAL	COTA MÁXIMA	COTA MÍNIMA
--------------	-------------	-------------

PARTS LIST

11	1	SMA Fiber Patch Cable	Glass	Thorlabs, Nr. M37L02
10	1	1/2" SMA Fiber Adapter	Steel	Thorlabs, Nr. SM05SMA
9	1	1/2" Retaining Ring	Aluminium	Thorlabs, Nr. SM05RR
8	1	1/2" Tube	Aluminium	Thorlabs, Nr. SM05M10
7	1	1" to 1/2" Tube Adapter	Aluminium	Thorlabs, Nr. SM1A1
6	1	2" to 1" Tube Adapter	Aluminium	Thorlabs, Nr. SM1A2
5	1	2" Locking Ring	Aluminium	Thorlabs, Nr. SM2NT
4	1	2" Adjustable Length Lens Tube	Aluminium	Thorlabs, Nr. SM2V10
3	1	2" Retaining Ring	Aluminium	Thorlabs, Nr. SM2RR
2	2	2" Lens Tube	Aluminium	Thorlabs, Nr. SM2L10
1	1	Achromat	Glass	Edmund Optics, Nr. #49-292
POS. CANT.		DESCRIPCIÓN	NORMA	MATERIAL

PONTIFICIA UNIVERSIDAD CATÓLICA DEL PERÚ

MÉTODO DE PROYECCIÓN



Física

Objective

ESCALA

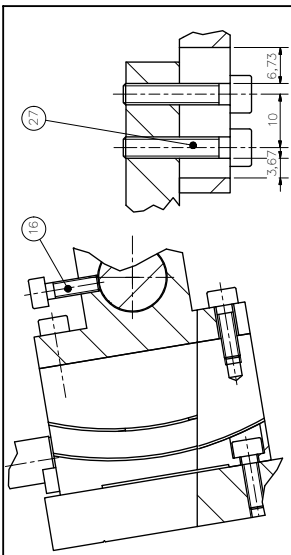
1:1

ASMBL1

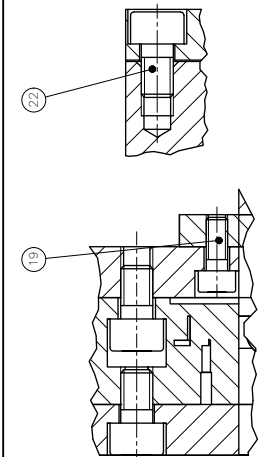
Lich, Julian Andreas

FECHA:  
2017.03.27

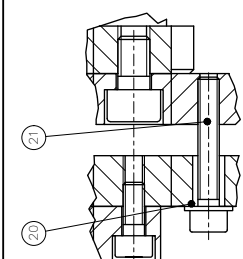
LÁMINA:  
A4



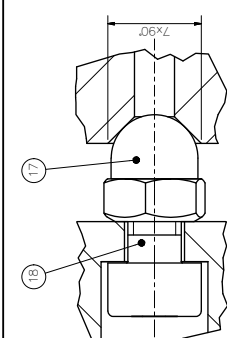
DETALLE J  
ESCALA 2 : 1



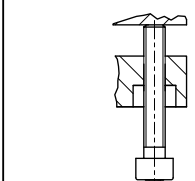
DETALLE H  
ESCALA 2 : 1



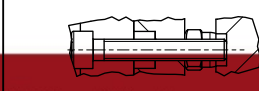
DETALLE F  
ESCALA 2 : 1



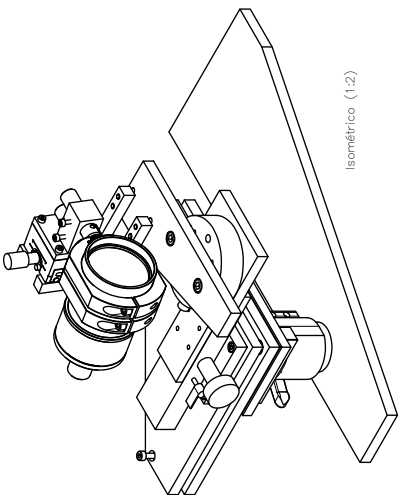
DETALLE E  
ESCALA 3 : 1



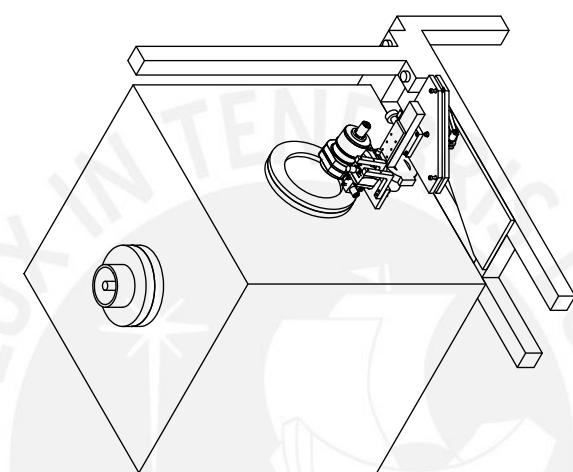
DETALLE D  
ESCALA 2 : 1



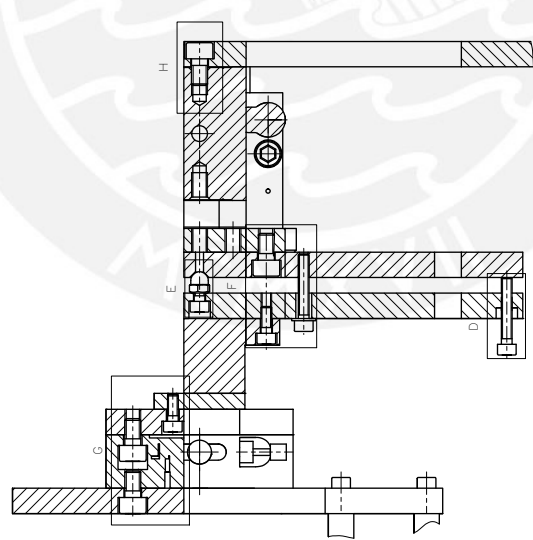
DETALLE C  
ESCALA 2 : 1



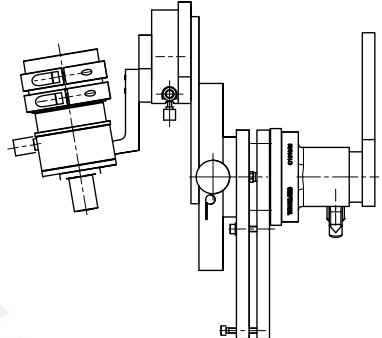
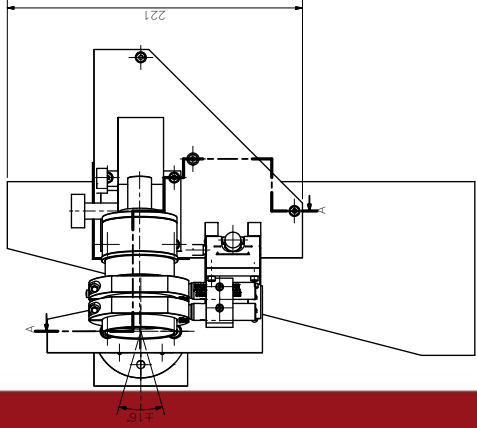
Isométrico (1,2)



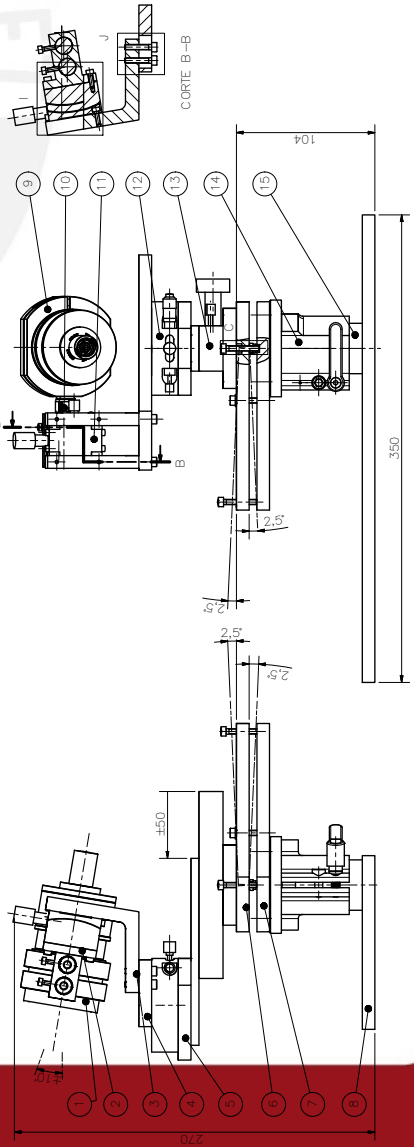
Isométrico (1,5) - Montaje o Cámara de Vacío



CORTE A-A



CORTE B-B



PARIS	US	MATERIAL
27	4 ISO 4762 - M4 x 20	DN EN ISO 4762 Steel
22	9 ISO 4762 - M6 x 10	DN EN ISO 4762 Steel
21	3 ISO 4762 - M4 x 25	DN EN ISO 4762 Steel
20	1 DIN 125 - 4.4.3	DN 125 Steel
19	8 ISO 4762 - M4 x 10	DN EN ISO 4762 Steel
18	1 ISO 4762 - M4 x 6	DN EN ISO 4762 Steel
17	1 DIN 1587 - M4	DN 1587 Steel
16	10 ISO 4762 - M3 x 10	DN EN ISO 4762 Steel
15	1 Hex. Rod	Steel
14	1 Height Adjustable Base	Thomas, Nr. P52/M
13	1 Rack & Pinion Stage	Edmond Optics Nr. #66-517
12	1 Rotation Stage	Edmond Optics Nr. #66-517
11	1 Goniometer	Edmond Optics Nr. #66-517
10	2 Comp. Rod	Thomas, Nr. TR30C/M
9	2 Objective Comp.	Aluminum Nr. SM2C/M
8	1 Rack Base	Aluminum Constructed
7	1 Lower Tri. Platform	Aluminum Constructed
6	1 Upper Tri. Platform	Aluminum Constructed
5	1 V2 - Connector + Stop	Aluminum Constructed
4	1 V2 - Connector 2	Aluminum Constructed
3	1 V2 - Connector 1	Aluminum Constructed
2	1 Pos. Holder	Aluminum Constructed
1	1 Objective	See ASSEMBLY OBSERVACIONES

METODO DE PROTECCION  
TUBO

PONTIFICIA UNIVERSIDAD CATOLICA DEL PERU

ESCALA 1:2

Mechanics Assembly

Lich, Julian Andreas

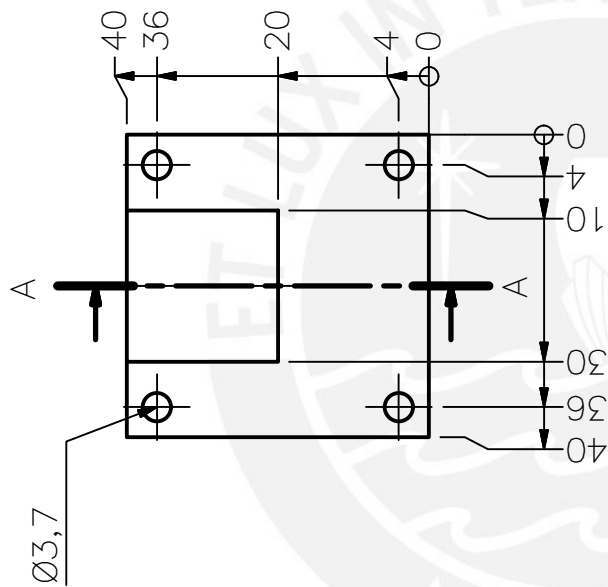
FECHA: 2017.04.24  
LÁMINA: A1

ASMBL2

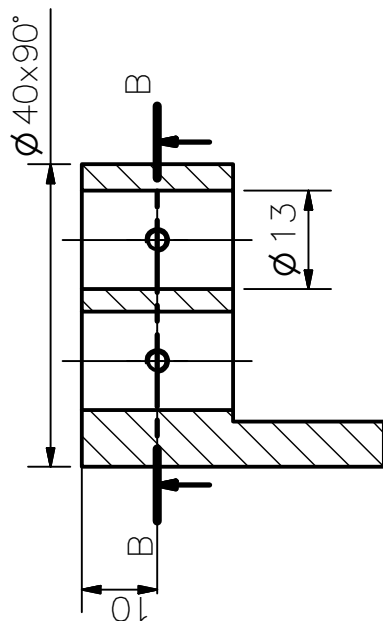
COTA: NOMENCLATURA

COTA: MATERIAL

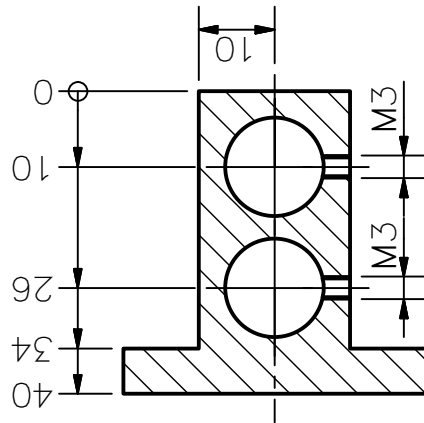
COTA: MEDIDA



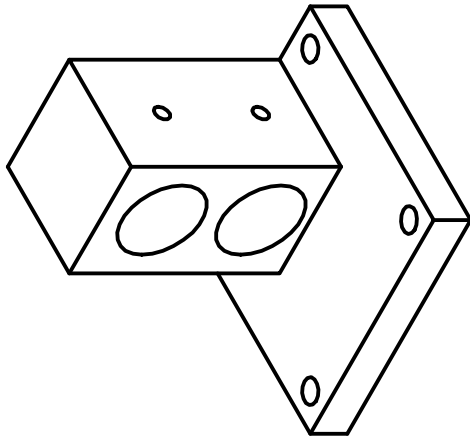
$\varnothing 3,7$



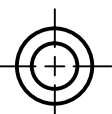
CORTE A-A



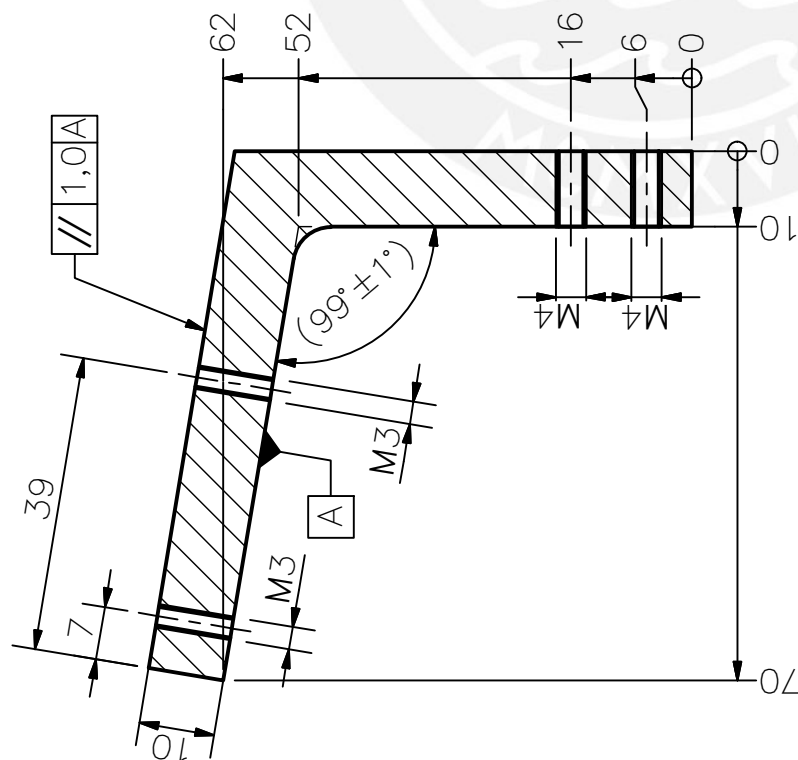
CORTE B-B



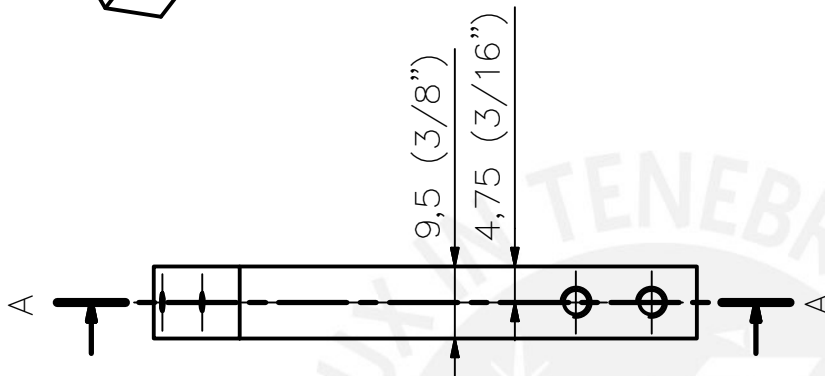
Isométrico (1:2)

ACABADO SUPERFICIAL	TOLERANCIA GENERAL DIN ISO 2768 mK	MATERIAL Aluminio
PONTIFICIA UNIVERSIDAD CATÓLICA DEL PERÚ Física		
MÉTODO DE PROYECCIÓN 	Conector Barras—Goniometro	
PC 1	Lich, Julian Andreas	ESCALA 1:1
		FECHA: 2017.04.24
		LÁMINA: A4

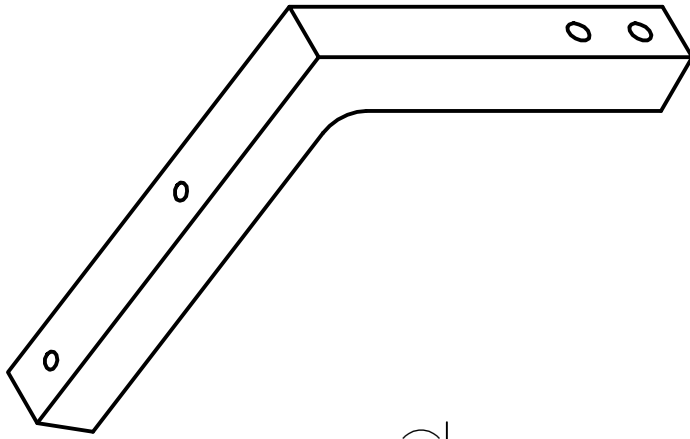
COTA NOMINAL	COTA MÁXIMA	COTA MÍNIMA
--------------	-------------	-------------

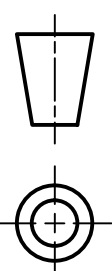


CORTE A-A

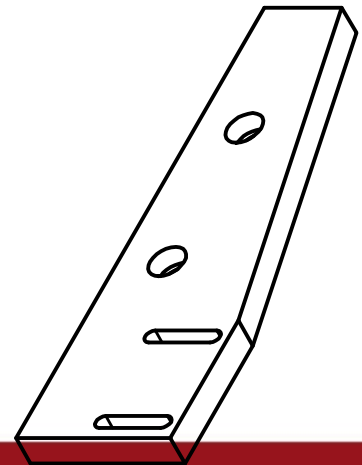
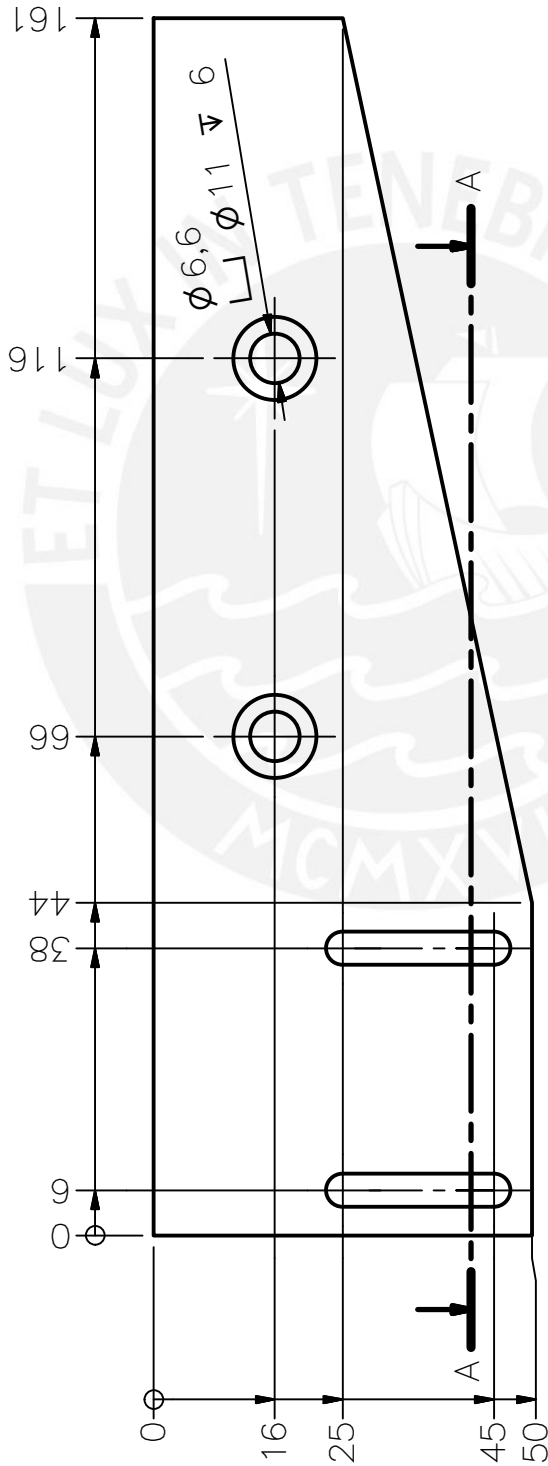
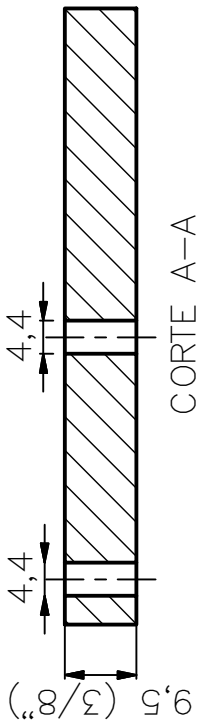


Isométrico (1:1)



ACABADO SUPERFICIAL	TOLERANCIA GENERAL DIN ISO 2768 mK	MATERIAL Aluminio
PONTIFICIA UNIVERSIDAD CATÓLICA DEL PERÚ Física		
MÉTODO DE PROYECCIÓN 	Base inclinada para Goniometro	ESCALA 1:1
PC 2	Lich, Julian Andreas	FECHA: 2017.04.24
		LÁMINA: A4

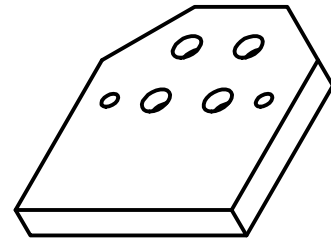
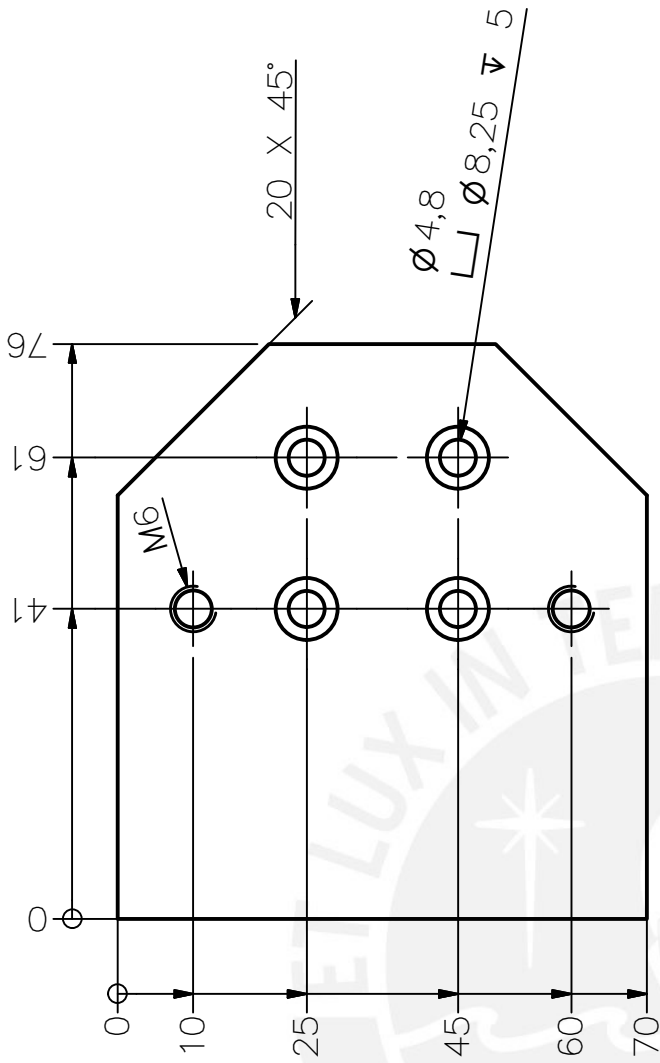
COTA NOMINAL	COTA MÁXIMA	COTA MÍNIMA




ACABADO SUPERFICIAL	TOLERANCIA GENERAL DIN ISO 2768 mK	MATERIAL Aluminio
PONTIFICIA UNIVERSIDAD CATÓLICA DEL PERÚ Física		
MÉTODO DE PROYECCIÓN	Conector del Goniometro	ESCALA 1:1
PC 3	Lich, Julian Andreas	FECHA: 2017.04.24
		LÁMINA: A4

COTA NOMINAL	COTA MÁXIMA	COTA MÍNIMA
--------------	-------------	-------------

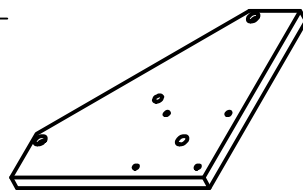
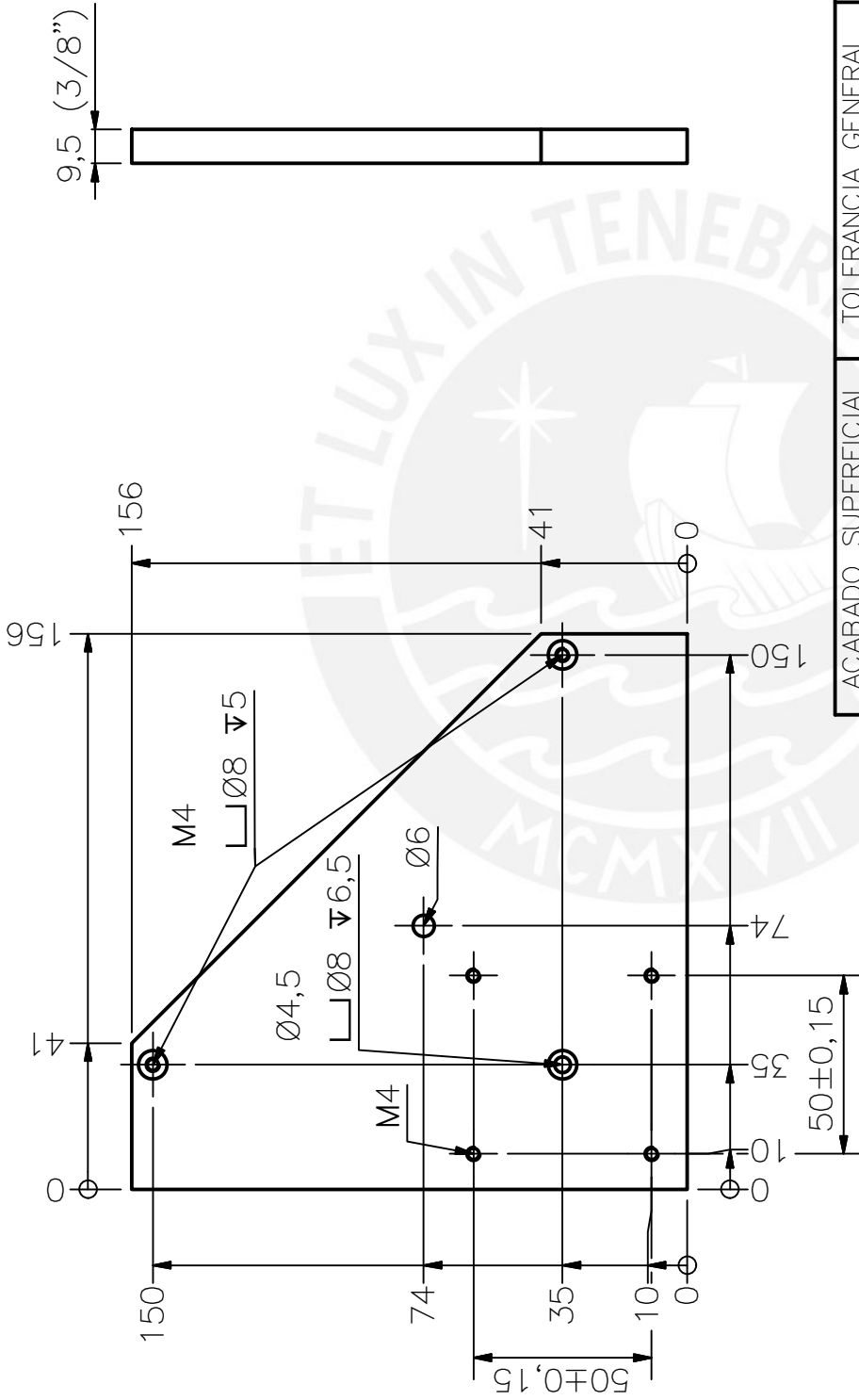
9,5 (3/8")



Isométrico (1:2)

ACABADO SUPERFICIAL	TOLERANCIA GENERAL DIN ISO 2768 mK	MATERIAL Aluminio
PONTIFICIA UNIVERSIDAD CATÓLICA DEL PERÚ Física		
MÉTODO DE PROYECCIÓN 	Conector Y-X	
PC4	Lich, Julian Andreas	ESCALA 1:1
		FECHA: 2017.04.24
		LÁMINA: A4

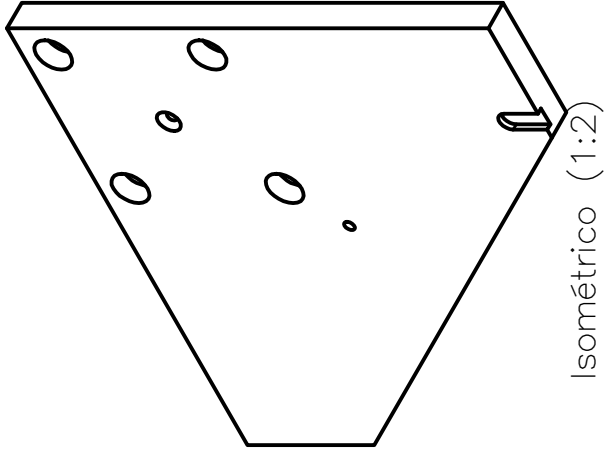
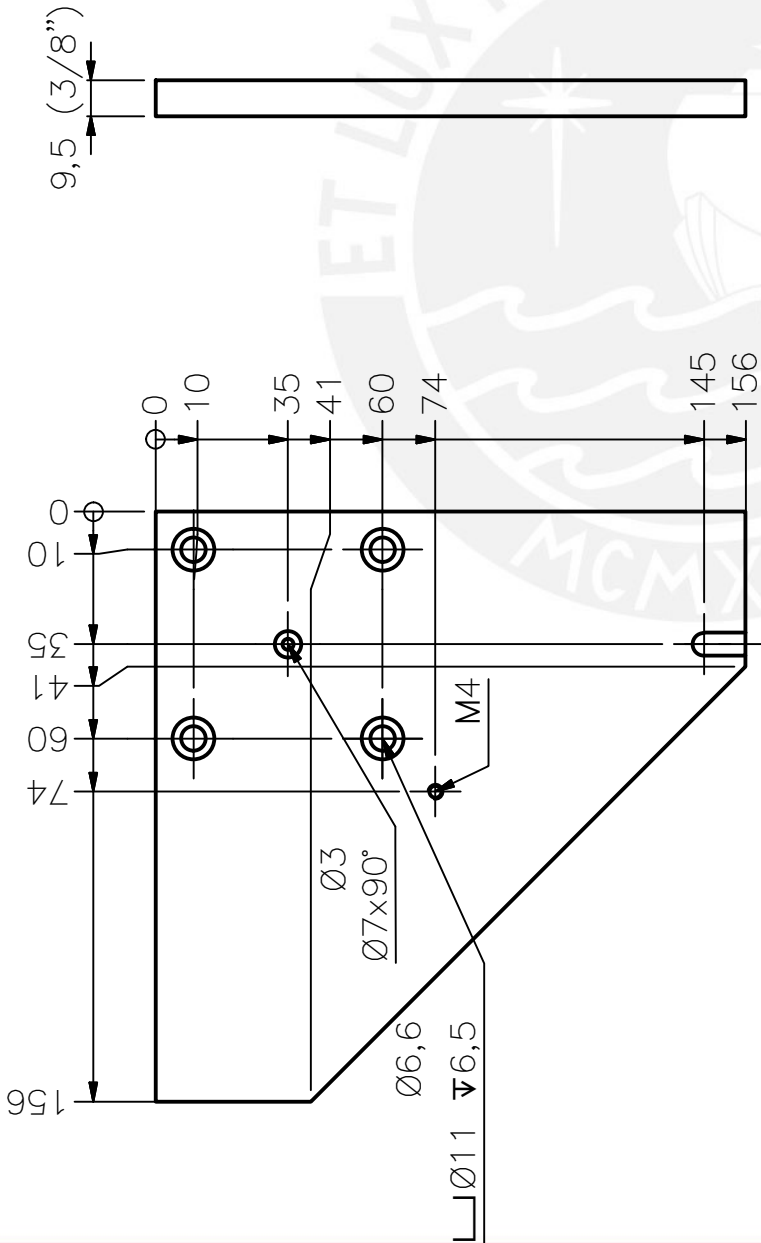
COTA NOMINAL	COTA MÁXIMA	COTA MÍNIMA
--------------	-------------	-------------

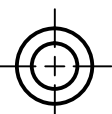


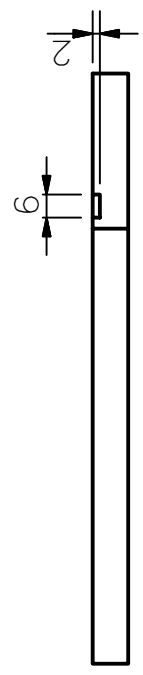
ACABADO SUPERFICIAL	TOLERANCIA GENERAL DIN ISO 2768 mK	MATERIAL Aluminio
PONTIFICIA UNIVERSIDAD CATÓLICA DEL PERÚ Física		
MÉTODO DE PROYECCIÓN	Base para inclinación encima	ESCALA 1:2
PC5	Lich, Julian Andreas	FECHA: 2017.04.24
		LÁMINA: A4

COTA NOMINAL	COTA MÁXIMA	COTA MÍNIMA
--------------	-------------	-------------



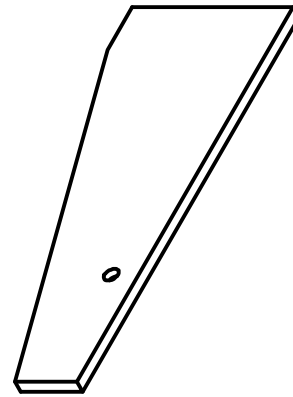
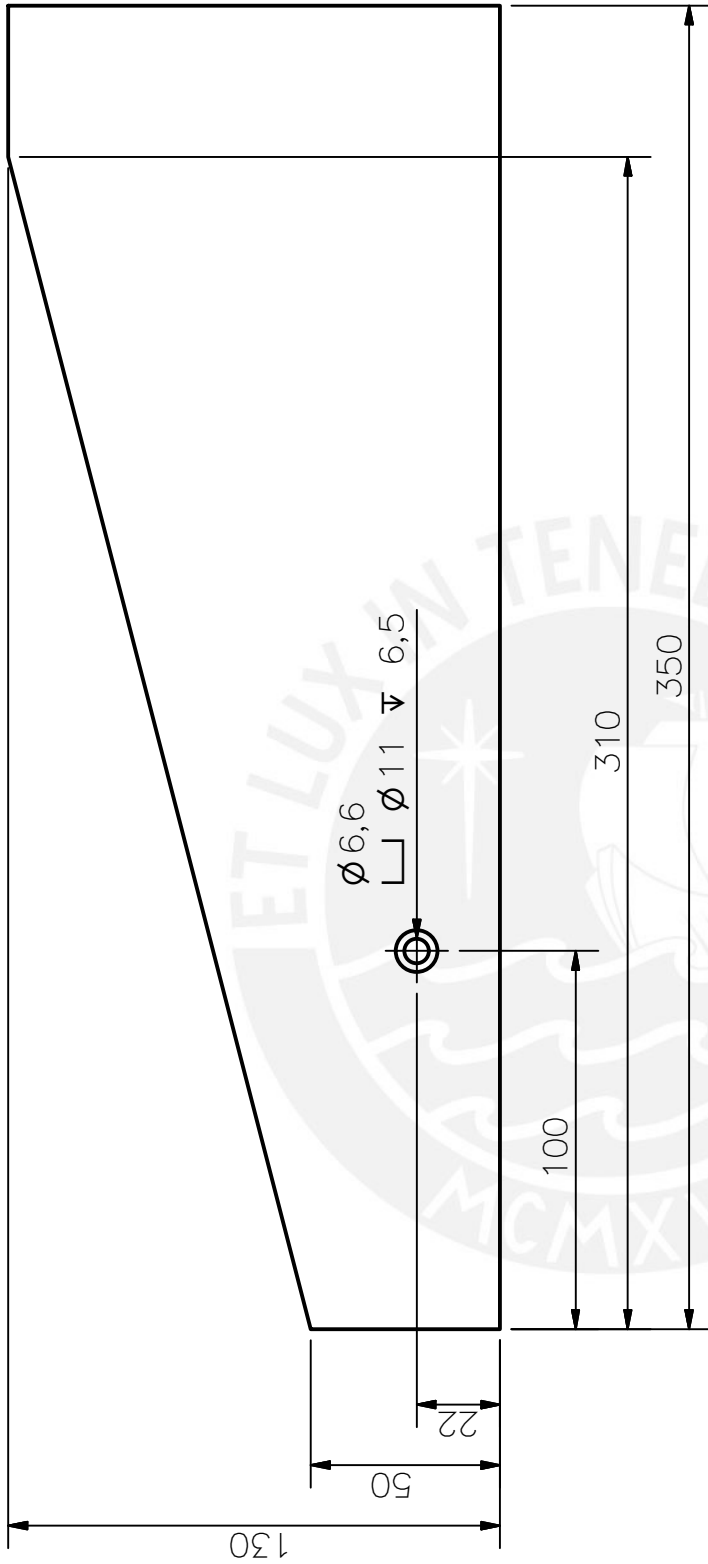


ACABADO SUPERFICIAL	TOLERANCIA GENERAL DIN ISO 2768 mK	MATERIAL Aluminio
PONTIFICIA UNIVERSIDAD CATÓLICA DEL PERÚ Física		
MÉTODO DE PROYECCIÓN 	Base para inclinación abajo	ESCALA 1:2
PC6	Lich, Julian Andreas	FECHA: 2017.04.24
		LÁMINA: A4

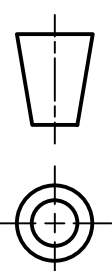


COTA NOMINAL	COTA MÁXIMA	COTA MÍNIMA
--------------	-------------	-------------

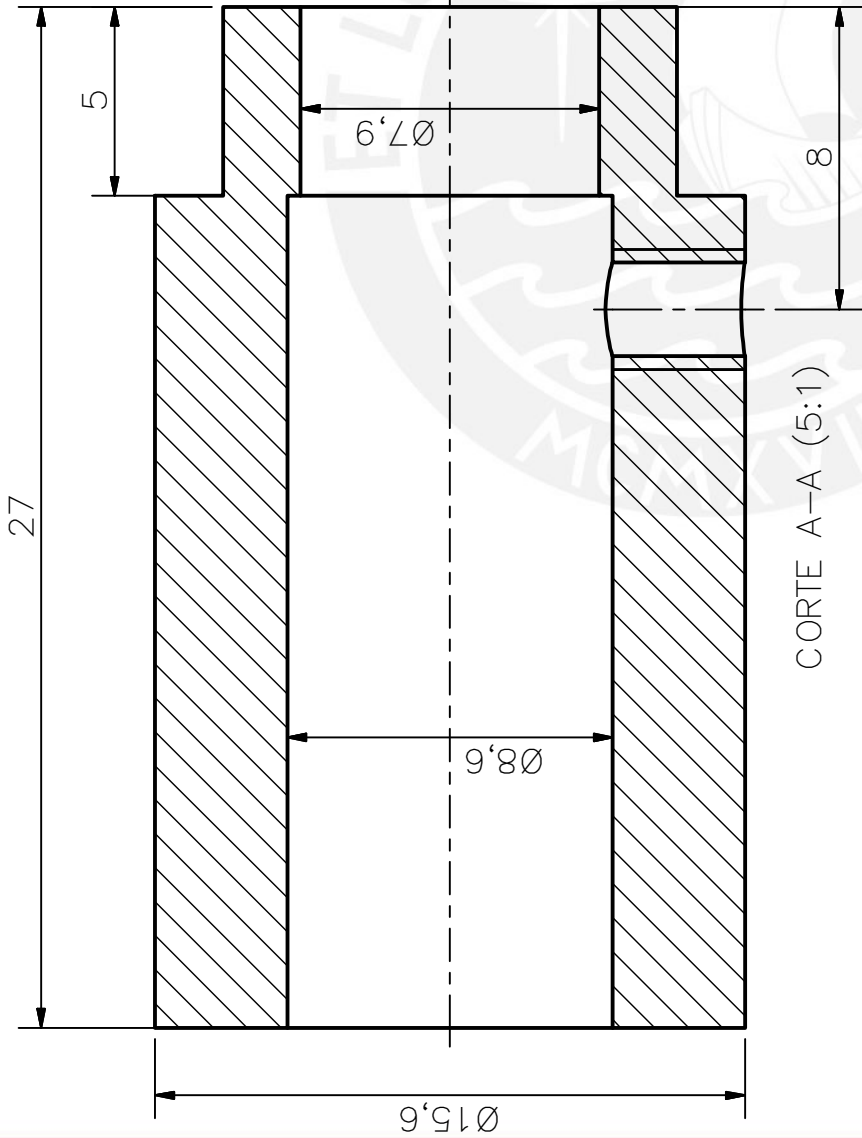
9,5 (3/8")



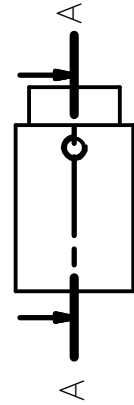
Isométrico (1:5)

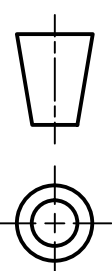
ACABADO SUPERFICIAL	TOLERANCIA GENERAL DIN ISO 2768 vL	MATERIAL Aluminio
PONTIFICIA UNIVERSIDAD CATÓLICA DEL PERÚ Física		
MÉTODO DE PROYECCIÓN	Plancha de soporte	ESCALA 1:2
		FECHA: 2017.04.24
PC 7	Lich, Julian Andreas	LÁMINA: A4

COTA NOMINAL	COTA MÁXIMA	COTA MÍNIMA
--------------	-------------	-------------



CORTE A-A (5:1)



ACABADO SUPERFICIAL	TOLERANCIA GENERAL DIN ISO 2768 mK	MATERIAL Aluminio
PONTIFICIA UNIVERSIDAD CATÓLICA DEL PERÚ Física		
MÉTODO DE PROYECCIÓN 	Adaptador Fibra-Espectrógrafo	ESCALA 1:1 (5:1)
PCA1	Lich, Julian Andreas	FECHA: 2017.05.02
		LÁMINA: A4

COTA NOMINAL	COTA MÁXIMA	COTA MÍNIMA
--------------	-------------	-------------

# Bibliography

- [AA14] Alexander Axelevitch and Boris Apter. Optical emission spectroscopy of the sputtering process in the triode system. *Radiation Effects and Defects in Solids*, 169(9):759–766, 2014.
- [Beh81] R Behrisch. *Sputtering by particle bombardment I. Physical sputtering of single-element solids, Vol. 47*. Springer-Verlag, New York, NY, 1981.
- [BRRA05] BC Barja, A Remorino, MJ Roberti, and PF Aramendia. Luminescence quenching of europium (iii) and terbium (iii) carboxylates by transition metals in solution. In *Anales de la Asociación Química Argentina*, volume 93, pages 81–96. SciELO Argentina, 2005.
- [Cha08] Julio Chaves. *Introduction to Nonimaging Optics*. Boca Raton, FL: CRC Press, London: Taylor and Francis, 2008.
- [Cor15] Lambda Research Corporation. *OSLO-EDU, Revision 6.6.5*. 25 Porter Road Littleton, MA 01460, Copyright ©2001-2015. [lambdaresearch.com/oslo/](http://lambdaresearch.com/oslo/).
- [Dem14] Wolfgang Demtröder. *Laser Spectroscopy 1*. Springer, Kaiserslautern, Germany, 5 edition, 2014.
- [Fre96] Roger Freeman. *Reference Manual for Telecommunications Engineering*. John Wiley & Sons, Inc., New York, NY, 1996.
- [GDZT<sup>+</sup>16] JA Guerra, F De Zela, K Tucto, L Montañez, JA Töfflinger, A Winnacker, and R Weingärtner. Effect of thermal annealing treatments on the optical activation of tb3+-doped amorphous sic: H thin films. *Journal of Physics D: Applied Physics*, 49(37):375104, 2016.

- [GMW<sup>+</sup>15] J Andres Guerra, Liz Montañez, Albrecht Winnacker, Francisco De Zela, and Roland Weingärtner. Thermal activation and temperature dependent pl and cl of tb doped amorphous aln and sin thin films. *physica status solidi (c)*, 12(8):1183–1186, 2015.
- [Goe67] David G. Goebel. Generalized integrating-sphere theory. *Appl. Opt.*, 6(1):125–128, Jan 1967.
- [Haf03] Heinz Haferkorn. *Optik. Physikalisch-technische Grundlagen*. Weinheim: Wiley-VCH., 2003.
- [Kas11] Keith J Kasunic. *Optical Systems Engineering*. New York : McGraw-Hill Professional, 2011.
- [Kos12] R John Koshel. *Illumination Engineering: design with nonimaging optics*. John Wiley & Sons, 2012.
- [Law13] Andy Lawrence. *Astronomical Measurement: A Concise Guide*. Springer Science & Business Media, 2013.
- [LJ07] HJ Lozykowski and WM Jadwisieniczak. Thermal quenching of luminescence and isovalent trap model for rare-earth-ion-doped aln. *physica status solidi (b)*, 244(6):2109–2126, 2007.
- [MIE<sup>+</sup>01] Fumiaki Mitsugi, Tomoaki Ikegami, K Ebihara, J Narayan, and AM Grishin. Colossal magnetoresistive and ferroelectric thin films deposited by excimer laser induced plasma. *Science and Technology of Advanced Materials*, 2(3):525–531, 2001.
- [Mit17] Beate Mitschunas. *Nutzerdokumentation zum Programm PARAX 2.0*, 2017.
- [MP14] Sergio Musazzi and Umberto Perini. *Laser-induced breakdown spectroscopy*, volume 182. Springer, 2014.
- [Naw11] Amruta V Nawarange. *Optical emission spectroscopy during sputter deposition of CdTe solar cells and CuTe-based back contacts*. PhD thesis, The University of Toledo, 2011.
- [New] Newport Corporation, 1791 Deere Avenue, Irvine, CA, 92606, USA. *Light Collection and Systems Throughput*. <https://www.newport.com/t/light-collection-and-systems-throughput>, date of retrieving: 01.2017.

- [New15] Newport Corporation, 1791 Deere Avenue, Irvine, CA, 92606, USA. *Oriel MS260i, 1/4m Imaging Spectrograph Family - User's Manual*, 2015.
- [New16] Newport Corporation, 1791 Deere Avenue, Irvine, CA, 92606, USA. *Oriel Cornerstone 260, 1/4m Monochromator - Data Sheet*, 09 2016.
- [Noj15] Kazuo Nojiri. *Dry etching technology for semiconductors*. Springer, 2015.
- [Ohr01] Milton Ohring. *Materials science of thin films*. Academic press, 2001.
- [OLZ+13] MF Omar, HH Ley, J Zainal, AK Ismail, RK Raja Ibrahim, and S Sakrani. Optical emission spectroscopy study on deposition process of silicon carbide thin films. In *Photonics (ICP), 2013 IEEE 4th International Conference on*, pages 154–156. IEEE, 2013.
- [PL05] Christopher A Palmer and Erwin G Loewen. *Diffraction grating handbook*. Newport Corporation Springfield, Ohio, USA, 2005.
- [RWS99] A Raveh, M Weiss, and R Schneck. Optical emission spectroscopy as a tool for designing and controlling the deposition of graded tialn layers by ecr-assisted reactive rf sputtering. *Surface and Coatings Technology*, 111(2):263–268, 1999.
- [Tho] Inc. Thorlabs. Modifying beam profiles with multimode fibers. Technical report, Thorlabs, Inc., 56 Sparta Avenue, Newton, New Jersey 07860, USA. [https://www.thorlabs.com/images/TabImages/MM\\_Fiber\\_Lab.pdf](https://www.thorlabs.com/images/TabImages/MM_Fiber_Lab.pdf), date of retrieving: 05.2017.
- [TS16] Karem Tucto Salinas. Structural, luminescence and judd-ofelt analysis to study the influence of post-annealing treatment on the ain: Tb thin films prepared by radiofrequency magnetron sputtering. Master's thesis, PUCP, Peru and TU Ilmenau, Germany, 2016.
- [URK00] Urs Utzinger and R Richards-Kortum. Fiber optic probes for optical spectroscopy, clinical applications. *Encyclopedia of Spectroscopy and Spectrometry*, pages 513–527, 2000.

- [WKA04] Kiyotaka Wasa, Makoto Kitabatake, and Hideaki Adachi. *Thin film materials technology: sputtering of control compound materials*. Springer Science & Business Media, 2004.

